AL-MUSTANSIRIYAH JOURNAL OF SCIENCE

Volume 2, December 1977

College of SCIENCE, AL-MUSTANSIRIYAH
UNIVERSITY BAGHDAD-IRAQ

CONTENT

COLLEGE OF SCIENCE PRESS
UNIVERSITY OF BAGHDAD

AL-MUSTANSIRIYAH JOURNAL OF SCIENCE

Volume 2, December 1977

College of science, Al-Mustansiriyah University Baghdad-Iraq

Instructions for Authors:

1. Manuscripts should be Submitted in triplicate, they should be typewritten with double spacings. A margin of about 2.5 cm should be left onthe left hand side.
2. Both Arabic and English abstracts should be submitted, typed on separate sheets of paper.
3. The title of the Paper together with the name and address of the author (s) should be typed on a separate sheet. Name of author shouldbe written in full e.g Ahmed M. Ali.
4. Figures and illustrations should be drawn in black china ink on tracing Papers. Three photocopies of each diagram should also be submitted. Captions to figures should be written on the trace paper.
5. Tables should be arranged in such away so as to make them legible .
6. The same facts should not be given in tables and figures except when it is absoutely necessary to do so.
7. Reference numbers should be written between square brackets []. A list of referances should be given on a separate sheet of paper.
8. Where possible, Papers should follow the Pattern: Introduction, Experimental, Results and Discussion.

Al-mustansiriy Ah Journal Of Science
Volume 2, December 1997

AI-MUSTANSIRIYAH JOURNAL OF SCIENCE 1977

CONTENT

FABRICATION AND PERFORMANCE OF THIN SILICON SURFACE-BARRIER DETECTORS

T.M. Al-Ardawi, A.A. Abdulla & M.A. Al-Jeboori*

Department of Physics, College of Science,
Baghdad University.

ABSTRACT

Thin silicon surface-barrier detectors have been prepared for particle detection. A special technique was used for preparation of very thin silicon slices and for their oxidation. Study of the characteristics of these detectors has shown that gold-silicon contact has a weak but stable barrier.

INTRODUCTION

Semiconductor detectors are widely used in detection of nuclear radiation, as they have the great advantage of good performance. Nevertheless when using semiconductors in detection of heavey ions and fission fragments, two main problems arise. The first one concerns the energy defect associated with the atomic or nuclear scattering. The second problem is that of inefficient charge collection from semiconductor under conditions likely to give either high recombination rate or high trapping rate. The latter problem is usually solved by using either thin slices of low resistivity or thick slices of high resistivity crystals. Thick slices have distinct disadvantage because of their increased sensitivity to gamma radiation, neutrons and light charged particles.

---

* Now at the College of Science, Al-Mustansiriyah University, Baghdad, Iraq.

Al-Mustansiriyah Journal of Science, Vol. 2 (1977).

The use of dE/dx detectors in conjunction with total energy (E) detector results in a very effective system for separation and identification of a group of different types of particles. Silicon surface barrier total energy detectors have been prepared by different workers. They followed different procedures in a trial to attain improved detector characteristics. Generally, the detectors fabricated by these workers were of different performances depending on the procedures used in their preparation.

The present work was aimed to prepare thin silicon surface-barrier detectors with improved characteristics for alpha-particle detection.

EXPERIMENTAL

Preparation technique

Preparation of a thin semiconductor detector involves several technological problems. The most important two conditions to be fulfilled are: 1) High degree of surface uniformity to minimize the energy loss fluctuation due to the thickness variation which has a great effect on the spectrum broadening, 2) High ohmicity of the back contact to avoid increasing the device noise when the space-charge region reaches the back. Several methods have been reported to prepare thin silicon slices of high thickness uniformity. These methods include chemical etching[1,2,3] and/or mechanical lapping[4,5,6] in addition to more sophisticated techniques[7].

Recently Porpon et al.[8] followed a new procedure for preparation of semiconductor ΔE detector. The method could be described briefly as the growing of epitaxial semiconductor layer of high resistivity on a low resistivity n-type silicon crystal.

Generally silicon crystals are polished to a thickness of about 100 micron. The thining operation is then continued through chemical etching until the crystal thickness is reduced to the required magnitude. But here we are faced with the problem of surface nonuniformity, which is due to the nonuniform movement of the etchant on the surface of the crystal.

To minimize the surface nonuniformity a special apparatus was developed for mechanical polishing and another for chemical etching of the crystals. The two apparatus are shown in figures 1 and 2.

When these apparatus were used crystals of high-uniform thickness were obtained. The uniformity was tested by scaning the surface of the crystal using a beam of collimated α-particles. The variation in the thickness was seen to be less than 0.4 μm over 20 mm^2 area.

Oxidation of the surface of n-type Si crystals was performed by treatment with hot diluted solution of sodium dichromate. For p-type silicon crystals concentrated nitric acid was used as oxidizing agent instead of sodium dichromate, as the latter tends to lower the p-type barrier (see ref. 9). A number of p-type detectors were prepared using air as oxidizing agent. These detectors were highly noisy and deteriorated within 3 days.

A gold film of 40-50 $\mu g/cm^2$ was used as a front contact while an aluminium film of 20-30 $\mu g/cm^2$ was used as a back contact.

Detector performance

The characteristics of the prepared silicon surface barrier detectors were determined using the measuring system shown in figure 3. The system linearity was tested using α-particle source. The multichannel analyzer (MCA) was calibrated using Am^{241} α-particle source

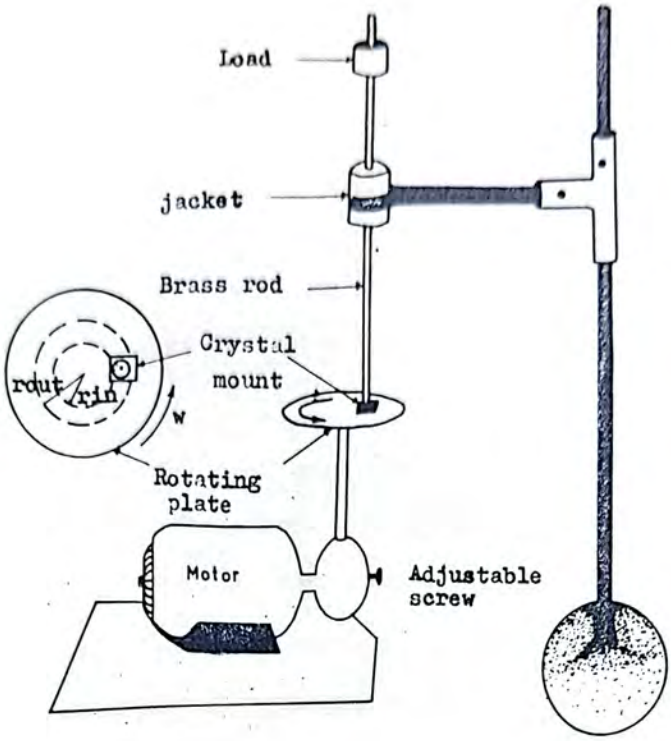

Fig. 1. Shows the system of the mechanical polishing.

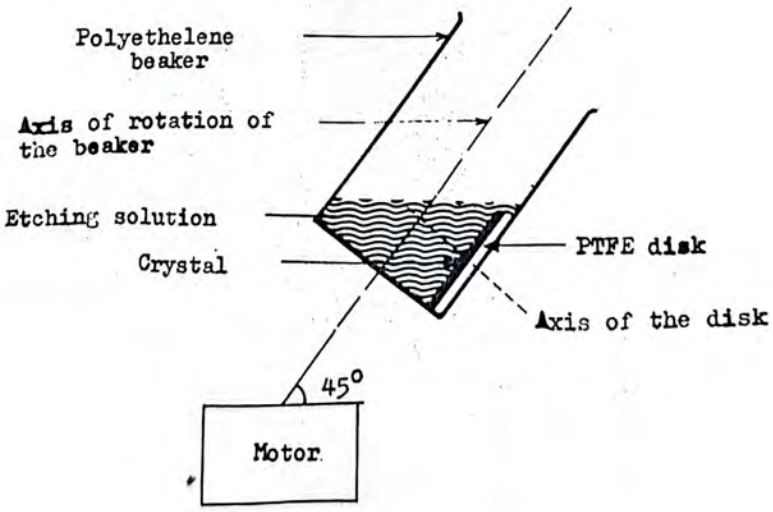

Fig. 2. The etching system.

of energy 5.486 Mev, a pulse generator and ortic 419 mercury relay pulser. A completely stopping detector was used for the detection of Am^{241} spectrum. A simple circuit was used for measuring the volt-ampere characteristics of the detector. The detectors capacitance as a function of reverse bias voltage was measured using a small capacitor bridge type TM-351-G-No.1737 and RC generator. The measurements were carried out at a frequency of 1.5 KHz and input voltage 0.1 volts. An AC millivoltmeter was used as a signal detector. The leakage current as a function of bias voltage was measured using a DC microammeter connected to the current monitoring jaks on the bias supply unit across a resistance of 1 MΩ. The system noise was measured by feeding pulses through the system from the ortic 419 mercury relay pulser. The total amplifier-detector noise resolution spread is equal to the FWHM of the pulser spectrum.

The energy resolution of the detector was measured using 512 multi-channel analyzer (MCA). A thin α-particle source (Am^{241})of activity (0.15 μC) and energy 5.486 Mev and Ra^{226} source. A copper collimator of diameter 4 mm was used between the source and the detector.

RESULTS AND DISCUSSIONS

Figure 4 shows the variation of the detectors capacitance with the applied voltage in reverse direction. It can be noticed that the detectors capacitance steeply decreases at first then attains a constant value. Here the capacitance is related to the detectors material and applied voltage according to the equation[10]

$$C = \frac{xA}{4\pi d}$$

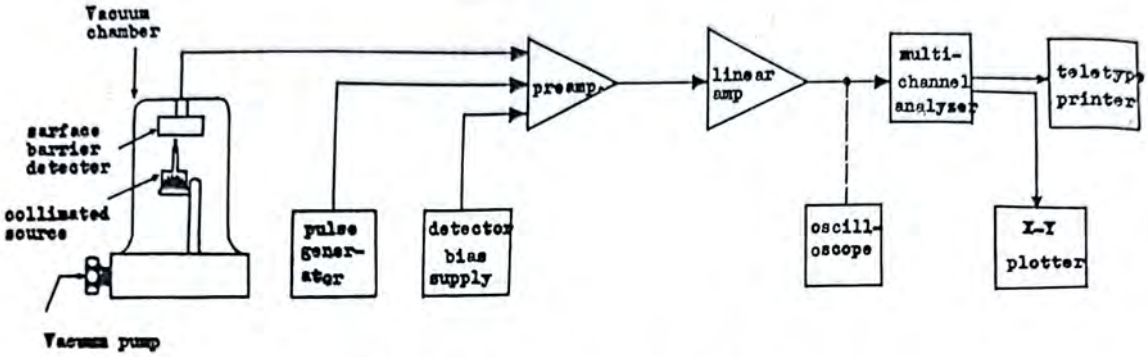

Fig. 3. Schematic diagram for the system used.

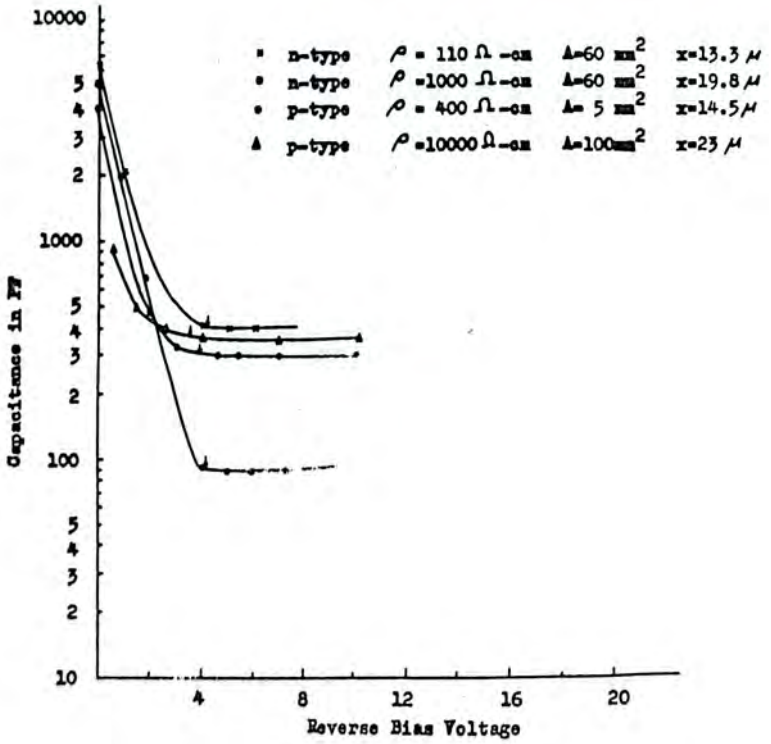

Fig. 4. C-V characteristics for different thickness ΔE detectors.

where x is the dielectric constant of the material, A is the detectors area, d is the depletion thickness.

Figures 5 and 6 show the I-V characteristics of both p- and n-type detectors. These results agree with the suggestion of Anderson[11].

It is interesting to note that the p-type detector prepared using air as oxidizing agent was deteriorated within three days, while those prepared using concentrated nitric acid, as oxidizing agent, were stable with time and had low reverse current (see fig.7). It is also noticed that gold forms stable rectifying contact with p-type silicon. The main defect of this contact was that the reverse current is higher than that in aluminium contact. Mathew et al. have noticed that gold silicon barrier is weak and unstable. This observation may be attributed to the short exposure time (10 mins) of silicon crystal to the oxidizing agent (HNO_3 conc.).

Table 1 shows the noise contribution of the amplifier-detector system. The high total noise in case of forward biasing in p-type may be attributed to the following: 1) The noise of undepleted silicon which is clear from the results of capacitance measurements (fig. 8). 2) The non-complete charge collection compared to the reverse direction of the same detector. 3) The weakness of the barrier of the prepared detectors.

The energy resolution for α- particles was measured (see tables 2 and 3). It is clear from the tables that the measured values of the energy resolution depends primarily on the detector thickness and the energy of the incident particle. The large difference between theoretical and experimental energy resolution may be due to the absence of exact theory which explains energy

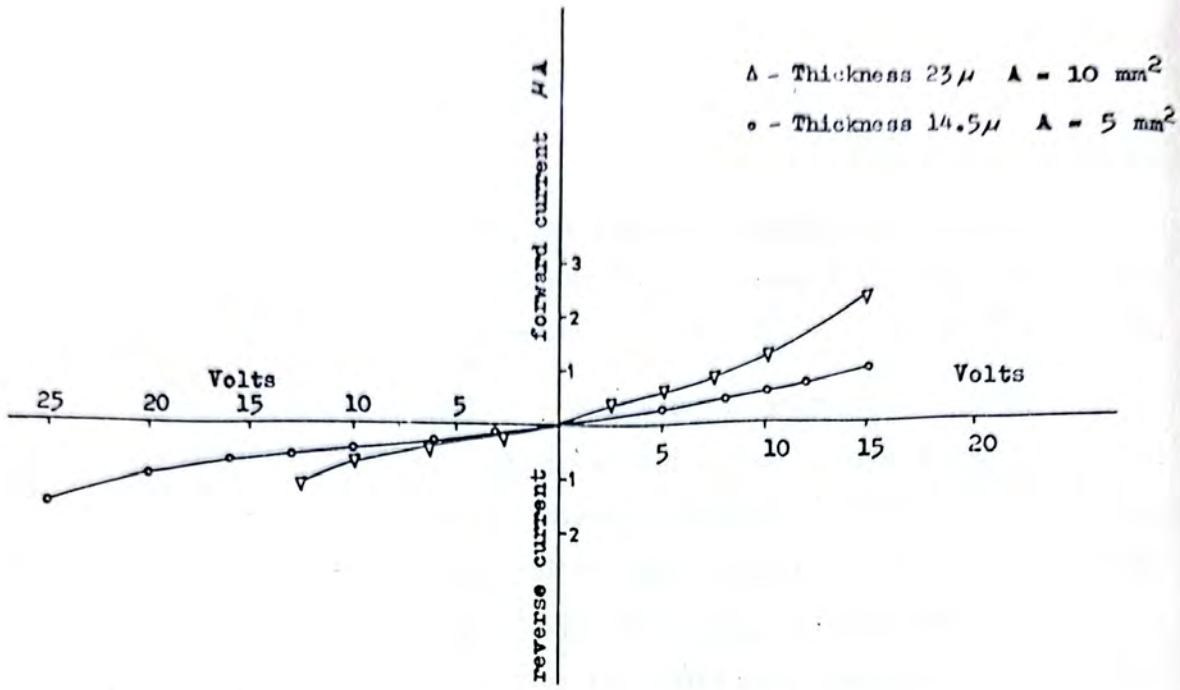

Fig. 5. I-V characteristics of p-type detectors.

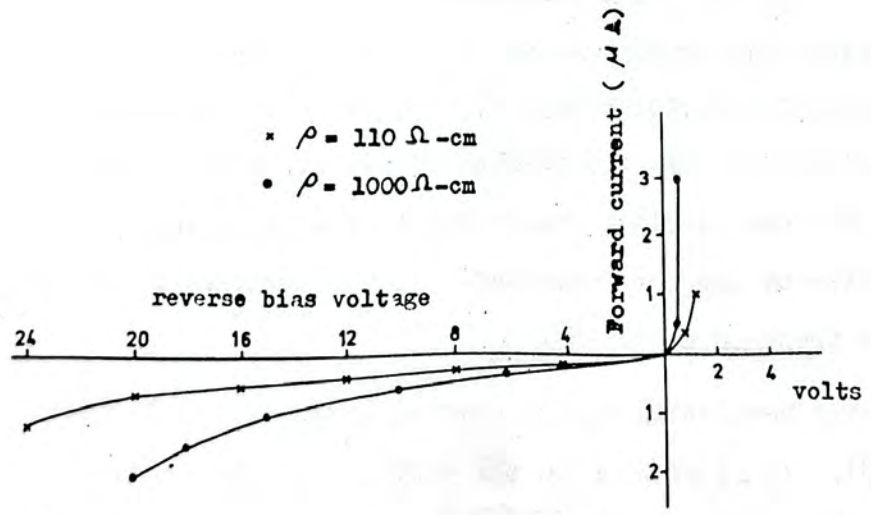

Fig. 6. Current-voltage characteristics of n-type detectors.

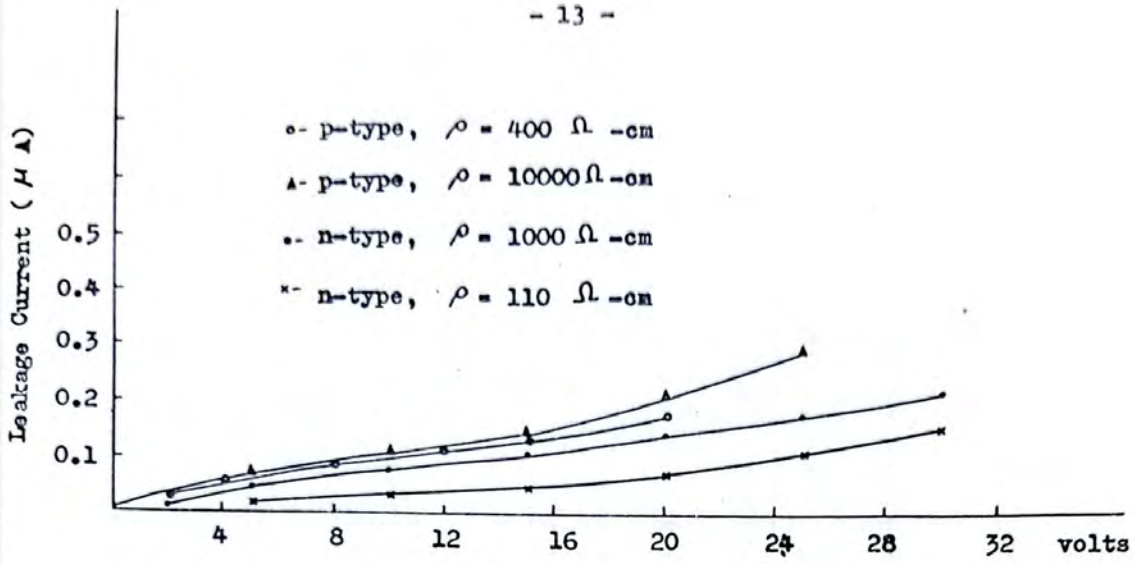

Fig. 7. Reverse current versues bias voltage.

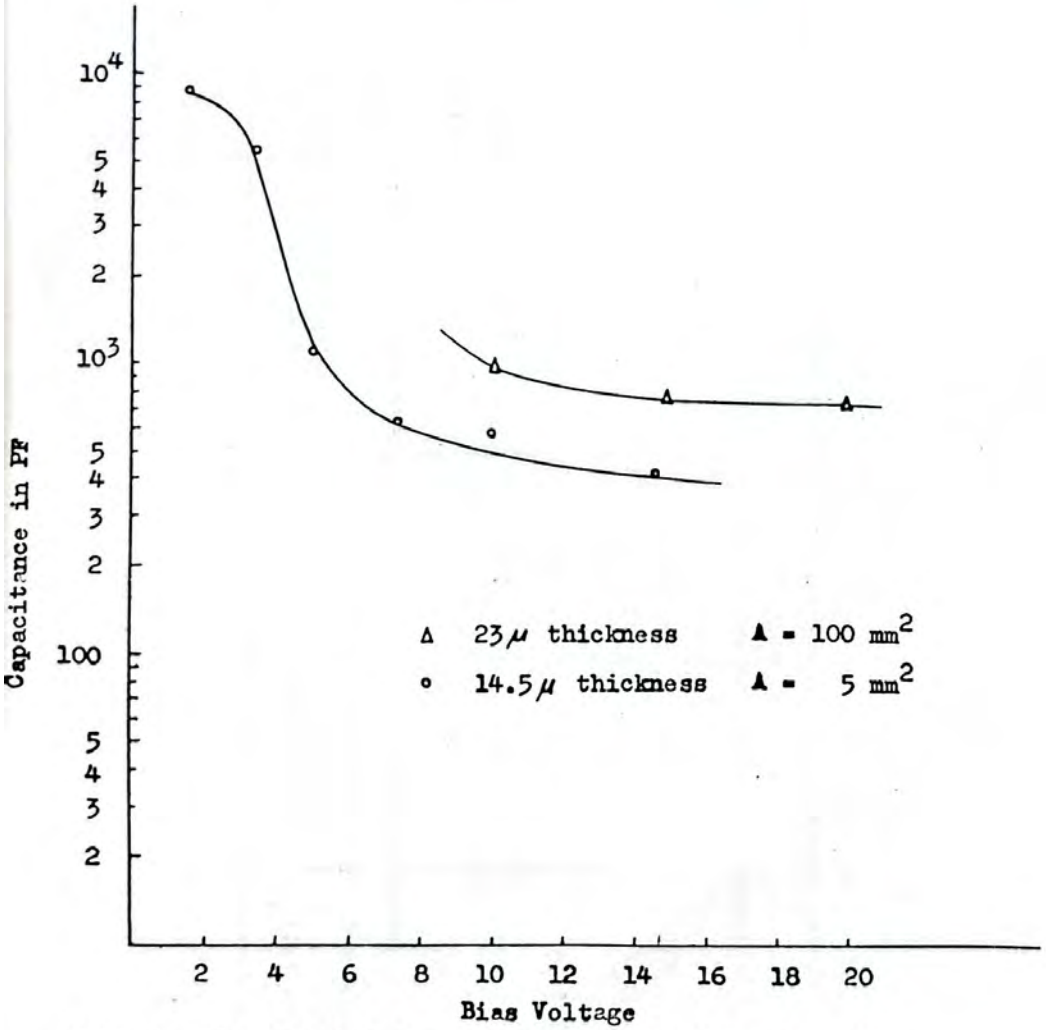

Fig. 8. Forward C-V characteristics of p-type detectors.

Detector thickness (μ)	Detector type	Detector capacity (P.F)	Leakage* current noise (Kev)	Bias resistor noise (Kev)	Residual noise of reverse bias(Kev)	Total noise reverse (Kev)	Total noise of forward bias (Kev)
12.3	p-type	350	9.88	6.8	30.7	32	80
13.3	n-type	380	5.8	6.7	32.8	34	—
14.5	p-type	85	10.9	6.7	16.5	21	56.4
19.8	n-type	280	10.05	6.7	30	33	--
23	p-type	330	11.6	6.7	27.95	31	140

Table (1) : The experimental and theoretical noise of p and n-type detector as a function of detector thickness.

* Theoretical noise calculated from reference[12].

E_α = 5.486 Mev	Theoretical Energy Resolution (Kev)				Experimental	Operating Bias
Detector thickness (μ)	Behr	Cranshaw	Tschalar	Tschalar Beth-Livig.	Energy Resolution (Kev)	voltage (volts)
12.3	70.8	80	80.5	93	154.6	10
13.3	73.6	83.5	84	97	172	20
14.5	76.9	87	89	103	187	12
18	85.7	100	104.5	120.6	248	15
19.8	90	106	118.4	136.6	292	15
23	97	117	143.6	167	380	10

Table (2) : Experimental and theoretical energy resolution of detectors as a function of detector thickness at 5.486 Mev alpha particle.

E_a = 7.68 Mev Detector thickness (μ)	Theoretical Energy Resolution (Kev)				Experimental Energy Resolution (Kev)	Operating Bias Voltage (Volts)
	Behr	Cranshaw	Tschalar	Tschalar Beth-Livig.		
12.3	70.8	79.5	75	86.5	146	10
13.3	73.6	83.0	76.9	88.7	160	20
14.5	76.9	86	80	92	177	12
19.8	90.0	105	98	113	256.5	15
23	97	113	111	128	297	10

Table (3) ; Experimental and theoretical energy resolution of detectors as a function of detector thickness for E_a = 7.68 Mev.

loss process as well as to the nonuniformity in the detector thickness. Two typical spectra of Am^{241} alpha particle source of energy 5.486 Mev detected by ΔE detector of thickness 14.5 μm for forward biased and reverse biased voltages are shown in figures 9 and 10 respectively.

CONCLUSIONS

1. Techniques have been developed for fabricating thin detectors of thickness variation 0.4 um.

2. The obtained results are not in much difference with the previous ones. This indicates that either the theories need to be developed further or the technique of detector fabrication need to be improved.

3. It is noticed that gold-silicon barrier has very good stability.

ACKNOWLEDGMENT

The authors would like to thank Dr. T.A. Hindia for many helpful discussions. The financial support given by the University of Baghdad to one of the authors, namely, T.M. Al-Ardawi is acknowledged with thanks.

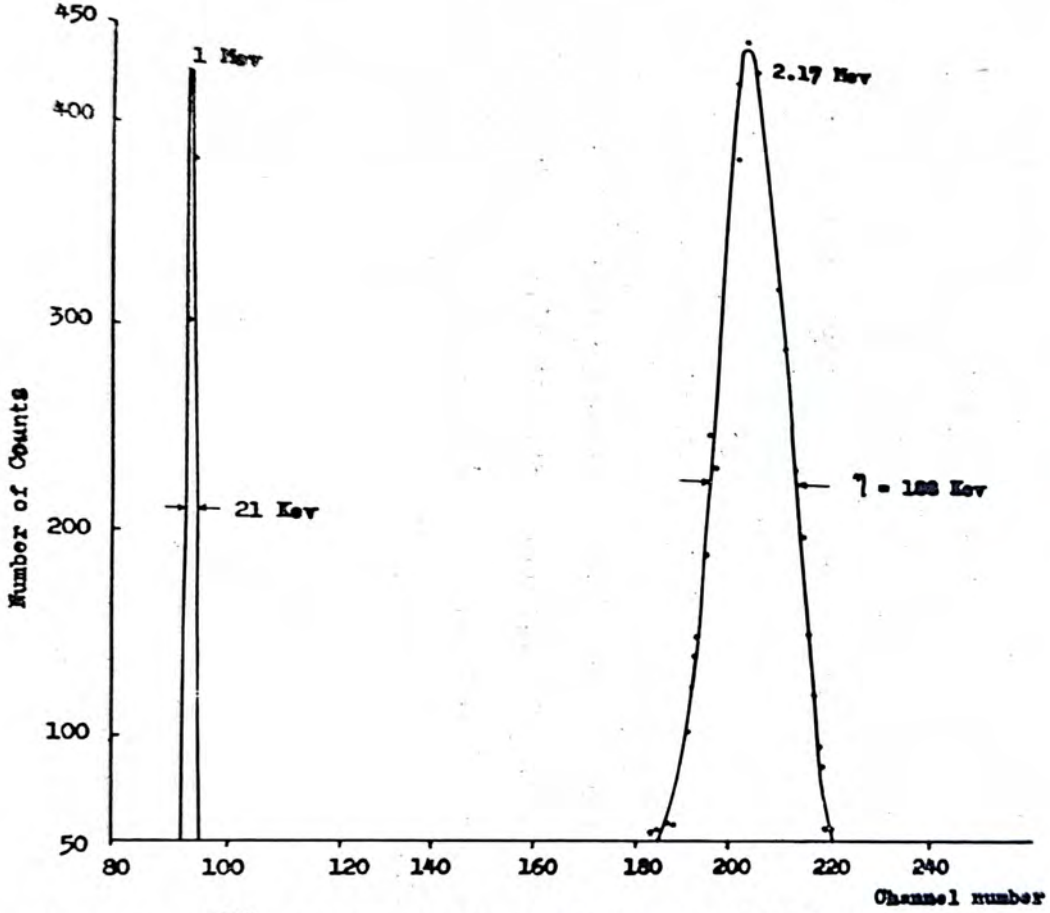

Fig. 10. Am^{241} spectrum detected by Si detector of thickness 14.5μ Reverse-biased.

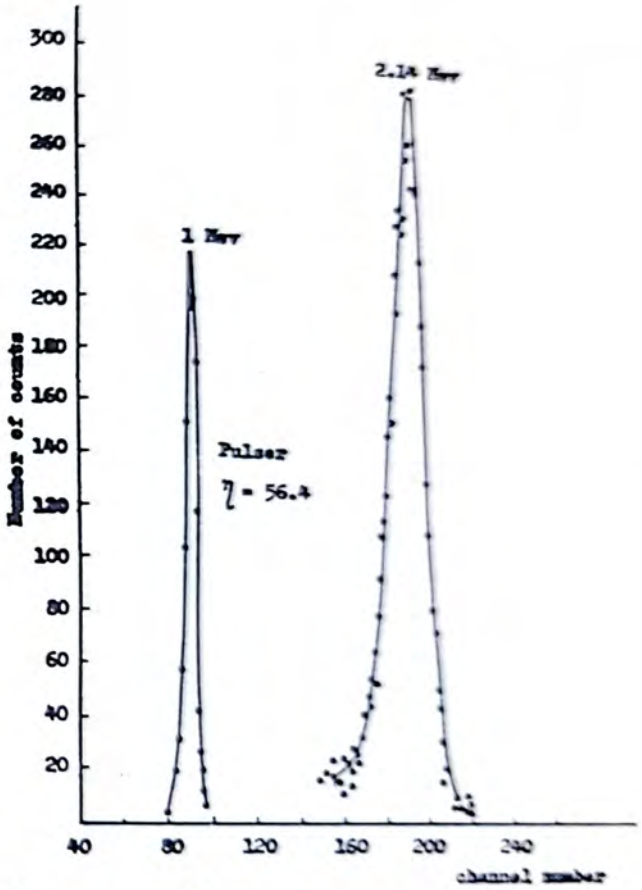

Fig. 9. Am^{241} spectrum detected by 14.5μ detector forward biased.

REFERENCES

1. P.L.F. Hemment and P.R.C. Stevens, J. of Sci. Inst. (J. of Phys.E)., Series 2, 2, 19 (1969).
2. G. Fabri and G. Redelli, Nucl. Inst. and Meth. 35, 130 (1965).
3. G. Anderson - Lindstron and, Zausig, Nucl. Inst. and Meth., 40, 277 (1966).
4. T.C. Madden and W.M. Gibson, IEEE Trans. on Nucl. Sci., 11, 3, 254 (1964).
5. C.N. Inskeep, W.M. Eidson and B.A. Lasalle, IRE Trans. Nucl. Sci. NS. 9, 167 (1962).
6. J.H. Elliot and R.H. Phel, Rev. Sci. Inst., 33, 713 (1962).
7. D.H. Mash, G.D. Henshall and B. Bales, J. of Phys. D. 1199 (1970).
8. J.P. Ponpon and P. Siffert, Nucl. Inst. and Meth., 112, 465 (1973).
9. Osborn C.M., Electrochemical Society, 121, 9, 1195 (1974).
10. G. Dernally and D.C. Morthrop, Semiconductor Counter for Nuclear Radiation (E and F.N. Spon, Ltd. London, 1963).
11. L.P. Anderson and S. Berg, Nucl. Inst. and Meth., 108, 435 (1973).
12. J.S. Fleming, Nucl. Inst. and Meth., 127, 221 (1975).

الخلاصـــــــــــــــة

لقـد تم تصنيع عـدد من الكاشفات الاشعاعيـة الرقيقة من النوعيـــــن n و P لبلـورات السيليكون شـبه الموصلـة بسمك يتراوح ما بين ١٢ الـــــى ٢٣ ميكرون ، وقـد استخدمت طريقة ميكانيكية بواسطة محرك يحتوى على صفيحـة افقيـة دوارة مغطـاة بصفيحـة زجاجيـة تحتوى على حبيبات Al_2O_3 باحجـام معلومـة لبرادة وتنعيـم وجهـي البلـورة ولا زالـة الخدوش الناتجة عند عمليـة القطـع. وبعد معاملة البلـورة بواسطة محاليـل كيمياوية حيـث تجرى عمليـــة التآكـل فيها وتصقـل الى سمكها النهائي ومن ثم تثبيتها على اطـار خاص صنـع لهذا الغـرض من مادة لافـا . وبعد تبخيـر الذهب والالمنيوم على وجهـــي البلـورة يصبح الكاشـف معـد للعمـل .

وتمت دراسة الخواص النظرية والعملية لهذه الكاشفات وتبين من دراســـة علاقـة التيـار العكسي مع الجهد المسلط للكاشفات من النـوع P ان سـلوك اتصال الذهب مـع السيليكون لم يكن اوميـا كما هو المتوقـع من الناحية النظريـة بـل كان سلوكـا معـدلا ، وهذه الظاهرة لا يمكن تفسيرها بدون اعتبار طبقـة اوكسـيد السيليكون كعـازل فعال في هذه الناحيـة. وعند دراسة التمييز الطاقي لهذه الكاشفات بواسطة اشعة الفا ذات طاقـة ٤٨٦ر٥ ، ٦٨ر٧ ميكا اليكتـرون فولت تبين ان هناك اختلافـا كبيرا بين النتائج النظريـة والنتائـج العملية كمـا ان هناك اختلافـا محسوسا بين النتائج العملية التي حصل عليها الباحثون اضافـة الى اختلافهـا الكبير مع النتائج النظريـة ايضـا . ويمكن تفسـير جميع تبريرات هـذا الاختلاف كنتيجـة لعـدم التجانس في سـمك الكاشـف المسـتخدم .

STUDIES ON THE EVAPORITE OCCURENCES ALONG THE COASTAL PLAIN, WEST OF ALEXANDRIA, A.R.E.*

Part - I

Geochemical and Mineralogical Studies,

M.E. HILMY, S.A. HUSSEIN, S. HASSAN
Faculty of Science, Ain Shams University,
Cairo, EGYPT.

A B S T R A C T

Several Pleistocene and Holocene evaporite were recorded in the coastal plain Region of Egypt. The Pleistocene evaporites are found in the form of some alternating gypsum and marly layers, while the Holocene evaporites occur as marshy or Mallahet deposits. At the same time, a bore-hole drilled on the area, was described, where gypsum beds of Miocene age were detected. These evaporites were studied in detail from different points of view. Part-I of this study is devoted to the geologic occurence, geochemistry and mineralogy of these deposits. Gypsum is the main evaporite mineral in the Pleistocene deposits, with some contaminations of other minerals, e.g. dolomite, calcite, halite and anhydrite. The main salt separated from the Holocene ponds is halite with minor amounts of potassium and magnesium salts. Traces of gypsum may also precipitate together with halite in the ponds.

The distribution of trace elements in the different evaporite deposits was also discussed.

---

* This study represents a part of M.Sc. Thesis presented by the third author, under the supervision of the first and the second authors. It was submitted to the Faculty of Science, Ain Shams University, Cairo, in 1977.

INTRODUCTION

The Mediterranean Coastal Zone, west of the Nile Delta, received much attention as a territory where land reclamation for agricultural expansion, can be conducted on a wide scale. Previous workers on the coastal zone, were mainly concerned with its geomorphology and hydrogeology, e.g. Fourtau (1893), Blanckenhorn (1901 and 1921), Hume and Hughes (1921), Hume and Little (1928) Andrew and Cuvillier (1938), Ball (1939), Sanford and Arkell (1939) Picard (1943), Shotton (1946), Schwegler (1948), Hilmy (1951), Paver and Pretorius (1954), Shata (1955), Shukri et.al. (1955-1956) Said and Kamel (1957) and Abdullah (1966).

More recently, several authors took over studies of the coastal zone from hydrogeological and pedological points of view, e.g. Shata and Co-workers (1953-1970), El-Shazly (1964), Hammad (1966 & 1972), Harga (1967), El-Shamy (1968), Attia (1975)....etc.

In the above literature, little information can be found about the evaporite deposits in the coastal zone. However, a good information of regional importance about the whole Coastal Zone can be found. The present study deals with the mineralogy, geochemistry, and petrography of the evaporite deposits encountered in the coastal section, between west Alexandria and El-Alamein area.

Part-I includes the geology, geochemistry and mineralogy of the evaporites, while Part-II discusses the petrography and the environmental conditions of sedimentations.

For the present work four areas were chosen for the study of the evaporite occurences in the coastal region and the nearby localities. Three of these areas are where gypsum is extracted for the manufacture of plaster of Paris, these are : El-Gharbaniat, El-Hammam and El-Imayi

The fourth area is a new one and is under preliminary investigations, this is El-Barqan. Beside these four main localities of evaporite deposits, ether marshy lake or Mellahat deposits were attempted also in the present study.

Location

The area in which the major portion of the present investigations were undertaken, extends from west of the city of Alexandria to the village of El-Alamein, and occupies a strip of country varying between five and forty Kilometers wide along the northwestern portion of the Mediterranean Coast of Egypt.

This distance by road between these two extremeties of the studied area is approximately 110 Kilometers, and stretches generally in an east-west direction.

The northern limit of the area is delineated by the Mediterranean shore-line and the southern limit is approximately demarcated by the 100 m Contour line above sea level. The whole area of investigation is contained between longitudes 29° and 30° E and around latitude 29° N., (Fig. 1).

Stratigraphic position of the evaporite deposits

The Mediterranean Coastal Zone is totally occupied by sedimentary rocks belonging to Quarternary and Tertiary Eras (Fig.2).

The surface succession, having a thickness of about 200 m , is dominated by limestone. The subsurface borings for oil exploration in area of study show that there is a thick sedimentary section (± 500 m) belonging to the Tertiary and pre-Tertiary Eras (including

Fig. (1) Location map

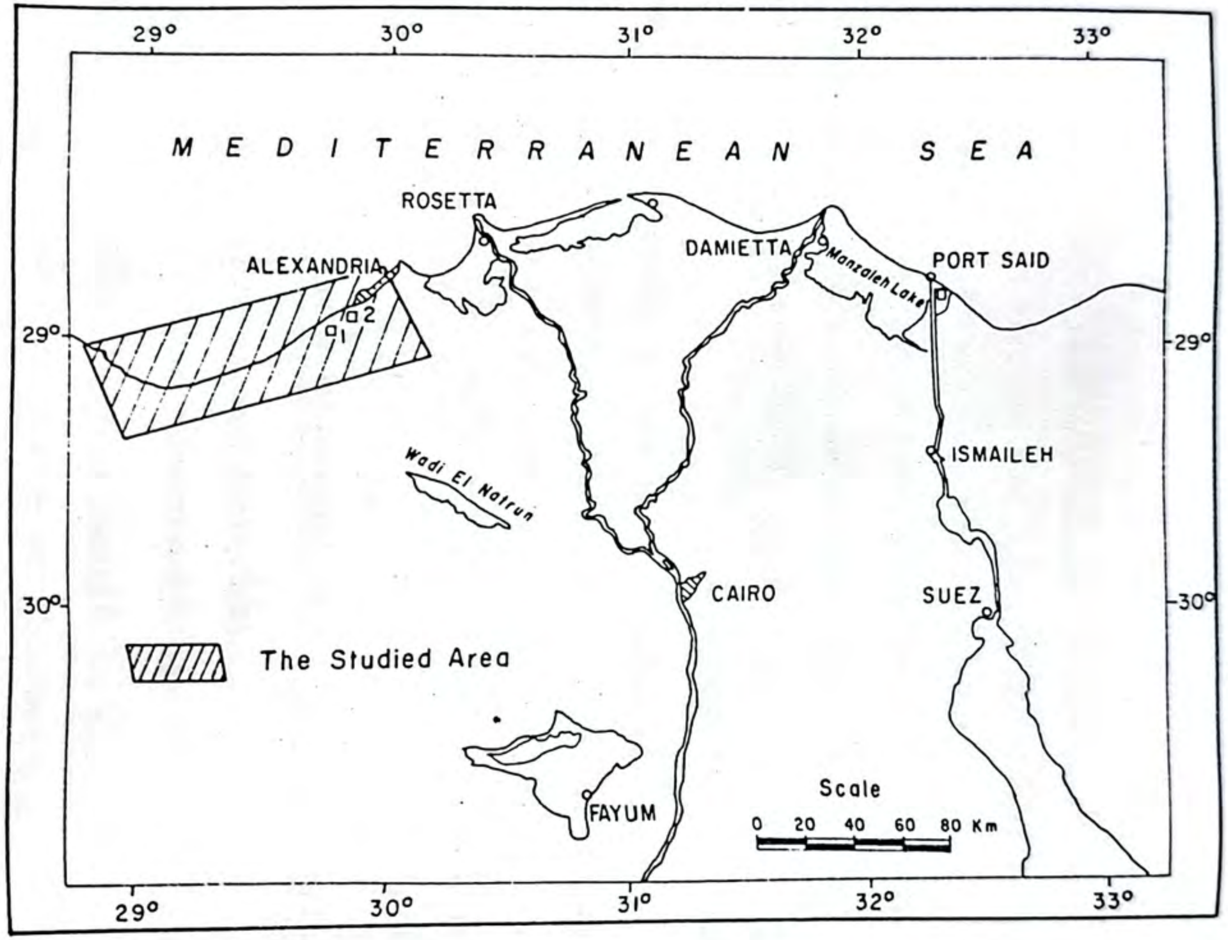

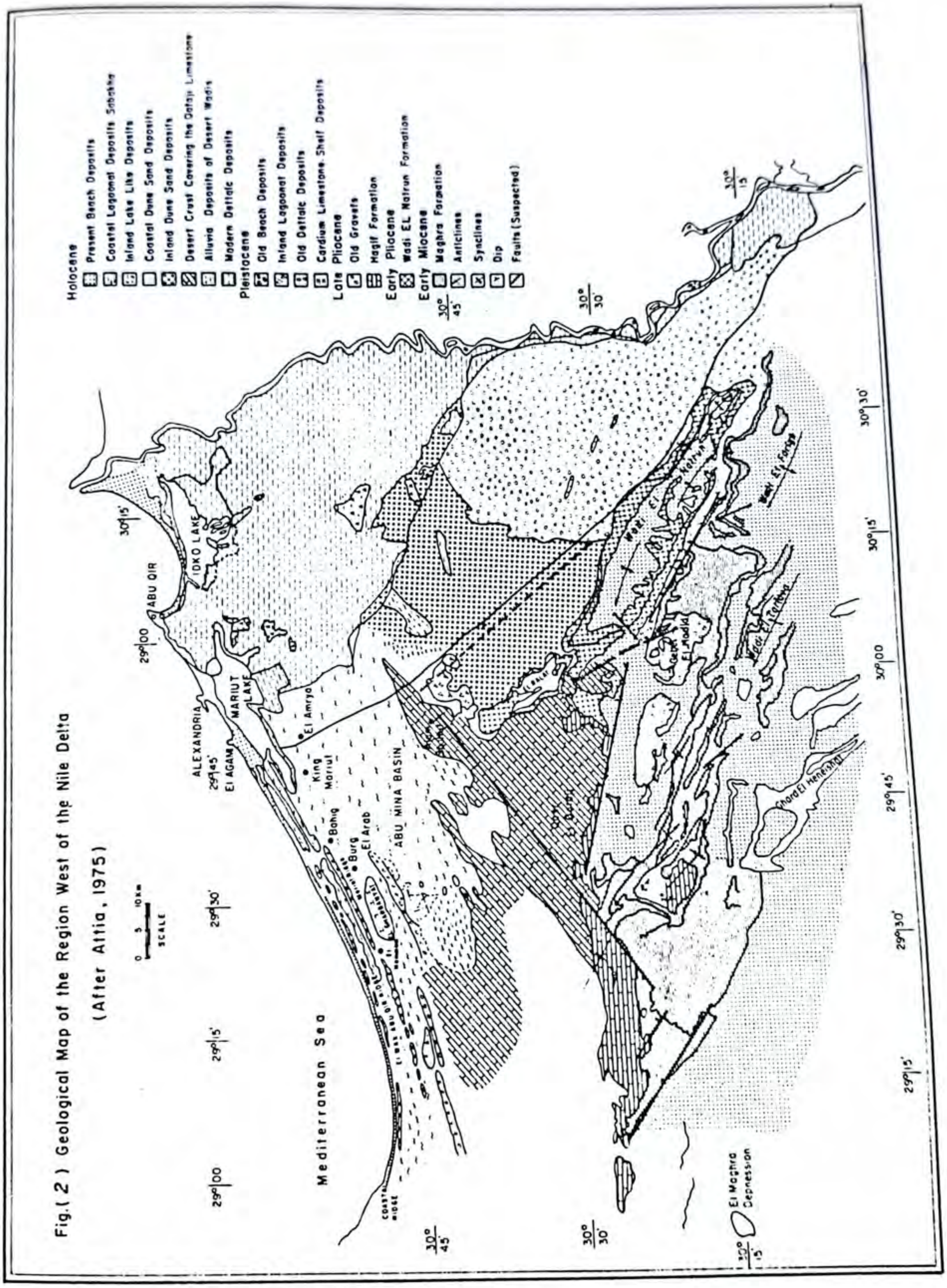

Fig.(2) Geological Map of the Region West of the Nile Delta

(After Attia, 1975)

Paleozoic and Mesozoic). The general succession of the stratigraphic sequence of the coastal zone, compiled by the authors from different sources in the literature, can be summarized in Table (1) from top to base.

Table (1) shows that the evaporite deposits in the area under investigation, belong to Pleistocene (gypsum formation) and Holocene (marshy deposits). The Pleistocene gypsum formation is found in an evaporite series composed of alternating gypsum and marly layers. Philip (1955) distinguished seven of gypsum layers alternating with seven layers of clay, these alternations indicate seven periods of dryness with seven wet periods inbetween.

The Holocene marshy deposits are mainly found in Mallahet Maryut and its extension. These deposits are formed of slightly compact saline calcareous mud. They become compact and more saline with increasing depth. Weathered and down-washed materials are found admixed with salts produced by evaporation of brackish water near the surface.

Beside the Pleistocene and Holocene evaporite occurrences, a bore-hole drilled on Abu-Sir ridge at El-Alamein, was described, where gypsum beds of Miocene age were detected (Hammad, 1972). This boring was made by Desert Institute for ground water investigation in this area.

Geomorphological aspects

From a geomorphological point of view, the western Mediterranean littoral zone can be subdivided into the following geomorphic units (Fig. 3).

Table (1): The Stratigraphic Sequence of the Coastal Zone (Compiled by the the Authors)

Age	Type of sediments	Thickness
Quaternary:		
a) Holocene:	1. Beach deposits	variable
	2. Drift sand	variable
	3. Lacustrine	5 m
	4. Limestone crust	variable
	5. Alluvial deposits	5 m
	6. Marshy deposits	variable
b) Pleistocene:	1. Alluvial terraces	variable
	2. Oolitic limestone	40 m
	3. Cardium limestone	5 m
	4. Gypsum formations	3 m
c) Plio-pleistocene	1. Kataji limestones	5 m
	2. Pink limestone	variable
Tertiary:		
a) Pliocene:	Creamy limestone	38 m
b) Miocene:	1. Chalky limestone	25 m
	2. Clayey limestone	variable
	3. Marl	"
	4. Clay	"
	5. Marl	"

Fig. (3) Map showing the main landforms in the coastal plain to the west of Abu Qir headland (after Attia, 1975)

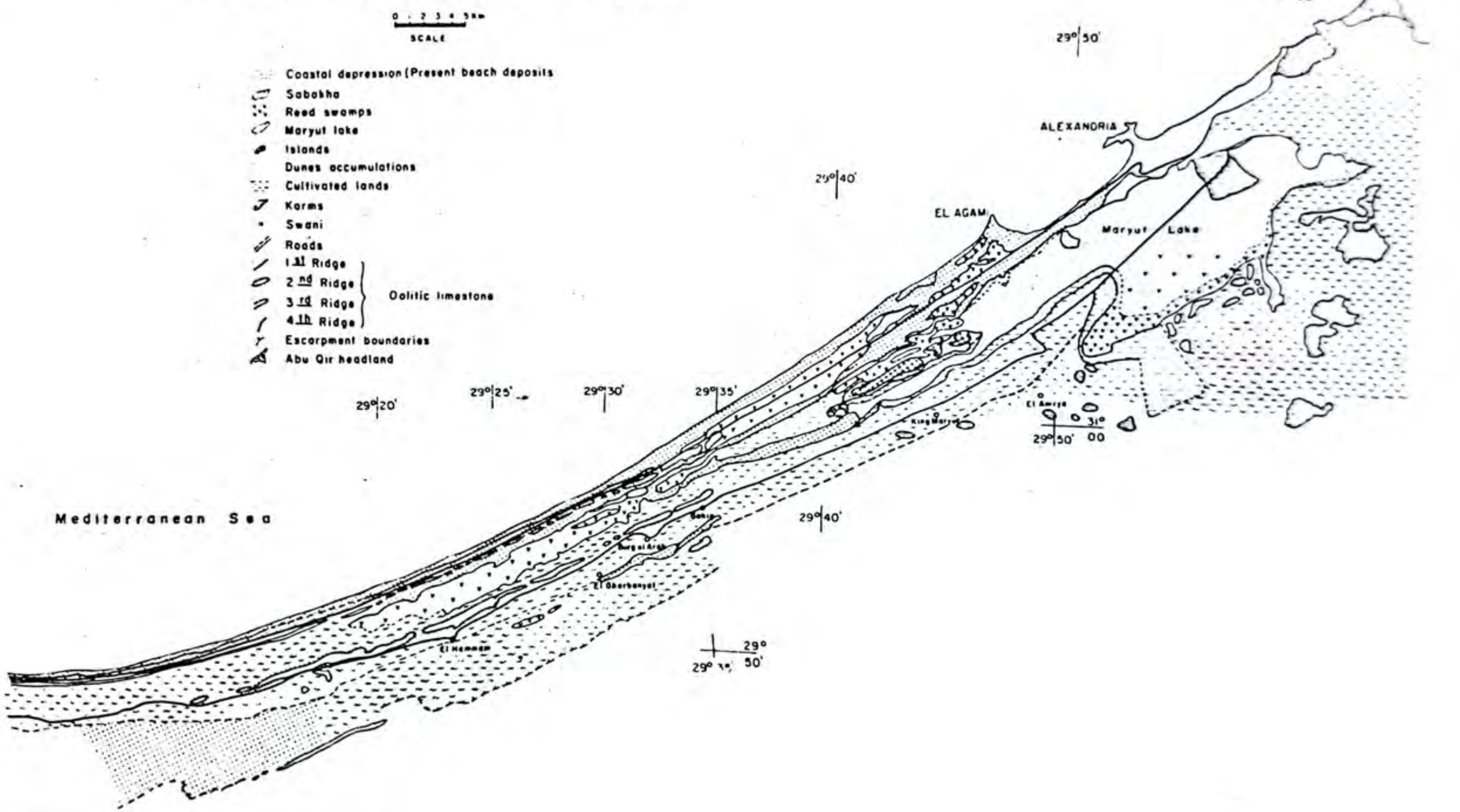

1- The Coastal plain

This plain extends parallel to the Mediterranean Coast and runs in an E-W direction for a distance of about 150 Km. Its width is much variable, stretching southwards from few meters to about 10 Km. In this plain, land features resulting from constructional as well as destructinal processes are demonstrated. The Coastal plain can be subdivided into young coastal plain (Recent) and Old coastal plain (Pleistocene). The latter plain consists of limestone ridges alternating with several shallow depressions.

The fore-shore elongate ridges run in NE-SW direction, i.e. parallel to the Mediterranean Coast. These ridges are (from north to south) : the coastal ridge, El-Max - Abu-Sir ridge, Gebel Maryut ridge, Khashm El-Eish ridge, Alam El-Khadem ridge, El-Mikherta ridge, Raqabet El-Halif ridge and Alam Shaltud ridge.

The fore-shore elongate depressions are generally parallel to the above-mentioned ridges and described by Philip (1955) as lagoonal depressions filled with calcareous loamy deposits. These depressions include: the coastal depression, Matar el-Dehkeila - Abu Sir depression, Mallahat Maryut depression.

2- The Piedmont plain

This plain is represented by the area between Gebel Maryut ridge in the north and Maryut table land in the south. The plain varies in width from 3-6 Km. Its surface elevation varies between 10-20 m above sea level. The surface of the Piedmont plain is covered with alluvial deposits and calcareous loamy soil overlying an evaporite series.

3- Maryut table land

It lies south of the coastal plain and extends southwestward to merge gradually in the western Desert plateau. It is 75 Km long and has an average width of 4 Km. and a maximum height of about 110 m above sea level. Its surface is composed of limestone,

4- Abu Mina Basin

This represents the depositional valley draining the table land area, and lies south of the Coastal plain and east of the table land. It traverses the Maryut table land and slopes gradually in a N-E direction. It occupies an area of about 500 square kilometers. Its surface is covered with good soil suitable for cultivation which derived from the adjacent table land.

From the evidences gathered in the field, it was found that most of the Pleistocene gypsum deposits in the coastal area, occur in the longitudinal depression between the second and third ridges (Abu Sir and Maryut ridges). El-Barqan gypsum occurrence lies in the depression behind the fourth ridge. These ridges and depressions are parallel to the coast of the Mediterranean Sea. From the distribution of evaporites, it is clearly observed that the deposition of evaporites is of a regional rather than strictly local characteristic This indicate that the gypsum was deposited by evaporation from ancient lagoons. These lagoons were formed during the marine transgression of the Middle Pleistocene, where the Mediterranean Sea invaded the coastal areas behind the first and second ridges, and on its consequent regression the lagoons so formed in the depressions The ridges acted as a bars, separating the shore lines from the lagoons.

Shukri et al. (1956) identified nine main bars (or ridges) separated by seven lagoons. From the ages of these bars and the lagoons, the same authors were able to configurate the shore lines of the Mediterranean Sea in the Pleistocene times, Fig. (4).

The marshy deposits (Holocene) occur in a number of salt pans which are found in the basins and depressions located in the studied area. These pans depend mainly on rain mater for dissolution of the residual salts (i.e. Lake Maryut) together with minor sea seepage. Rain falling on the higher parts of the area flows into the depression of these natural pans. The water accumulating is left to dissolve the residual salts and then to evaporate leaving behind a crust of salts.

Measured sections and sampling

Five sections were measured, described and sampled from the evaporite successions in the following areas :

El-Hammam - A and El-Hammam - B (two quarries), El-Imayid, El-Gharbaniat and El-Barqan.

The location of these sections are shown in Fig. (5), while Fig. (6 - a,b,c,d,e,) shows the description of these sections. Fig. (6-F), shows description of the succession encountered in Abu-Sir subsurface section (MIOCENE).

About "100" selected samples were collected from the measured sections for the present study. The following table (2) is a summary of sampling sites and sample number for collected samples.

Geochemistry of evaporite deposits

In order to get information about the conditions under which the evaporite rocks were formed, a study was made to investigate and

Fig.(4) Main shore lines bordering coastal plain of Egypt from Mousterian to Sicilian stages

(after Shukri et al , 1958)

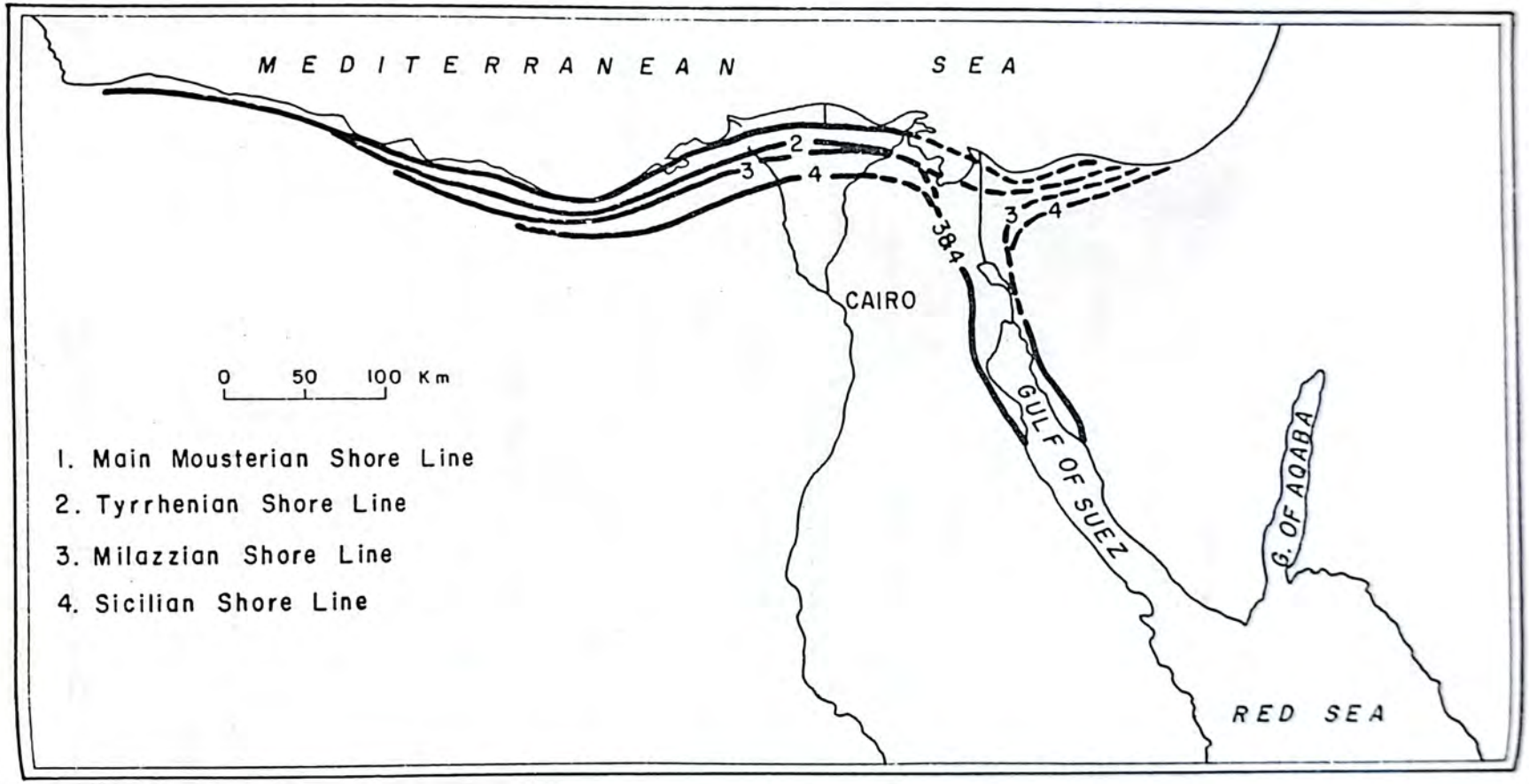

Fig. (5) Index map showing the location of the collected samples

Scale = 1 : 500.000

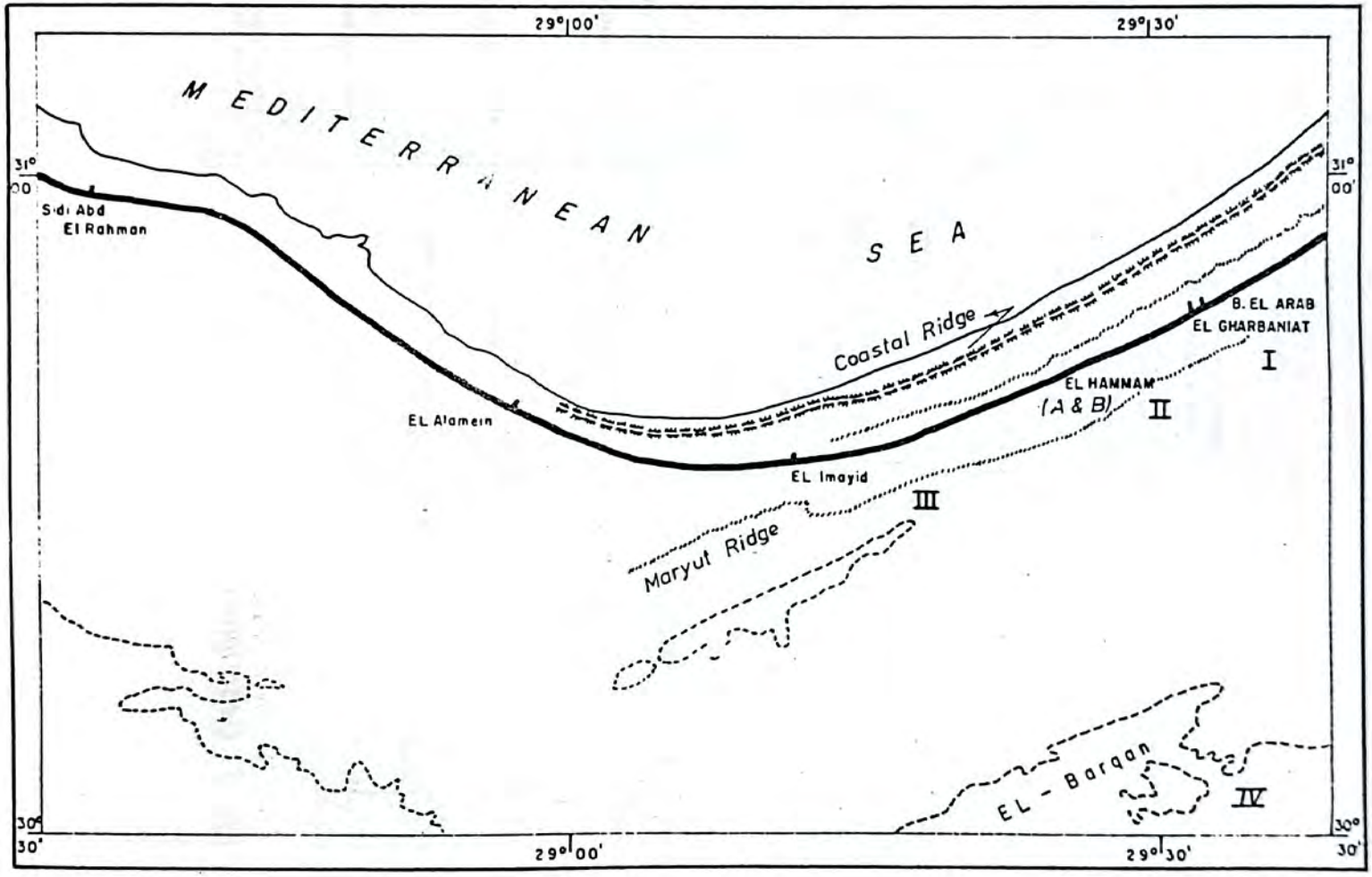

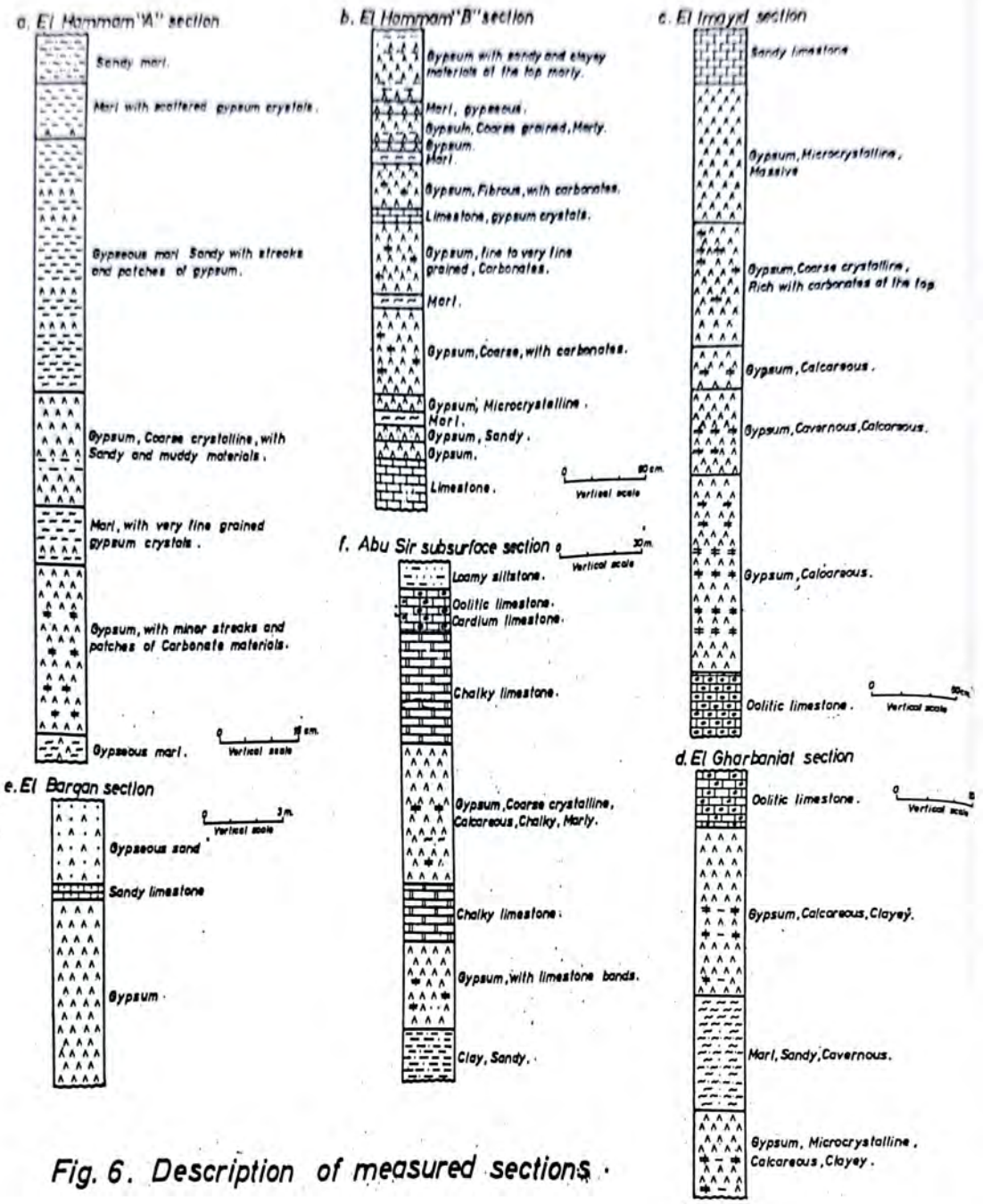

Fig. 6. Description of measured sections.

Table (2) Sampling Sites and Number of the Collected Samples

Sampling sites	Sample number
1. El-Hammam-A section	I-1 to I-6
2. El-Hammam-B section	II-1 to II-15
3. El-Imayid section	III-1 to III-6
4. El-Gharbaniat section	IV-1 to IV-6
5. El-Barqan gypsum	V-1 to V-5
6. El-Barqan limestone	L-1 to L-3
7. El-Barqan cavity fillings	C-1 to C-5
8. El-Barqan gypsum sands	G-1 to G-5
9. Subsurface gypsum samples at Abu-Sir ridge	A-1 to A-7
10. Salt-samples	S-1 to S-30
11. Water samples	WS-1 to WS-5

determine the chemical composition of these rocks and discuss the interrelation of their constituents. Also an attempt is made to calculate the mineral phases in order to follow variations in the evaporite mineral associations in rock samples.

Eleven different gypsum samples were selected for chemical analysis, to represent nearly most of the different types of evaporite rocks present and the type of contaminations.

Two rock salt samples separated from the brines were selected from the different varieties of saline deposits. Two samples from the brine waters was collected by using polyethelene bottles, capacity one liter. One of these samples represents concentrated brine water without salt crystallization, while the other sample represents the same water after the salts have been precipitated at the floor of the brine. The standard methods of testing rock salts, gypsum and gypsum products are used in the chemical analyses of these samples (Welcher, 1958, Kolthoff and Sandell, 1936).

Chemical Composition of gypsum and gypsum-bearing rocks

The results of the chemical analysis of gypsum rocks are given in tables 3,4 and illustrated graphically in Figs.7 and 8.

The results of the chemical analysis show that:

1- El-Barqan deposit shows the most pure gypsum present in the studied area. Two analyzed samples from this deposit show a percentage of about 98.00% gypsum ($CaSO_4 \cdot 2H_2O$), with trace of carbonates, halite, and silica (2%).

2- In other localities, gypsum ranges between 48% (subsurface Abu-Sir samples, A-5) to about 94% (El-Hammam samples, I-

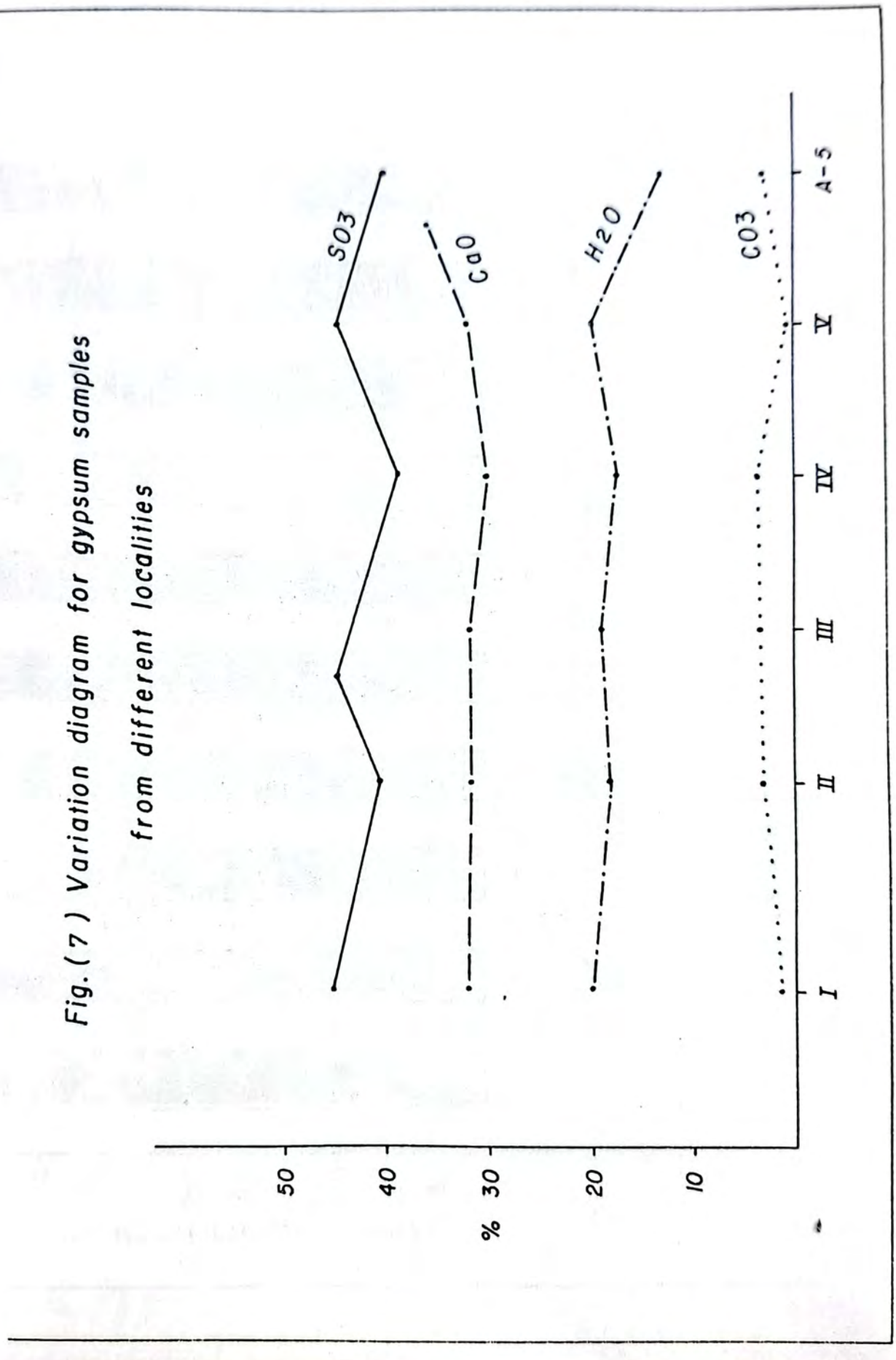

Fig. (7) Variation diagram for gypsum samples from different localities

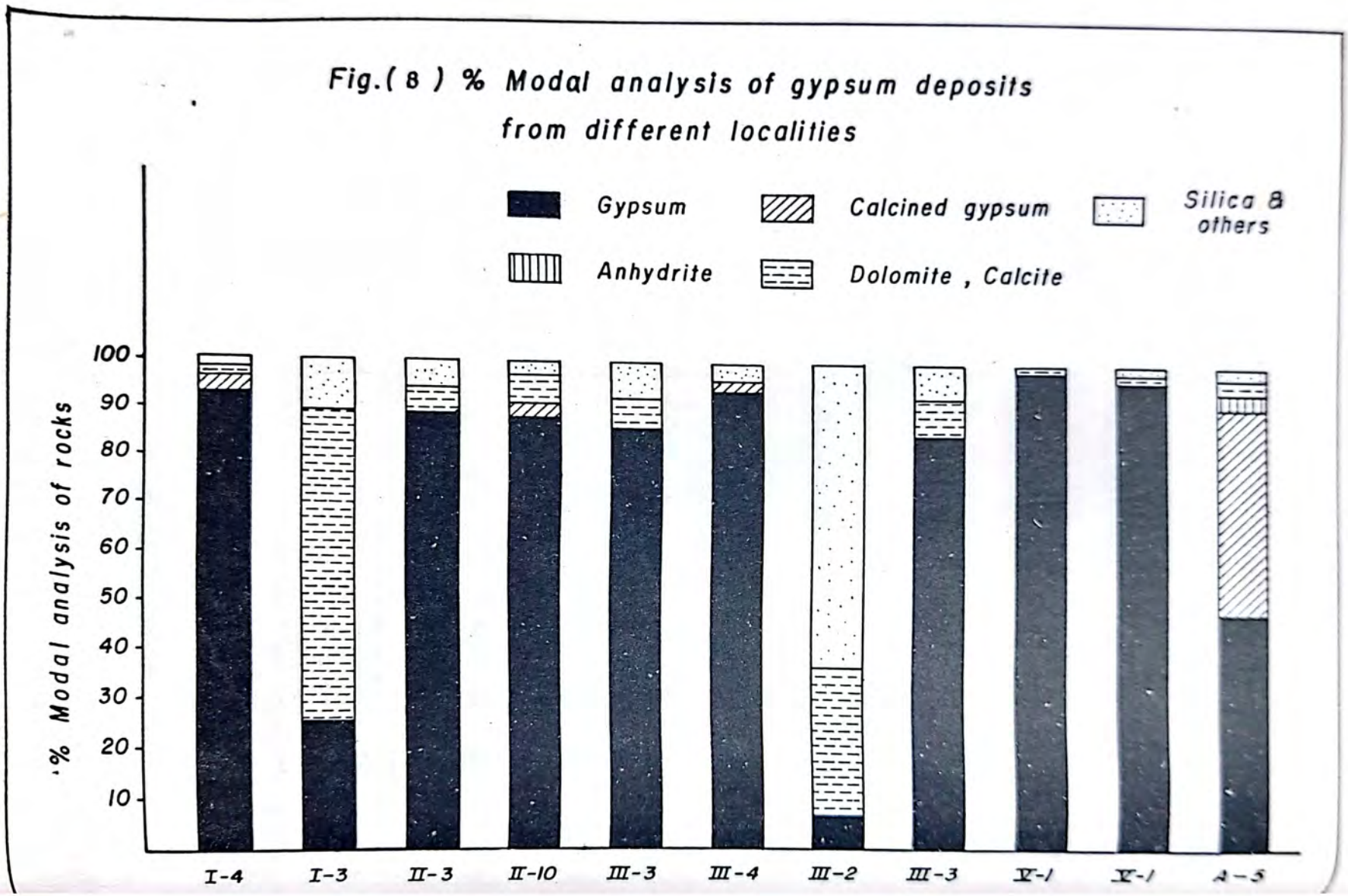

Fig.(8) % Modal analysis of gypsum deposits from different localities

Table (3) : Chemical analysis of gypsum samples.

Sample No.	V-1	V-1¯	1-4	III-4	II-3	II-10	III-3	IV-3	A-5	I-3	III-2
H_2O	20.00	20.21	20.01	19.55	18.50	18.61	18.41	17.90	13.54	5.78	2.64
S O3	45.99	45.14	45.96	45.16	41.20	43.26	39.40	39.30	41.22	11.90	2.66
CaO	32.70	32.50	32.66	32.40	32.00	32.40	31.02	30.50	36.66	28.01	16.05
MgO	trace	trace	0.02	trace	1.37	1.36	1.58	1.43	1.38	14.22	3.11
CO_3	00.86	0.41	0.82	0.62	3.01	3.01	3.28	3.11	3.01	30.14	13.86
SiO_2	0.24	0.22	2.12	2.10	2.70	1.10	4.60	3.80	2.83	4.50	28.05
R_2O_3	-	-	-	-	0.44	-	0.68	0.50	0.45	1.40	32.21
NaCl	0.14	1.40	0.35	0.14	0.28	0.10	0.87	3.42	0.34	3.54	1.50
Total	99.93	99.88	101.94	99.97	99.50	99.84	99.84	99.96	99.43	99.49	100.08

Table (4): The approximate amounts of the evaporite minerals as calculated from the chemical analysis data

Sample No.	V-1	V-1¯	I-4	III-4	II-3	II-10	III-3	IV-3	A-5	I-3	III-2
Gypsum	98.00	97.12	93.02	94.00	89.28	88.02	88.40	85.22	48.00	25.50	6.88
Cleined gypsum	-	-	3.00	2.00	-	3.25	-	-	43.00	-	-
Anhydrite	-	-	-	-	-	-	-	-	2.02	-	-
Calcite	1.90	-	-	-	-	-	-	-	-	-	16.02
Dolomite	-	1.02	1.70	1.01	5.82	6.08	6.64	7.00	2.48	64.88	13.88
Halite	0.14	1.40	0.35	0.14	0.28	0.10	0.87	3.42	0.34	3.54	1.50
SiO_2	0.24	0.22	2.12	2.10	2.70	1.10	4.60	3.80	2.83	4.50	28.05
Aggregates	-	-	-	-	0.44	-	00.68	0.50	0.45	1.40	32.21

The lower values of gypsum in these gypsum occurrences are due to its contaminations with carbonates (calcite and/or dolomite), SiO_2 and R_2O_3 .

3- The carbonates are the main impurities detected within El-Hammam, El-Imayid and El-Gharbaniat gypsum deposits, (e.g. samples No. I-4, II-3, II-10, III-3 and IV-3). In these samples the carbonates consist mainly of dolomite $Ca_2Mg(CO_3)_2$ with traces of calcite ($CaCO_3$). The percentage of dolomite ranges between 1-7%. The analysis of these calcareous materials separately, shows that they consist of about 16% calcite and 14% dolomite (e.g. sample No. II-2).

4- Samples from the subsurface section of Abu-Sir (A-5), consists of 48% gypsum and about 2% anhydrite. Also some contaminations with SiO_2, R_2O_3, dolomite and halite present.

5- From the chemical point of view a third form of the group $CaSO_4 - H_2O$ is present, it is called calcined-gypsum or hemi-hydrate from (plaster of Paris, bassanite) with a formula $CaSO_4 \cdot \frac{1}{2}H_2O$. Its percentage may reach up to 43.60% (sample No. A-5). According to Khalil, 1966, this form occurs in the calculations of some analysis. This form is generally associated with gypsum rather than with anhydrite. It is not found in nature, and may appear in the chemical analysis due to heating of gypsum.

6- Variation diagram (Fig.7) show the H_2O , SO_3 , CO_3 and CaO variations, from which it appears that El-Barqan samples (V) have high values of SO_3 and H_2O (gypsum) and lower values of CaO and CO_3 (carbonates).

7- Sodium chloride is found generally in all samples, ranging

from 0.10 to 3.54%, the high values is found in the gypseous marl sample (I-3).

8- Modal analysis (Fig.8) shows that these deposits consist mineralogically of gypsum as an essential constituent, with minor amounts of anhydrite, calcite, dolomite, halite, silica and aggregates.

II. Chemical composition of salt deposits and brine water

Two salt samples separated from the brines, together with two brine water samples were analysed. The results are given in table (5) in weight percent.

From table (5) the following conclusions are arrived at :

1- The main salt separated from these ponds is sodium chloride (Na = 38% , Cl = 58%) with minor amounts of potassium and magnesium salts. Minor and trace amounts of gypsum may also precipitate together with halite.

2- The main salts which will be separated from brine waters can be more appropriately studied in the light of the well-known Bunsen-Fresenius conception. According to this conception, the ions of the strong acids (Cl^- , SO_4^{--}) from a chemical combination with alkalies (Na^+,K^+), the rest of these acid radicals combine thereafter, with alkaline earths (Ca^{++},Mg^{++}). If the latter are in surplus in water, they will combine with the weak acids (CO_3^{--} , HCO_3^-).

These relationships can best be represented by means of bar graphs according to the method given by Collin, 1923. The height of the bar is equivalent to the concentration of cations

Table (5): Chemical composition of salts and brines

	S A L T S		B R I N E S			
	1	2	3		4	
	wt%	wt%	g/L	equiv. g/L	g/L	equiv. g/L
Na	37.48	38.01	98.1	4.25	42.8	1.81
K	0.72	0.18	1.5	0.04	9.5	0.24
Mg	0.08	0.01	11.6	0.90	60.5	5.00
Ca	0.01	0.02	0.4	0.03	0.02	-
Cl	57.21	58.46	206.5	5.80	205.0	5.77
SO_4	3.14	1.52	14.5	0.98	50.8	1.11
CO_3	0.04	0.01	0.1	-	0.1	-
WIR*	0.82	0.30				
TDS**			369		422	
Salinity			30		34	
Sp.Gr.			20		1.25	
pH			7		6.5	
R-1			1.36		1.37	

Description of samples:

1. Crystalline salt sample, pure milky white, collected from the floor of the brine.
2. Fine-grained salt sample collected from the borders of the brine.
3. Concentrated brine water without salt crystallization.
4. Brine water with salts crystallized at the floor and at the edges of the brine.

* Water insoluble residue.

** Total dissolved salts.

and anions (equiv. gm/L). The bar is divided vertically into two halves, the right one represents the anion side while the left represents the cation side, (Fig. 9).

Due to the fact that the concentration of cations and anions are equal, when expressed in equiv. gm/L, the possible combinations of these can be read directly from the bar graph.

From the data given in table (5) and Fig. (9), it is apparent that the concentrated brine water before crystallization consists of salt assemblages as follows :

(Na,K) ; $MgCl_2$; $CaSO_4$; while brine waters (after crystallization of salts) consist of : (Na,K) Cl ; $MgSO_4$ $MgCl_2$.

Distribution of trace elements in evaporite deposits

In addition to the chemical analysis in items of major constituents, quantitative spectrographic analysis has been made for "14" samples of evaporite deposits in the area under consideration.

As far as the authors are aware, no previous information is available concerning the distribution of trace elements in the evaporite deposits in the studied area. The results of this investigation are given in Table (6) for gypsum deposits, while Table (7) gives the results of analysis of salts and brines collected from the ponds.

Lithium and barium were determined using a flame spectrophotometer (Perkin Elemer Model 16). Boron was determined spectrophotometerically using carmine method. Bromine is determined using x-ray fluorescene. Furthermore, samples of salts from the concentration and crystallization ponds were subjected to a semi-quantitative spectrographic analysis using a Large Hilger and Wats spectrograph

Fig.(9) Bar graph representation of Salt samples

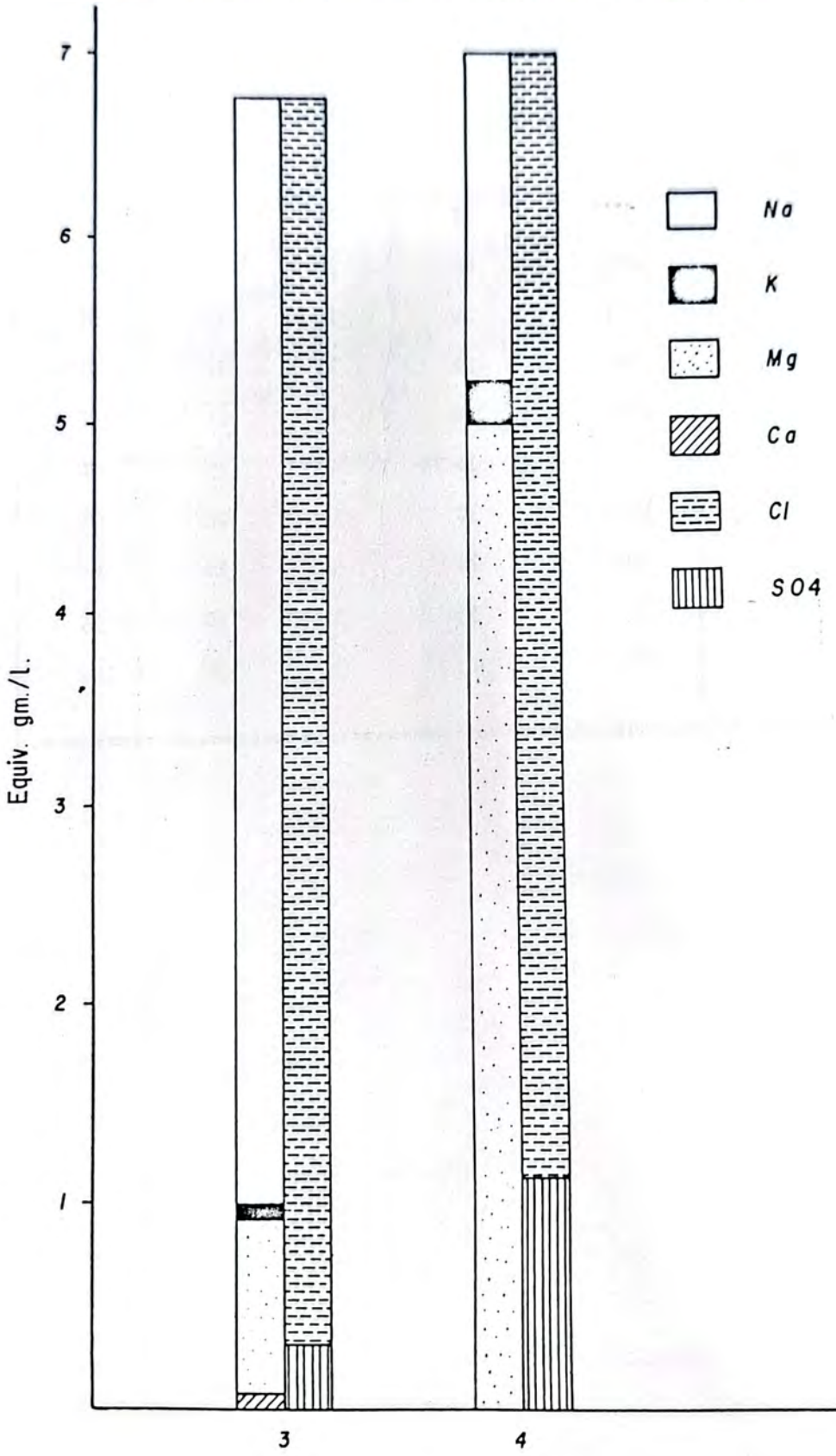

Table (6): Distribution of trace elements in gypsum and gypsum-bearing deposits (in ppm).

Sample No.	Sr	Ba	Li	B	Br
B-1	300	10	10	15	56
B-1"	300	12	10	15	60
I-4	5600	40	10	20	180
III-4	4100	10	10	15	80
II-3	2900	10	10	15	70
II-10	1600	30	10	20	50
III-3	7200	10	10	15	20
IV-3	1500	10	10	20	70
A-5	8900	20	10	20	60
I-3	1060	35	10	120	150
III	1800	40	10	120	140

Table (7): Distribution of trace elements in salts and brines (in ppm).

Sample No.	Sr.	Ba	Li	B	Fr
1	1250	20	30	40	150
2	1000	40	60	20	1100
3	150	-	10	30	60
4	120	10	10	50	250

These analysis were carried out at the Robertson International Limite England. The following elements were identified and discussed as follows:

Strontium

Strontium is known to be found in sea water. Rankama and Shama (1950) gave an average content of 13 ppm of strontium in sea water. The evaporite sediments are thus comparatively rich in strontium and the entrance of Sr into the minerals of marine salt sediments seems to be regulated by the calcium content of these minerals. It was found that Sr in the crystallization of these aqueous solutions replaces exclusively the calcium ions not the potasium. So strontium is found to be found with gypsu rather than halite rocks. Noll, (1934) found 0.003-0. 13% in gypsum rocks and 0.17-69% SrO in anhydrite, while Stewart (1963) gave an average of 48-180 ppm in halite rocks.

Tables (6 and 7) show the distribution of Sr in gypsum an salt pans in the studied area. Sr is mainly found in the gyps beds (300-8900 ppm) rather than salt and brine water (120-1250 ppm). This is mainly due to its tendency to replace "Ca" in $CaSO_4$ system. The higher content of Sr in salt samples is mainly due to the presence of $CaSO_4$ and other Ca-Salts which a admixed with halite in these ponds.

Barium

Accordirg to Rankama and Sahama (1950), barium has an average of 260 ppm in sea water. The barium transported to th sea becomes largely separated already during the formation of hydrolyzate sediments and only small part thereof remains in

sea water. Barium does not form independant minerals in evaporates because of its low content in sea water and in the concentrating brines. The argillaceous sediments are the richest in barium (460 ppm).

In the studied samples, barium ranges between 10 to 40 ppm in gypsum deposits and from 10 to 40 similar in salt samples. These values are similar to those recorded by Rankama and Sahama (1950) and Goldschmidt (1954). The higher values are due to the marly and argillaceous contaminations.

Lithium

According to Rankama and Sahama (1950) and Goldschmidt (1954) lithium has an average of 0.2 ppm in sea water. Some lithium should be expected, therefore, in evaporite sediments, e.g. in halite in which lithium replaces sodium in small quantities.

Goldschmidt (1954) pointed out that "little is known about the occurrence or lithium in marine evaporite sediments, it has been detected but no determinations appear to have been reported".

In recent publications of Stewart (1963) and Rosler and Lange (1965) no data are given for lithium content of salt deposits.

Stewart (1963) mentioned that lithium has been detected spectrographically in marine evaporates and is present in the associated clays and clastic materials.

The distribution of lithium in gypsum and in salt pans is shown in Tables (6 , 7). Higher values of lithium were observed in the clayey and the marly gypsum samples. The salt samples

contain from 10-40 ppm lithium which may occur either in liquid inclusions in halite (in the form of Li Cl) or replacing sodium in halite.

Boron

Boron is considerably concentrated in evaporite deposits, such as salt deposits of marine origin. Harder (1959) found that gypsum and anhydrite may contain up to 500 ppm boron, while halite may contain about 50 ppm boron. Boron is usually found as various borates which are chiefly deposited as calcium and magnesium borates, the latter are more common in marine evaporites and tend to form in the latter stages of evaporation of sea water.

It should be noted also that clays have a strong tendency to adsorb boron from marine waters and salt clays may contain up to 2000 ppm B (Harder, 1959).

Tables (6, 7) show the distribution of boron in the studied samples.

In the gypsum deposits (Table 7) boron ranges between 15-20 ppm. This can be attributed to the separation of calcium borate in them. The marly and the clayey beds show high ratios (120 ppm)

On the other hand salt and brine water samples (Table 8) show a concentration of 20-50 ppm boron, values which are in agreement with those reported by Harder (1959). The highest amount is observed in the brine water, sample No. 2 (Table 8) which has been collected after crystallization of salts. This is to be expected since borates separates mainly together with magnesium salts (after the crystallization of halite).

Table (8): X-ray powder data (from diffractometer recordings) of gypsum from different localities, in the area of study.

I-4		II-3		III-5		IV-I		V-5		Gypsum A.S.T.M. (6-0046)	
dA°	I/I°	DA°	I/I°	dA°	I/I°	dA°	I/I°	dA°	I/I°	dA°	I/I°
7.56	100	7.52	100	7.55	80	7.52	100	7.52	100	7.56	100
4.23	80	4.27	80	4.25	22	4.23	80	4.25	25	4.27	51
3.70	30	3.78	30	3.78	60	3.75	80	3.77	60	3.79	21
3.08	80	3.02	80	3.05	100	3.07	80	3.05	100	3.06	57
2.88	80	2.86	70	2.82	42	2.85	50	2.86	37	2.87	27
2.79	30	2.77	30	2.77	11	2.77	30	2.77	12	2.79	5
2.67	80	2.67	70	2.67	33	2.66	40	2.67	42	2.68	28
2.49	30	2.51	40	2.52	13	2.50	20	2.52	17	2.59	4
2.20	30	2.23	30	2.21	30	2.20	20	2.21	30	2.22	6
2.08	60	2.08	40	2.07	28	2.06	20	2.07	30	2.08	10
1.89	50	1.90	40	1.98	55	1.95	40	1.94	17	1.95	2
1.83	50	1.83	70	1.89	20	1.88	20	1.89	60	1.89	16
1.81	50	1.82	40	1.81	24	1.80	20	1.81	24	1.81	10
1.77	50	1.77	40	1.71	24	1.70	30	1.76	24	1.77	10
1.65	20	1.65	30	1.65	11	1.65	20	1.64	10	1.65	2
1.61	30	1.61	30	1.62	28	1.60	20	1.61	10	1.62	6
1.52	20			1.53	8	1.52	10	1.58	12	1.58	2
1.43	30			1.46	8	1.45	10	1.45	10	1.46	1
1.37	30			1.36	20			1.36	20	1.34	3

Bromine

Small amounts of bromine (ionic radius 1.96 A^0) replace chlorine (1.81 A^0) in all the chloride salts. Practically no bromine separates from the brines during the deposition of carbonates or sulphates of calcium. As soon as deposition of halite begins, bromine is partially extracted from the brine, but because of its larger ionic radius, it tends to become concentrated in the later products and the Br:Cl ratio gradually increases in the residual liquid. The bromine content is given in Table (6, 7): gypsum deposits have concentration of 50-150 ppm Br. The higher values are observed in the clayey and calcareous gypsum which may contain some halite inclusions. The highest values are recorded in salt samples (1100 ppm), this provides a further proof to the above-mentioned conception of increase of Br in the latter salts to be formed on evaporation.

Mineralogy of the evaporite deposits

Identification of the evaporite minerals has been made mainly by microscopic and X-ray diffraction analysis of crushed and separated grains. Refractive indices have been measured by the immersion method using immersion media composed of a mixture of clove oil and monobromophelein in certain ratios to yield the refractive index range 1.514 to 1.665. Specific gravity of the evaporite rocks was determined by means of the pycnometer method.

The following evaporite minerals, listed in a decreasing order of abundance in the collected samples have been identified and described :

1- Gypsum

Gypsum is usually colorless, although some shades of pale grey color are observed due to impurities of clay, marl and other minerals. According to crystallinity and granularity, three types of gypsum have been observed :

a) Well-developed euhedral crystals of "selenite" which are found as distinct crystals or broad plates.

b) Coherent aggregates with a parallel fibrous structure parallel to C-axis, this is "satinspar".

c) Most gypsum occurs as massive rock gypsum, which is fine-grained and is often darkened by impurities.

The specific gravity for pure gypsum was found to be in the range of 2.2 - 2.4 (e.g. samples III-4, V-1, V-5), while the value tend to be low due to the contaminations present, e.g. sample I-5 has Sp.Gr.= 2.180 (gypseous marl).

In the case of sample VI-7 the Sp.Gr.= 2.650, which is mainly due to anhydrite inclusions (Sp.Gr. of anhydrite = 2.7 - 2.9).

Refractive indices measured for gypsum are :

$n\alpha$ = 1.519 - 1.521

$n\beta$ = 1.523 - 1.526

$n\gamma$ = 1.529 - 1.531

The X-ray powder diffraction analysis carried out on gypsum deposits from different localities is shown in Table (8).

2- Halite :

Halite occurs in considerable amounts in the marshy deposits

in the form of snow-white, very coarse-crystalline aggregates of well-developed hopper structure. It shows colorless clear crystals under the microscope, but frequently tiny inclusions filled with brine. Halite occurs commonly as aggregates of euhedral to subhedral cubes and the faces are often cavernous and stepped.

The specific gravity for pure crystalline halite is 2.12$_0$, while for impure salts are 2.082. Refractive index measured is 1.544. The data of X-ray powder diffraction analysis carried out on salt crystals are given in Table (9), which shows the presence of halite with minor amounts of sylvite.

3- Dolomite :

Dolomite forms up to about 20% of the calcareous gypsum beds associating with calcite. Dolomite and calcite, which ar chemically formed, occur as cementing materials in this rock.

Dolomite is yellowish white, microcrystalline and has a specific gravity equal to 2.83. It is colorless to grey, with grain size less than 10 microns and so it is termed "dolomicrite" (Folk, 1959).

Refractive indices measured are :

NE or nB = 1.500 - 1.526

NO or nw = 1.680 - 1.716

Dolomite has also been identified by means of X-ray powd diffraction analysis (Table 10) with some gypsum.

4- Calcite :

Calcite grains are not very common. They are always asso

Table (9): X-ray powder data (from diffractometer recordings) of a salt sample, from the area of study.

Sample data		A.S.T.M. Data			
		Halite 6-0622		Sylvite 4-0587	
dA°	I/I°	dA°	I/I°	dA°	I/I°
3.15	40			3.15	100
2.82	100	2.82	100		
2.18	20			2.22	59
1.99	100	1.99	55		
1.81	40			1.82	23
1.62	50	1.63	15		
1.54	40			1.57	8
1.41	40	1.41	6	1.41	20
1.26	50	1.22	11	1.28	13
1.15	50	1.15	7		
1.12	40			1.11	2
1.04	50	1.09	1	1.05	6
0.96	20	0.95	1	0.95	3

Table (10): X-ray powder data (from diffractometer recordings) showing contamination of gypsum with dolomite.

Sample data II-14		A.S.T.M. Data			
		Dolomite 5-0622		Gypsum 6-0046	
dA°	I/I°	dA°	I/I°	dA°	I/I°
7.55	80			7.56	100
3.05	80			3.06	57
2.87	100	2.88	100	2.87	27
2.67	40	2.66	4.3		
2.58	20	2.53	3.6	2.59	4
2.45	10			2.45	4
2.21	36	2.19	12		
2.08	46	2.06	1.7		
1.99	23	2.00	7.2	1.99	4
1.90	66			1.90	16
1.87	36	1.84	1.8	1.88	10
1.81	30	1.80	13	1.80	4
1.78	33	1.78	13.5	1.78	10
1.62	36			1.62	6
1.60	16			1.60	1
1.58	16			1.58	2
1.44	16	1.44	1.8	1.44	2

ted with dolomite in the calcareous gypsum. It cannot be distinguished from dolomite microscopically owing to its fine-grained nature and similarity in optical characters. Table (11) shows X-ray diffraction data of calcite within gypsum.

5- Sylvite :

Sylvite was only identified by means of X-ray powder analysis (Table 9).

In some cases sylvite was identified microscopically by its isotropy and refractive (lower than halite).

Slawson (1929), quoted by Deer et. al. (1962), stated that halite and sylvite form a continuous series of mixed crystals when crystallizing together, producing a series of 10 or 12 double salts ranging in refractive index from 1.544 (pure halite) to 1.490 (pure sylvite).

6- Anhydrite :

Anhydrite occurs only as small shreds included in the coarse-grained gypsum crystals of the subsurface samples (sample No. A-7). The anhydrite inclusions are usually less than 5% and identified mainly by X-ray diffraction analysis (Table 12).

7- Complex salts :

These salts have been detected by X-ray diffraction analysis in the evaporite samples collected from the concentration and marshy deposits of these identified minerals. Kieserite ($MgSO_4 \cdot H_2O$) and bloedite ($MgSO_4 \cdot Na_2SO_4 \cdot 4H_2O$). Tables 13, 14 show X-ray powder data of these minerals.

Table (11): X-ray powder data (from diffractometer recordings) showing contamination of gypsum with calcite.

Sample data III-3		A.S.T.M. Data			
		calcite 5-0586		gypsum 6-0040	
DA°	I/I°	dA°	I/I°	dA°	I/I°
7.52	40			7.56	100
4.23	40			4.27	51
3.82	40	3.86	12	3.79	21
3.03	100	3.04	100	3.06	57
2.88	30	2.85	3	2.87	27
2.67	30			2.68	28
2.48	40	2.50	14	2.50	60
2.27	50	2.29	18		
2.09	50	2.09	18	2.08	10
1.90	80	1.91	17	1.90	10
1.87	80	1.88	17	1.88	10
1.61	30	1.62	4	1.62	6
1.59	40	1.60	8		
1.52	40	1.52	5	1.52	1
1.44	30	1.44	5	1.44	2
1.42	30	1.42	3	1.42	1

Table (12): X-ray powder data (from diffractometer recordings) showing anhydrite associated with gypsum.

Sample data No. A-7		A. S. T. M. Data			
		Gypsum 6-0046		Anhydrite 6-0220	
dA°	I/I°	dA°	I/I°	dA°	I/I°
7.56	100	7.56	100		
4.27	20	4.27	51		
3.87	10			3.87	6
3.79	3	3.79	21		
3.50	95			3.50	100
3.06	50	3.06	57		
2.85	10			2.84	33
2.67	10	2.68	28		
2.49	2	2.50	6	2.47	8
2.20	10			2.21	20
2.14	1	2.14	1		
2.07	2	2.08	10	2.09	9
1.99	2	1.99	4	1.99	6
1.95	2	1.95	2	1.94	4
1.89	1	1.88	10	1.87	15
1.86	1	1.80	4	1.85	4
1.84	2	1.84	1		

Table (13): X-ray powder data of Kieserite from salt marshy deposits.

Sample data		A.S.T.M. Data	
		Kieserite 1-0638	
dA°	I/I°	dA°	I/I°
4.83	10	4.82	40
3.38	10	3.38	100
2.55	2	2.25	40

Table (14): X-ray powder data of bloedite from salt marshy deposits.

Sample data		A. S. T. M. Data	
		Bloedite 4-0549	
dA°	I/I°	dA°	I/I°
4.52	10	4.53	80
2.94	15	2.95	30
2.63	3	2.63	40
2.56	3	2.57	30
2.25	2	2.25	30
2.04	3	2.03	30
1.92	3	1.92	30
1.66	2	1.66	30

C O N C L U S I O N S

The Pleistocene, Holocene and subsurface Miocene evaporite deposits were studied geochemically and mineralogically to get information about their environment of deposition.

The chemical and modal analyses of gypsum deposits show that they consist of up to 98% $CaSO_4 \cdot 2H_2O$ in El-Barqan area. Other low percentages in the other localities, (6,86% - 97%) are due to contaminations of calcareous and marly materials. The main carbonate mineral present with sulfates is dolomite (1.02% - 7.00%), with traces of calcite. Anhydrite is shown only in the subsurface samples (due to dehydration at depth), its percentage is about 2%.

Calcined gypsum (not found in nature) appears in percentages in the chemical analysis and may be due to heating of gypsum.

The chemical analysis of saline samples (marshy deposits) shows that the main salt separated from the ponds is NaCl and minor amounts of K, Mg salts. Minor and trace amounts of gypsum may be also percipitated with halite. The chemical analysis of concentrated brine water reveals the presence of salt assemblage of: (Na, K) Cl, $MgCl_2$, $MgSO_4$, $CaSO_4$ while the discharged brine water consists of : (Na, K) Cl - $MgCl_2$ and $MgSO_4$.

The study of the distribution of trace elements in the evaporite deposits revealed the presence of Sr, Ba, Li, B and Br.

The manner of occurrence of these trace elements is discussed. The mineralogical composition of evaporite deposits (gypsum and salts) is investigated using x-ray powder diffraction techniques and optical microscopy. Gypsum is the common mineral encountered. Other minor minerals include anhydrite, dolomite, calcite and detrital minerals

El Shamy, I.Z., 1968, The geology of water and soil resources in El-Dabaa area, Western Mediterranean Coastal Zone, U.A.R. : M.Sc. Thesis, Cairo Univ.

El Shazly, M.M., 1964, Geology, Pedology and Hydrogeology of Mersa Matruh area: Ph.D. Thesis, Cairo Univ.

Folk, P.L., 1959, Principal petrographic classifications of limeston Bull. Amer. Ass. Pet., Vol. 43, pp.1.

Fourtau, R., 1893, La region de Mariout, Etude geologiques: Bull. Inst. Egypt. 111, 141.

Goldschmidt, V.M., 1954, Geochemistry: Oxford, Clorendon Press.

Hammad, F.A., 1966, The geology of ground water supplies in Ras el Hekma area, Western Mediterranean Littoral Zone, U.A.R.: M.Sc. Thesis, Cairo University.

---------- 1972, The geology of soils and water resources in the area between Ras El-Hekma and Ras Alam El Rum, Western Mediterranean Littoral Zone, Egypt: Ph.D. Thesis, Cairo University.

Harder, H., 1959, Beitrage Zur Geochemie des Bars. pt. 2-Bor in sedimenten: Akad. Wiss. Gottingen Nachr., 2, Mat. Phys. Kl. 6, 123.

Harga, A.A., 1967, Morphological and physical studies of Burg El-Arab - El-Hammam area: M.Sc. Thesis, Cairo Universi

Hilmy, M.E., 1951, Beach sands of the Mediterranean Coast of Egypt Jour. Sed. Pet., Vol. 21, p. 109.

Hume, W.F. and Hughes, F., 1921, The soils and water supplies of Maryut district west of Alexandria: Surv. Dept. Publ Vol. 37, Cairo.

Hume, W.F. and Little, O.H., 1928, Raised beaches and terraces of Egypt: Union Geogr. Int., Paris. Report Comm., pliocene and pleistocene terraces : 9.

Khalil, A.A., 1966, Constitution and suitability of local gypsum raw materials: M.Sc. Thesis, Nat. Res. Cen. Egypt.

Kolthoff, I.M. and Sandell, E.B., 1936, Textbook of quantitative inorganic analysis: McMillan Co., New York.

Noll, W., 1934, Geochemie des Strontium: Chemie der Erde, Vol. 8, pp. 507.

Paver, G.L., and Pretorius, D.A., 1954, Report on reconnaissance hydrogeologist investigations in the western desert coastal zone: Publ. Inst. Des., 5, 2.

Phillip, G., 1955, Geology of the pleistocenesediments of the Mediterranean Coast West of Abu Qir: Ph.D. Thesis, Cairo University.

Picard, L., 1943, Structures and Evolution of Palestine: Geol. Dept., Hebrew University, Jerusalem.

Rankama, K. and Sahama, Th., G., 1950, Geochemistry: Chicago Univ. Press.

Roser, H.J. and Longe, H., 1963, Geochische Tabellen: VEB Deutsch Verlag Grudstoff Industrie, Leipzig.

Said, R. and Kamel, T., 1957. The Distribution of Foraminifera in the Egyptian Mediterranean Coast: Egypt. Jour. Geol., Vol. 1, No.2.

Sandford, K.S. and Arkell, W.J., 1939, Paleolithic man and the Nile Valley in Lower Egypt: Univ. Chicago, Oriental Inst. Publ., 17.

Schewgler, E., 1948, Vorgange subaerischer diagenese in Kustend Unensanden des Agyptischen Mittelmeer gebiets: Neues Jabrobuch Montashefte, Abt., B, h-1-4, pp.g.

Shata, A.A., 1953, New light on the structural developments of the Western Desert of Egypt: Bull. Inst. Des. Egypt. Tome III, No.1.

---------- 1955, An introductory note on the geology of the northern portion of the Western Desert of Egypt: Bull. Inst. Des. Egyp., Tome 5, No.3, pp. 96-106.

---------- 1955, Remarks on the Physiography of El Amerya-Maryat area: Bull. Soc. Geogr. Egypt., Vol. 30, pp. 5-74.

---------- 1959, Rock exposures and their bearing on the soil formation of some desert areas of Egypt: Bull. Des. Egypt. No. 12, pp. 71-81.

---------- 1961, The geology of the ground water supplies in some arable lands in the desert of Egypt: Internal Rep., Des. Inst., Cairo.

---------- 1962, The Maryut agricultural project, the Mediterranean region littoral, Report geomorphogenic aspects: Internal Report, Des. Inst., G.D.D.O., Cairo.

---------- 1970, The geomorphology, Pedology and Hydrogeology of the Mediterranean Coast Desert of U.A.R. : Symposium on the Geology of Libya, Fac. Sci., Libya Univ., pp. 431 - 446.

Shotton, F.M., 1946, Water supplies in the Middle East compaigns, the main water table of the Miocene limestone of the coastal desert, Egypt: Report from water and water engineering, Cairo.

Shukri, N.M., Phillip, G., 1955, The Geology of the Mediterranean Coast between Rosetta and Bardia: Part I, Recent Sediments: Bull. Inst. Egypt, 37(2), pp.377.

---------- 1956, The Geology of the Mediterranean Coast between Rosetta and Bardia: Part III, Pleistocene sediments, Mineral analysis: Bull. Inst. Egypt, 37(2), pp. 445.

Stewart, F.H., 1963, Marine evaporites: Geol. Surv. USA, Prof. Paper, pp. 440.

Welcher, F.J., 1958, The analytical uses of ethylenediamine tetraacitic acid: Princeton, Van Nostrand.

* * * * * * * *

الخلاصـــــــــــة

يتناول هذا البحث دراسة مفصلة لرواسب المتبخرات التي توجـــد على طـــول الساحل الشمالي لجمهورية مصـــر العربيـــة. ويختص هـــــذا الجـــزء من هذه الدراسة بجيولوجيـــة وجيوكيميائيـــة والمعادن المكونـــة لهذه الرواسب. وقـــد تبين ان رواسب المتبخرات في هذه المنطقـــــة تتبـــع عصر البليستوسين والعصر الحديث. وجـــد ان معدن الجبـــس يكون المعدن الرئيس لرواسب عصـــر البليستوسين بالاضافة الى بعـــــض الشوائب من معادن الدولوميت والكالســـيت والهاليت والانهيدريـــــت اما رواسب المتبخـــرات التابعة للعصـــر الحديث فتتكون من معدن الهاليت بالاضافة الى بعـــض امـــلاح البوتاسيوم والماغنسيوم مع اثـــار من الجبـــس. وقـــد تم ايضـــا دراسة توزيع بعض العناصـــر الشحيحـــة في هـــــــذه الرواســـب.

STUDIES ON THE EVAPORITE OCCURRENCES ALONG COASTAL PLAIN, WEST OF ALEXANDRIA, A.R.E.*

Part - II

Petrography and Petrogensis

M.E. HILMY, S.A. HUSSEIN and S. HASSAN

Faculty of Science, Ain Shams,

University, Cairo, EGYPT.

INTRODUCTION

In part-I of this work (Hilmy et al., 1978) the geological occurrence, geochemistry and minerology of the evaporite deposits encountered along the Mediterranean Coastal Plain, west of Alexandria town, were discussed.

The present work deals with the petrography of the different rock types of these deposits. The gensis of the evaporite deposits in the Coastal Zone is then discussed in the light of the data and informations get from part-I (Hilmy et al., 1978) and part-II.

Evaporite Rocks require special technique for preparing thin sections in them due to their physical properties as solubility in water, low hardness and loss of water content at high temperature etc. In the preparation of thin sections the procedure described by Reed and Mergner (1953) has been followed with some modifications proposed by the authors.

---

* This study represents a part of M.Sc. Thesis presented by the third author, under the supervision of the first and second authors. It was submitted to the Faculty of Science, Ain Shams University, Cairo, EGYPT, in 1977.

Al-Mustansiriyah Journal of Science, Vol. 2 (1977).

Petrography of the evaporite deposits

According to the geologic occurrence of the evaporite deposits, previously mentioned in part-I (Hilmy et.al, 1978), these deposits can be classified as follows :

I- Gypsum and gypsum-bearing rocks.

II- Salts of marshy deposits.

III- Evaporite-associated rocks.

The following is a brief description of the macroscopic and microscopic characters of these deposits.

I- Gypsum and gypsum-bearing rocks

Gypsum occurs in the form of a milky white deposit which is commonly laminated (Plate 1-a). Generally, the gypsum at the faces of the quarries is compact and massive, sometimes shows knotty structure. Interbedded with gypsum are yellowish white lenticular bands and patches of calcareous materials (Plate 1-a).

It varies between hard deposit (e.g., El-Barqan) to friable and cavernous deposits (e.g., El-Hammam). Some micro-structures are observed within gypsum lamination (e.g., microfolding or microtilting), (Plate 1-b).

The laminated rock gypsum can be subdivided on the basis of grain size, macroscopic and microscopic features into three main varieties :-

1- Very coarse swallow-tail crystalline rock gypsum

It is commonly observed in El-Barqan, El-Imayid and, Abu-Sir subsurface deposits. The rock show coarse aggregates of large swallow-tail selenite twins (arrow-head crystals), reaching about 10 to 15 cm in length and 1 to 4 cm in

Plate -1-

a) View at the face of El-Hammam gypsum deposit, showing lenticular bands and patches of calcarecus materials within gypsum laminations (looking west direction).

b) View at the face of El-Imayid gypsum deposit, showing microtilting within gypsum laminae, (looking west direction).

thickness (Plate 2-a). The aggregates show a peculiar fabric with the composition plane (100) of the twins perpendicular or subperpendicular to the bedding planes. Sometimes these arrow-head crystals show radial growth from common centers. Some beds of the selenitic gypsum show a cavernous habit rich in voids which are filled with carbonate, marshy and sandy materials.

In thin section the selenite is colorless in plane polarized light, except where it is contaminated with fine-grained inclusions, which give it a turbid color. The crystals show an equidimensional, polygonal, rhombic, prismatic, tabular or rod-like habits. Some of them show no regular shape, but most of them display very clear outlines due to cleavage planes. The close-packing of these crystals builds an interlocking texture of a mosaic form. There are sometimes a tendency, for the crystals to be oriented more or less parallel with their great axis, or the apex of arrow-head twinning (plate 2-b) perpendicular to bedding and are separated by very thin layers of accessory minerals such as dolomite and very fine-grained clay particles.

The coarse selenitic gypsum in notably pure, but it has several inclusions, important among which are marl, sand, clay and carbonate minerals. These impurities are either concentrated as intercalations, patches, stringers, thin lamellae or scattered as aggregates of grains.

This type of gypsum appears to be supported by crystallographic studies of Oginiben (1955, 1957), and is called "rhythmic primary gypsum".

Plate -2-

(a) Coarse-grained gypsum, showing long clear swallow-tail twinning perpendicular or subperpendicular to bedding plane, X 0.85. (El-Imayid area)

(b) Photomicrograph showing coarse-grained selenite with arrow-head twinning, crossed Nicols X 26.

2- Coarse-grained gypsum

The rock is white in color, transparent to translucent, hard and porous. It shows lamination, the laminae vary from 3 to 5 mm in thickness and slightly undulated (plate 3-a).

The laminae are of two types: (a) white microcrystalline gypsum, and (b) colorless or white coarse-grained gypsum laminae characterized by the occurrence of rows of phanerocrystalline gypsum crystals (1 cm or more in diameter) between the dense microcrystalline gypsum. These laminae are generally separated by clayey carbonate streaks.

Under the microscope the coarse-grained gypsum shows an increase in crystal-size from top to base of the laminae, i.e. inverse-graded bedding. It ranges from microcrystalline at the top, to coarse-crystalline at the base. An investigation of the shape of the grains shows that they are nearly equidimensional and irregular polygonal individuals predominate.

With them are associated other forms of elongated rhomboidal sections of prismatic grains, and less commonly lamellar, platy, rounded and fibrous crystals (plate 3-b).

The coarse gypsum crystals show porphyritic-type texture where the coarse grains are embedded in microcrystalline or cryptocrystalline gypsum matrix (plate 4-a).

The coarse-grained gypsum contains more impurities than the coarse selenitic type (more than 15%). These impurities are found as intercalations, patches, aggregates or oriented parallel to cleavage planes of gypsum (plate 4-b). The most important of these impurities are the carbonate minerals

Plate -3-

(a) Cavernous gypsum showing rhythmic laminae of gypsum intercalated with thin bands of marly and calcareous materials, X 0.85.

b) Photomicrograph of Coarse-grained gypsum showing different habits (e.g. rhombic, rounded, spindle...ect), crossed Nicols X 26.

Plate -4

(a) Photomicrograph of porphyritic-type texture in gypsum rock, notice the coarse-grained nature of gypsum crystals embedded in microcrystalline gypsum matrix, Crossed Nicols X26.

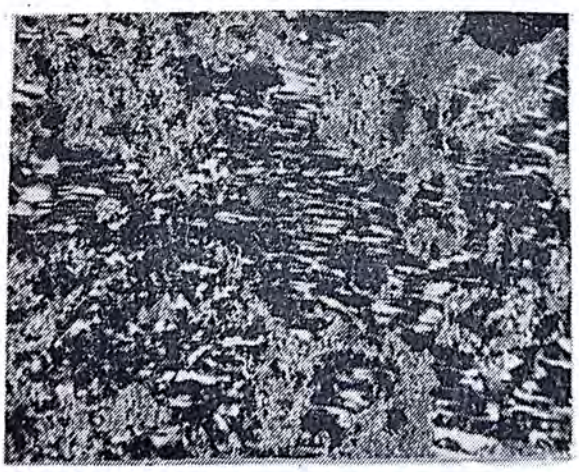

(b) Photomicrograph Of coarse -grained gypsum showing very fine-grained carbonate minerals (calcite, dolomicrite) as contaminations oriented parallel to cleavage planes of gypsum, Crosed Nicols X 26.

(calcite and/or dolomite), which occur as very fine rounded grains, (plate 4-b).

The clayey impurities are found in the form of small yellowish brown, fine-grained aggregates with few disseminated very fine quartz, glauconite, calcareous rock fragments and opaque materials.

In the subsurface occurence of gypsum at Abu-Sir ridge, the coarse-crystalline gypsum shows several inclusions, the most important are thin shreds or lamellae of anhydrite with sharp and mostly corroded borders. The anhydrite lamellae are small with a maximum length of about 0.5 mm and very often are parallel to the gypsum cleavage planes or located within them (plate 5-a).

3- Fine-grained gypsum

It is greyish-white in color, slightly friable and porous. It has a saccharoidal shape and sometimes alternating with marl, calcareous or clayey matter. It shows a clear lamination of brownish fine-grained marly, calcareous laminae and colorless gypsum laminae. The gypsum varies between micro-crystalline to cryptocrystalline, with gradual increase in size from top to base, (inverse graded-bedding).

The most important feature of the fine-grained gypsum is the cavernous habit. The cavities are either empty or filled with very fine-grained carbonates, clay particles, few disseminated opaques, black carbonaceous materials and quartz grains (plate 5-b).

Plate - 5

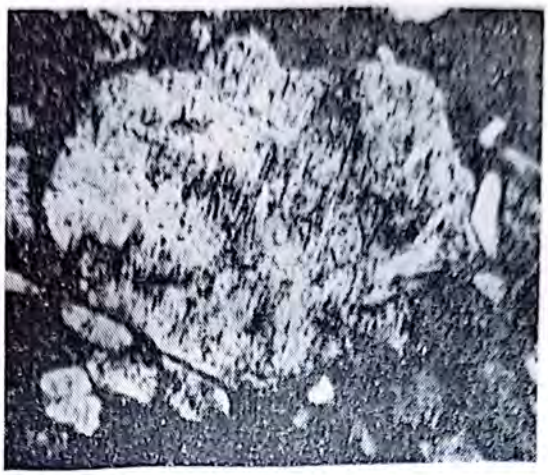

(a) Photomicrograph of coarse-grained gypsum showing thin shreds or lamellae of anhydrite within it. Notice that the anhydrite is oriented parallel to gypsum cleavage, Crossed Nicols X 105.

(b) Photomicrograph of microcrystalline cavernous gypsum with more cavities filled with very fine-grained carbonate minerals (Calcite and/or dolomicrite), Crossed Nicols X 26.

II- Salt of marshy deposits

Marshy deposits are observed in several pans within the depressions between the ridges (plate 6-a). These deposits are formed of slightly compact saline calcareous mud. They become compact, crystalline and more saline with increasing depth of the pan (plate 6-b). In general these salt deposits consist mainly of halite. The halite layer is white milky in color, fine-grained and often admixed with loamy soil. The salt pans are covered by about 5 cm of concentrated, sticky, colorless brine water.

The bottom of the pan is covered with a thin layer of about 0.5 cm of colorless coarse-crystalline halite, compact, hard and shows well-developed hopper structure (plate 7-a). At the borders of the pan the salts become finer and non-crystalline.

Microscopic indetification of crushed grains immersed in oil, and also from thin section microscopy, revealed that the rock is composed mainly of euhedral halite cubes with perfect cubical cleavage. The halite is colorless clear, in plane polarized light, but frequently show tiny inclusions filled with brine that appear cloudy. Between crossed Nicols, the halite crystals contain less than 5% silty inclusions formed of very fine-grained clayey materials which have been blown by the wind into the pan from the surrounding deposits (plate 7-b). A mixed crystalline aggregate of halite and sylvite with chevron structure is commonly observed in the sections showing growth of the halite-sylvite deposits.

III- Evaporite associated rocks

The evaporite associated rocks are found as intercalations or banding within gypsum beds. They also occur as cavity fillings

Plate - 6

(a) Distant view of marshy deposites, showing their occurence within the depression, notice also the accumulation of sal

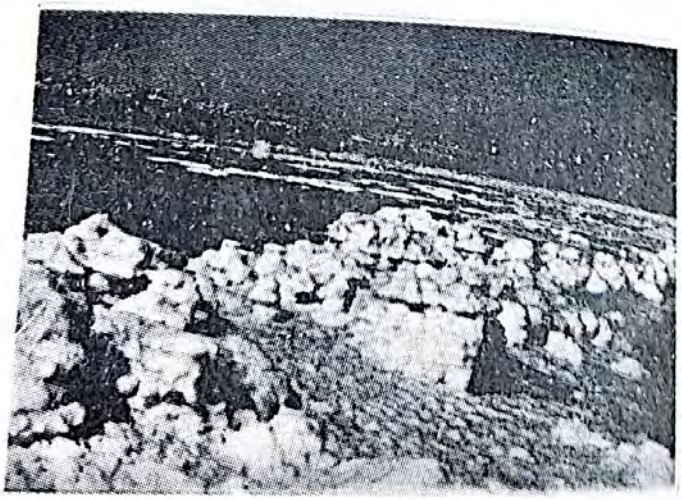

(b) Close-up view of salt accumulations at the centre of salt p notice the coarse-crystalline habit of salts .

Plate -7-

(a) Coarse-grained halite crystals, showing the perfect cubical cleavage and pyramidal-shaphed hopper crystal. X 0. 85 (Burg El-Arab Marshy deposits).

(b) Photomicrograph of coarse-crystalline halites (black) contaminated with very fine-grained clayey materials, Crossed Nicols X 26.

in gypsum bed at El-Barqan. These rocks consist of different varieties of the following rocks:

1- Limestone beds

Three types of limestones are observed within evaporite succession.

a. Oolitic limestone

It is found at the base of El-Imayid and El-Hammam sections.

It is snow white in color, but on weathering becomes grey and brown. Microscopically, the oolitic limestone is composed essentially of calcareous oolitic sand-size grains which are cemented together by fine calcium carbonate. It exhibits different shapes varying from rounded, spherical, ellipsoidal and irregular, (plate 8-a). The grains show a concentric structure where the carbonate layers are arranged around a nucleous. The shape of the oolitic grain reflects the shape of the nuclei which are either composed of quartz grains, carbonate grains, shell fragments or foraminifera. The diameter of the grains varies between 1 mm and 0.125 mm. The matrix is composed of calcareous material having a microcrystalline or cryptocrystalline texture.

b. Sandy limestones

It is observed in samples III-6 (at Imayid), (plate 8-b). The sandy limestone is composed of rounded carbonate grains of fine to very fine-grained. It is fossiliferous containing some foraminifera and shell fragments. These fragments are

Plate - 8

(a) Photomicrograph of colitic limestone, Crossed Nicols X 26.

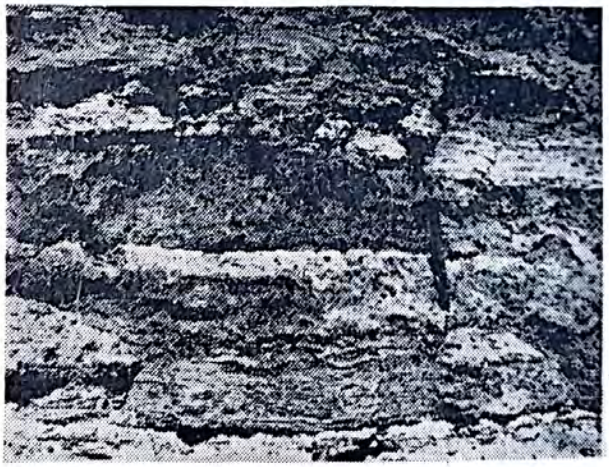

(b) Close-up view showing limestone bed within the gypsum succ-
ession of El-Hammam quarry.

rounded reflecting the reworking and transportation of them. The matrix is composed of very fine-grained clayey materials. Few fine-grained and rounded grains are observed scattered within clay matrix. Also minute particles of opaque minerals (iron oxides) and heavy mineral grains are identified.

c. Recrystallized limestone

This bed of limestone is found as a cap-rock to evaporite succession at El-Barqan gypsum occurrence. It is yellowish-brown, compact and hard, whereby it forms a resistant cover to weathering at that area. Microscopically, it consists of calcareous rock fragments. These fragments are composed essentially of foraminiferal limestones and/or recrystallized limestones. All these fragments are rounded in shape, giving a criteria of their reworking character (Allochthonous). The matrix is composed of clayey materials. These clayey materials are yellowish and very fine-grained. Quartz grains are found as fine to medium-grained, rounded to subrounded, and embedded within clay matrix or the calcareous grains. Opaque minerals (iron oxides) are observed as minute and scattered spots within the whole mass of the rock.

2- Marl beds

The marl beds are of common occurrence within evaporite successions, especially at El-Hammam gypsum quarries (samples, I-3, II-4, II-11, and II-7). They are found as intercalation or thin bands between evaporite deposits. According to their

mineral composition, there are two varieties of marl beds, namely:

a. Gypseous marl (e.g. samples I-5, II-15, II-14 El-Hammam area, plate 9-a). It shows white to brown color, friable to semi-hard, with scattered euhedral crystals of gypsum (plate 9-b).

In the field it occurs as thin streaks up to 30 cm in thickness.

Under the microscope the gypseous marl is essentially composed of carbonate minerals(45%) and argillaceous minerals (50%). The carbonates are found as very fine-grains (calcite and/or dolomite), rounded to subrounded and with clear twinkling. The argillaceous materials occur as very fine-grained materials, opaque to transparent, fossiliferous, with numerous cavities and form the groundmass of the rock. Few euhedra of gypsum crystals are seen scattered within the groundmass or as cavity-fillings of the interspaces present (about 5%). Embedded in the groundmass, other than the gypsum crystals, are few rounded grains of quartz and glauconite aggregates.

b. Sandy marls (e.g. samples II-7 and II-11, El-Hammam area). The rock is mainly white in color and friable. In thin section, the sandy marl consists essentially of carbonate minerals (45%) and argillaceous materials (50%). The carbonates are colorless, very fine-grained, rounded,fossiliferous showing few foraminiferal shell fragments and either found admixed with clay minerals or filling the cavities present. The clay materials occur as very fine-grained particles or as aggregates and usually transparent or transluscent. Embedded in this matrix ,

Plate -9-

(a) Close-up view of gypsum beds showing some marly intercalations (El-Hammam area) .

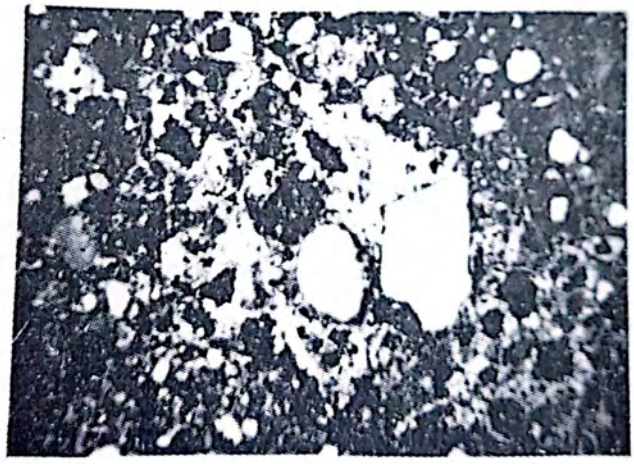

(b) Photomicrograph of gypsum marl, notice the euhedral gypsum crystals scattered within the groundmass, Crossed Nicols X 26.

there are numerous quartz grains (up to 5%). Quartz is found as fine to very fine-grained, rounded to subrounded grains. Rounded grains or some patches of glauconite aggregates are also observed within the marly groundmass. Few gypsum needles are observed filling some cavities.

3- Clay beds

These beds are found at El-Hamman succession (sample No.II-1) and El-Gharbaniat quarry (sample No. IV-3). The clays are found as thin streaks and intercalations between gypsum beds. There are two varieties of clays depending on mineralogic composition:

a. Sandy gypseous clay e.g. sample No. II-1 and some fissure fillings in Barqan (C-3), where the rock is composed of clay minerals (over 90%) with some accessory carbonates, quartz, gypsum and glauconite. The clay minerals are found as very fine-grained particles with grey to opaque color and having several void spaces. The carbonates are present as colorless, rounded, very fine-grained material either mixed with clayey materials or filling cavities. Quartz grains are embedded within the groundmass as colorless, fine to very fine-grained, rounded to subrounded grains. Gypsum is found as coarse-crystalline, euhedral and twinned crystals which may be filling the cavities or scattered as pseudophenocrysts within carbonate and clayey materials.

b. Clay e.g. sample No. IV-3, where the rock is totally composed of argillaceous materials. These are transparent and translucent, very fine aggregate, fossiliferous and rich in cavities. The majority of these voids and cavities are

empty, some of them are filled with very fine-grained carbonate minerals (calcite, dolomite), rounded quartz or acicular gypsum crystals.

4- Calcareous loam

The calcareous loam has been met with above gypsum beds and as large sheets in bore holes dug in it for gypsum extraction. The deposit attains a thickness of more 50 cm. It is greyish white in color and friable. Mineralogically it consists of about 50% of clay and silt, about 30% of fine cement of calcite and dolomite, about 15% of well-rounded quartz sand grains with average particle size in the medium to fine sand grade, about 5% of rounded fine gypsum grains, some carbonaceous impregnations and few grains of heavy minerals (opaques, zircon, monazite, rutile, garnet, staurolite and glauconite). Most of the grains are well-rounded and exhibited well-sorting character. The cementing material is composed of silt, clay, carbonates and black carbonaceous matter. Gypsum occurs in the form of: (a) Coarse, well-rounded colorless flakes that vary in size from less than 1 mm to 4 mm , (b) rosettes of about 3-4 mm, and (c) aggregates of about 2-6 mm long of fine rounded grains. Some broken fragments of common fossils are well preserved.

5- Gypsarenite

It is found as cavity fillings to El-Barqan gypsum (sample C-2). The rock is yellowish white in color and friable. The clastic texture may be seen macroscopically by difference in color between the grains. The gypsum is found in a percentage up to 30%. It occurs as colorless to cloudy, rounded grains and having grain size ranging from coarse to medium grade. Fragments of gypsum are largely

predominant, and possess different types of twinning (e.g. Swallow-tail, lamellar and simple). Some of these fragments are elongated parallel to the twinning plane. Some fibrous and acicular grains of gypsum are also observed. The other detrital components beside gypsum, are often reworked quartz, rock fragments and carbonate minerals.

6- Gypsum-quartz sand

This deposit is observed as small-scale sand dunes over gypsum occurrences in El-Barqan area. Also it is observed along the sides of the different hills at this locality. It is characterized by the presence of more or less equal quantities of gypsum and quartz grains that can be easily detected by a pocket lens. It has a lighter color (due to gypsum grains), yellowish white, loose and composed of about 60% of quartz and feldspars, about 35% of gypsum and some heavy minerals (opaques, zircon, monazite,rutile, garnet, staurolite and glauconite). The average particle size of gypsum-quartz sand is medium to fine grade, with excellent sorting and well-rounded grains. Spherecity is high in quartz grains and low in gypsum grains, as these latter are rod-like and thin flakes in shape. Pitting is prominent feature in gypsum grains. Some broken fragments of calcareous forms are also observed.

ORIGIN OF EVAPORITES IN THE COASTAL AREA

In discussing this problem, the startigraphic position of the evaporite deposits, must be taken into consideration. The evaporite deposits in the area under investigation, are met with in the Miocene subsurface section (Abu-Sir), Pleistocene surface sections

(El-Gharbaniat, El-Hammam, El-Imayid and El-Barqan), and Recent salt of marshy deposits.

Based on the foregoing field, geochemical, mineralogical (part-I) and petrographic observations, the origin of the evaporite deposits is discussed.

1- Miocene evaporites

The gypsum beds encountered in the Abu-sir subsurface section are considered to be of Miocene age (Hammad, 1972). Two beds are detected, an upper and lower one having a 50 m and 30 m thickness respectively and are separated by a thick chalky limestone bed (part-I). Again the upper gypsum bed is overlain by a chalky limestone bed (40 m), while the lower one is underlain by clay beds. The whole succession indicates two stages of evaporation within the Miocene section.

There is no doubt about the marine origin of these evaporite deposits, as indicated from the mineral association present. The gypsum was deposited by evaporation from ancient lagoons. These lagoons were formed during the marine transgression of Middle Miocene, and on its subsequent regression the lagoons were so formed. It must be noted that these lagoon series are known in different parts of Egypt, e.g. Gulf of Suez and Sinai, and attributed to the invassion of Middle Miocene sea (Hume et.al. 1928).

The general sequence of deposition in a normal basin is calcium carbonate, then calcium sulphate and finally sodium chloride and other soluble salts (Degens, 1965). The deposition of gypsum beds has taken place in lagoons that were continuously opened and attached to the sea, i.e. the lagoons did not reach the stage of deposition of

the most soluble salts (NaCl, KCl and $MgSO_4$). At the same time the lagoons are supposed to have been affected by gradual subsidence to permit a continuous running and inflow of sea water into the lagoons, causing the deposition of great thicknesses of gypsum.

In the present work, the geochemical and mineralogical studies revealed that the Miocene evaporites at Abu-Sir subsurface section consist mainly of coarse-grained gypsum, in addition to minor amounts of anhydrite which appear as thin shreds and inclusions within the gypsum crystals. The anhydrite is attributed to the dehydration of gypsum through pressure effect, due to depth, i.e. secondary. Summarizing the paragenetic sequence in the Miocene evaporites, the authors conclude that there are two cycles of evaporation within the Miocene section in the studied area.

These cycles led to the deposition of two thick beds of gypsum. The two cycles are separated by marine transgression giving rise a thick chalky limestone bed. In each cycle of evaporation the only salt precipitated was gypsum. Geomorphologic and tectonic factors affected in the processes that resulted in the deposition of a thick column of gypsum. Finally, due to compaction and burial, some gypsum dehydrated giving rise to minor amounts of anhydrite.

II- Pleistocene evaporites

The surface evaporite occurrences in the studied area, are considered to be of Pleistocene age (Abdullah, 1966). These deposits consist mainly of bedded gypsum and calcareous gypsum separated by marine limestones, marls and clays indicating arid and wet climatic flactuations. The mineral association as indicated from mineralogical studies and geochemical analyses indicates a marine origin of these evaporite deposits.

From the evidences gathered in the field, it is quite clear that most of the gypsum deposits in the coastal area, occur in the longitudinal depression between the second and the third ridges (Abu-sir and Maryut ridges). El-Barqan gypsum occurrence lies in the depression behind the forth ridge. These ridges and depressions are parallel to the coast of the Mediterranean Sea. From the distribution of evaporites, it is clearly observed that the deposition of evaporites is of a regional rather than strictly local characteristic. This indicates that the gypsum was deposited by evaporation from ancient lagoons. These lagoons were formed during the marine transgression of the Middle Pleistocene, where the Mediterranean Sea invaded the coastal area behind the first and the second ridges, and on its consequent regression the lagoons so formed in the depressions. The ridges acted as a bars, separating the shore lines from the lagoons. Shukri et al. (1956) identified nine main bars separated by seven lagoons. From the ages of these bars and lagoons, the same authors were able to cofigurate the shore lines of the Mediterranean Sea in the Pleistocene times (part - I Hilmy et al., 1978).

As mentioned before, for the Miocene subsurface evaporites, the lagoons were not completely disconnected from the sea, whereby evaporation continued in depositing calcium sulphate rather than other soluble salts. The fact that gypsum deposits show rhythmic bedding (e.g. El-Hammam, El-Gharbaniat and El-Imayid) is an indication of the seasonal flactuations of water level. The rising water seasons cause not only less precipitation of salts but also selective solving of the easily soluble minerals. This gives rise to vast volumes of sulphate deposits as compared to chlorides. In other

words during the rising water season dilution of the lagoon occurs, and the deposited chlorides are dissolved to a great extent and return back to the Mediterranean coast.

Gypsum occurs in a number of flat sheets or laminated strata separated by marly and limestone sheets.

Field observations revealed that the gypsum sheets are of limited thickness and show no preferential centers or axes of greater thickness. This is an evidence that no basinal subsidence took place during the deposition. On the other hand, one of the gypsum deposits is very broad and thicker. This is El-Barqan gypsum deposit, which covers a surface area of about 15 square Km, and the gypsum attains a thickness of more than 6 m. This large extension can be attributed to lower elevation at this area and also due to gradual subsidence at the time of deposition. The pertinent facts far reached throughout the present study, which have a bearing on the problem of whether gypsum was primary or secondary, are based on the following observations:

1. Chemical and modal analyses of these deposits show that they consist of up to 98% $CaSO_4 . 2H_2O$ (e.g. El-Barqan). The lower percentage is due to contaminations with calcareous and marly materials. The main calcareous impurities are dolomite (1-7%) with traces of calcite.

2. The mineralogical studies of gypsum rock samples collected from their occurrences, using both polarizing microscope and X-ray diffraction method, indicate also the presence of gypsum, dolomite and calcite.

3. The petrographic studies of the gypsum and gypsum-bearing rocks, show the presence of three varieties, namely: very coarse swallow-tail crystalline rock gypsum, coarse-grained gypsum and fine-grained gypsum. Gypsum occurs in different forms and habits, e.g. platy, fibrous, radiating, granular, rod-like, tabular, etc. The most common texture is the swallow-tail one.

The coarse-grained gypsum shows also phanero-crystalline crystals, 1 cm or more in diameter, between the dense micro-crystalline rhythmic laminae. These coarse crystals show prophyritic-type texture. Ogniben (1955) failed to explain the presence of these coarse gypsum crystals and failed also to explain the formation of the swallow-tail rock gypsum with crystals of about 10 cm or more in length, within the studied gypsum occurrence.

This prophyritic-type texture may be produced through the growth of the coarse crystals at the expense of smaller ones, in a process of partial dissolving and recrystallizations during deposition. This would be influenced through the dilution of the lagoons in winter times in such a way that the water can dissolve partially the gypsum grains, then the increase in salinity in the summer would precipitate sulphate in such a way that the smaller gypsum grains act as nuclei for the newly precipitate sulphates.

The three above mentioned rock varieties namely; fine-grained gypsum, coarse-grained gypsum and very coarse swallow-tail gypsum, represent three successive stages in such partial dissolving and recrystallization processes. It can be concluded

also that the gypsum is always primary.

With regard to the paragenetic sequence of evaporite deposits in the Pleistocene age, it can be said that it follows the experimental results found by Usiglio (1843). The first precipitating materials being the iron oxides (found within marly materials), calcite and dolomite. Dolomite is considered primary of evaporite origin due to its interbedding character with gypsum is considerable amounts (found with marly intercalation), lack of zoning, and its fine size (dolomicrite). Then the gypsum was precipitated in large amounts together with minor amounts of dolomite (found in cavities and intergranular cavities), producing gypsum beds. The recrystallization processes during deposition led to the development of an association of very coarse, coarse and fine-grained varieties of gypsum.

III- Recent salt of marshy deposits :

Field observations show that the salt deposits occur in a number of salt pans which are found in the basins and depressions located in the studied area. These pans depend mainly on rain water for dissolution of the residual salts (i.e. Lake Maryut) together with minor sea seepage. Rain falling on the higher parts of the area flows into the depression of these natural pans. The water accumulating is left to dissolve the residual salts and then to evaporate leaving behind a crust of salts. The following observations are arrived at regarding the marshy salt deposits:

1. Chemical analysis of salts, shows that the main salt

separated from these pans is NaCl and minor amounts of K, and Mg-salts. Minor and trace amounts of gypsum are also precipitated together with NaCl. The concentrated brine water consists of salt assemblage of (Na, K) Cl, $MgCl_2$, $MgSO_4$, $CaSO_4$ while the discharged brine water consists of (Na, K) Cl - $MgCl_2$ - $MgSO_4$.

2. Mineralogically, the marshy deposits consist of halite, calcite, gypsum as major minerals. Other minor minerals include sylvite, anhydrite, kisserite, bloedite and detrital minerals.

3. Petrographically, the salts consists of snow-white aggregates of coarse-crystalline salt with well-developed hopper structure. Crystals collected from the base of the pans are coarse-crystalline, while those collected from the borders become white saccharoidal, fine-grained aggregates, often mixed with windblown sand and fine earthy matter of calcareous loam and clays. Some halite cubes are colorless with R-I=1.541, a mixed crystalline aggregate of halite and sylvite.

From the results of the above-mentioned identifications and observations of the mineralogical associations of the marsh saline deposits, the authors give the following explanation of the paragenetic squence:

The principal ions encountered in these ponds are :

Na^+ , Ca^{2+} , Mg^{2+} , K^+ , Cl^- , SO_4^{2-} and CO_3^{2-}

On evaporation, the bulk of carbonate will normally separate as $CaCO_3$ before any other salts crystallize (Degens, 1969)

In such closed basins most of the calcium is precipitate as sulphate in the concentration ponds before halite starts to

separate. According to Borchert and Muir (1964), this process is accompanied by an increase in specific gravity and refractive index of the lagoons. In the salt pans when specific gravity reaches 1.21, halite will crystallize, because sodium and chlorine are so much in excess of other coponents. Salts of potassium and magnesium will form from a solution saturated with sodium chloride in the last stages of crystallization.

Summarizing, the authors arrive to the following paragenetic sequence of the evaporite minerals of the marshy deposits:

4. K, Mg - salts	(minor)	Late
3. Halite	(major)	
2. Gypsum	(minor)	
1. Calcium carbonate	(minor)	Early

REFERENCES

Abdullah, A.M., 1966, Geology of some gypsum deposits in North Western of Egypt: Geol. Surv. Egypt. 41, 11 pp.

_____, 1966, Stratigraphy and structure of a portion in the North Western Desert of Egypt, UAR (El-Alamein Dabaa - Qattara - Moghra area) with reference to its economic potentialities: Geol. Surv. Egypt. 45, 19 pp.

Borchert, H. and Muir, R.O., 1964, Salt deposits: Van Nostrand., New York.

Degens, R.T., 1965, Geochemistry of sediments: Prantice-Hall, New Gersey.

Hammad, F.A., 1972, The Geology of soils and water resources in the area between Ras El-Hekma and Ras Alam El Rum, Western Mediterranean litoral Zone, Egypt: Ph.D. Thesis, Cairo University.

Hilmy, M.E., Hussein, S.A. and Hassan, S., 1978, studies on the evaporite occurences along the coastal plain, west of Alexandria, ARE, Part 1: Geochemical and mineralogical studies, El-Mustansiriyah Journal of Science Baghdad, In Press.

Hume, W.F. and Little, O.H., 1928, Raised beaches and terraces of Egypt: Union Geogr. Int. Paris. Report Comm, 9.

Oginiben, L., 1955, Inverse graded bedding in primary gypsum of chemical deposition: Jour. Sed. Petr., Vol. 25, 4 pp. 273-281.

Ogniben, L., 1957, Secondary gypsum of the sulphur series, Sicily and the so-called integration: Jour. Sed. Pet., Vol. 27, 1, pp. 64-79.

Reed, F.S. and Mergner, J.L., 1953, Preparation of thin section : Amm. Min., Vol. 38, pp. 1184.

Shukri, N.M., 1956, The Geology of the Mediterranean Coast between Posetta and Bardia: Part III, Pleistocene Sediments, Mineral analysis: Bull. Inst. Egypt. 37(2), pp.445.

_____, and Said, R., 1966, The Geology of the Mediterranean Coast between Rosetta and Bradia: Part II, Plestocene Sediments, Geomorphology and Microfacies: Bull. Inst. Egypt. 37(2), pp. 395.

Usiglio, J., 1849, Concentration of sea water: Chem.(3), Vol.27. pp. g2 127.

الدراسة

يعتبر هذا البحث (٢) دراسة تكميلية للجزء الاول عن رواسب المتبخرات التي توجد على طول الساحل الشمالي لجمهورية مصر العربية الذى اختص بالدراسة الجيوكيميائية والمعدنية لهذه الرواسب.

يختص هذا الجزء بدراسة الوصف البتروجرافي لهذه الصخور ومناقشة المنشأة التتابعية لها. وقد قسمت هذه الصخور بتروجرافيا الى :- (أ) صخور الجبس وتشمل هذه الصخور الجبس المتبلورة الخشنة جدا وصخور الجبس الخشنة التحبب وصخور الجبس الدقيقة التحبب. (ب) رواسب الملاحات. (ج) الصخور المصاحبة للمتبخرات وتشمل طبقات الحجر الجيرى والمارل والطين والخرين الكلسي والجبس الحبيبي ورمال الجبس والكوارتز.

واعتمادا على الدراسات الحقلية والمعدنية والجيوكيميائية (من الجزء الاول) والدراسة البتروجرافية (للجزء الثاني) تمت مناقشة المنشأة التتابعية بالتفصيل.

CONTRIBUTION TO THE MINERALOGY OF SOME SYRIAN OIL-SHALES

Samir A. Hussein

Applied Geology Dept., Fac. Science,

Al-Mustansiriyah University,

Baghdad, Iraq

ABSTRACT

The Syrian Oil Shales have been studied in detail from petrological, chemical and mineralogical points of views. These deposits were reported within rocks of Cretaceous age, which consist mainly of limestone-phosphorite-black shale-chert assemblage. According to their mineralogical and textural features, they are classed as calcareous siltstones or carbonate-rich shales. Infrared and X-ray analyses of these shales, revealed the presence of organic constituents, quartz, calcite, dolomite and clay minerals (kaolinite, illite and montomorillonite). These shales are low-energy sediments and deposited under reducing conditions in shallow marine environments.

Al-Mustansiriyah Journal of Science, Vol. 2 (1977).

INTRODUCTION

At the beginning of this century, there are widespread efforts to seek possible substitutions for petroleum. One of these, is the accumulation of oil shale which have been the source products similar to those obtained from petroleum for a long time. According to Duncan et al. (1965), the amounts of oil that can be retorted from the oil shales range from 4% to more than 50% of the rock weight, or about 10-150 gal of oil per ton of rock.

The world occurrences of oil shale were reported by several workers, e.g. Jaffe (1962), Duncan et al. (1965) and Ozerov (1965). The oil shale deposit found in the Green River Formation, in the State of Colorado, Utah, and Wyoming (USA), is by far, the largest one and accounting for about 80% of the known world deposits. The oil contained in this formation is about 1800 billion barrels of recoverable oil. This figure reflects the economic potentialities of these deposits as a good source of energy. The oil shales of Australia, France and Scotland stand out as very important source of petroleum products for a long time. Other occurrence of oil shales have been reported to Sweden, China, Sicily, USSR, Yugoslavia, South Africa and Spain.

Numerous occurrence of oil shale deposits are known in several localities of Arabian countries, e.g. Algerie, Syria, Jordan, Palestine, Iraq and Liban. To the best of the writer knowledge, no previous detailed studies have been carried out on these shales. Interest to the development of these deposits has not been sufficient either to support through exploration and appraisal of known deposits or utilization of them as an energy source. However, they were

exploited only on a small scale for road paving.

The aim of the present study is therefore, to present the results of a detailed mineralogical, petrographic and geochemical investigations of the oil shales in Syria. Representative oil shale samples from different Syrian localities were collected and examined for this study. These localities are: Gebel Bosheri, Deir El-Zoor and Lazikyah. A general discussion of the environment of deposition and origin of these shales is also given.

Definition

Gavin (1924) defined the oil shale (bituminous shale) as follows: "Oil shale is a compact laminated rock of sedimentary origin, yielding over 33% of ash and containing organic matter that yields oil when distilled " . Brown (1927) was the first author to use the name "Kerogen" to denote specifically the insoluble organic matter in the oil shale. He used this term to cover the materials which on heating and decomposition give rise to shale oil. According to Yen et al. (1976), oil shales are diverse fine-grained sedimentary rocks which contain refractory organic constitutes that can be refined into fuels. Soluble bitumen fraction constitutes about 20% of this organic material, whereas the remainder exists as insoluble Kerogen. Yen et al. (1976) classified oil shales as "Composites" of tightly bound organic and inorganic materials. The ratio of organic to inorganic rarely exceeds 1:4,

Lithology and Petrography of Syrian Oil Shales

The oil shale deposits in Syria are widely distributed within the Cretaceous rocks, which consist mainly of limestone-phosphorite-black shale-chert assemblage. In this succession, the oil shales occur as thin bands and lenses intercalated within the whole Cretaceous rocks, and reachs to a maximum thickness of 2 m. Many thin but high grade oil shale deposits as well as extensive thicker lower grade accumulations were also included. They range in colour from high shales of brown, yellow, red to dark brown, grey or black and with satiny luster. Sometimes the black oil shales are found as minute seasonal pairs of laminae (varves), in which they occur as thin laminations of light and dark coloured materials. The latter being the result of inclusions of organic materials into the inorganic matrix (plate 1a). This microstratification structure indicates that the environmental conditions are not steady but varied on an annual, seasonal or irregular basis.

The oil shales are generally hard, compact and massive with a conchoidal fracture. Most of them weather in laminae, some of which are flexible and paper thin. Although most of them do not contain much oil as much, nearly all have at least small amounts of organic matters (bitumen) in the form of veinlets, veins or blebs of solid and viscous hydrocarbons.

In thin sections, oil shales consist of three main constituents: the detrital grains, the authigenic components and the organic matter.

The predominant detrital components of oil shales consist of clay minerals, in addition to few grains of quartz, orthoclase and plagioclase feldspars, sanidine and muscovite. About 75% of these

mineral matters consist of particle size varies between 2 and 20 u. i.e. silt size, 15% were less than 2 u. i.e. clay size and 10% ranged between 20 and 200 u. i.e. fine-sand size. Most of quartz and feldspars are either sharply angular or subangular ill-sorted and embedded in the argillaceous groundmass with a random arrangement, (plate 1b).

The authgenic minerals are represented by pyrite, calcite, dolomite and halite. Pyrite occurs in the form of diacoidal aggregates and spherules, however, cubes and other crystal forms are less common, (plate 1c). The granular occurrence of pyrite indicates that the sulfide is formed contemporaneously with the deposition. Calcite and dolomite occur as individual, microcrystalline rhombs and irregularly scattered through the sample, (plate 1d). In addition few crystals of halite are also detected within the argillaceous groundmass.

The major portion of the organic materials in the oil shales consists of the insoluble Kerogen, which is structureless, translucent and appears yellowish-amber, brown or brownish black colour in thin section, (plate 1e). Some of these organic constituents show some alteration as evidenced by their darkening. Few algal or plant remains are well preserved, but generally are not the predominant organic materkals present.

The mineral and textural features of these oil shales would allow them to be classed as calcareous siltstones or carbonate-rich shales.

Chemical analysis

Because of the insolubility of the oil shale samples, classical

a) Photomicrograph of oil shale sample, showing minute pairs of laminae (varves), in which thin laminations of light and dark coloured materials alternate with each others, plane polarized light, X25.

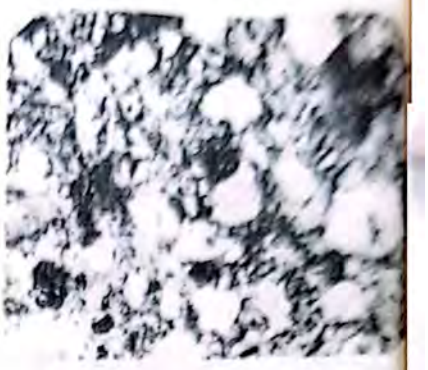

b) Photomicrograph of oil shale sample, showing fine sand size of quartz and feldspars embedded in the argillaceous ground-mass, X-nicols, X60.

Photomicrograph of oil shale sample, showing distributed pellets of pyrite the argillaceous groundmass, X-niclos, 0.

d) Photomicrograph of oil shale sample showing microcrystalline carbonates (calcite and/or dolomite) intermixed with the clay particles, X-nicols, 1

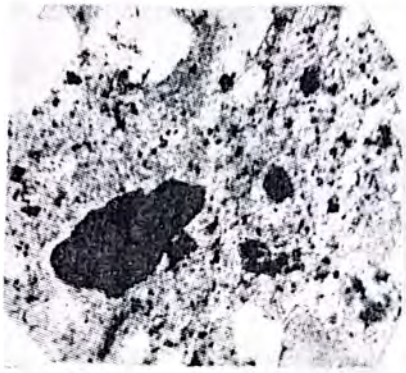

e) Photomicrograph of oil shale sample, showing translucent and structureless organic materials (Kerogen), X-niclos, X60.

Description of figures in plate - 1

chemical analysis has not provided such useful data on the chemical character of them. The elemental and infrared analyses give an excellent picture for all the constituents in oil shale samples.

Elemental analysis of the studied samples was carried out according to a modified scheme proposed by Saxby (1970) and the results are given in Table (1). The data in this Table is similar to those obtained by Himus (1951) and Robinson et al. (1967) for some Kerogen-rich rocks. According to them, these rocks range between the following limits: carbon-64% - 89%, hydrogen-7.1%-12.8%, nitrogen-0.1%-3.1%, sulphur-0.1%-8.7%, and oxygen-0.8%-24.8%.

The data can also be compared directly with other data of carbonaceous substances in various types of compositional diagrams. The Ralston diagram (modified by Cane, 1976) uses normalized C, H and O values to differentiate between petroleum, fats and coal. This diagram is shown in Fig. (1) which indicates that the investigated oil shale samples occupy an area between those of fatty acids, coal and petroleum.

A plot of H/C versus O/C atomic ratios* (Van Krevelen, 1961) is useful for comparing Kerogen and the source materials. Fig. (2) shows the plotted data obtained from Table (1) together with the elemental analysis of some other organic materials.

For simplicity and because of uncertainties in oxygen determination, Robenson et al. (1967) used hydrogen contents (or H/C atomic ratio) as a general indicators of terrestrial (low H/C) or marine (high H/C) source material of oil shales. Accordingly, the Syrian oil shales are considered to be of marine origin.

---

* H/C atomic ratio = 12 x %H/%C
O/C atomic ratio = 0.75x %O/%C

Table (1) Elemental analysis of the Syrian oil shale samples

	1	2	3	4
C	83.81	82.78	81.42	85.56
H	10.52	11.00	10.81	8.88
N	1.00	0.64	1.14	0.98
O	3.81	4.01	4.78	2.98
S	0.82	0.81	0.92	0.90
Cl	0.52	0.50	0.50	0.50
F	0.42	0.55	0.30	0.40
Ash	30.32	32.48	30.88	31.00
H/C	1.44	1.56	1.56	1.20
O/C	0.03	0.03	0.04	0.03

Fig.(11). Modified Ralston diagram showing possible precursors of Syrian oil shale.

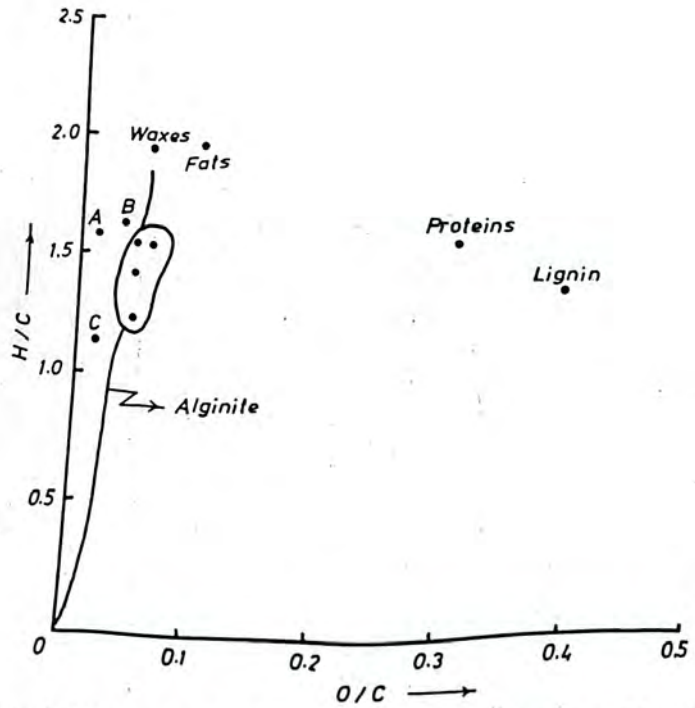

Fig.(2). Atomic H/C ratio versus O/C ratio of Syrian oil shales (circled), in addition to selected organic materials and other oil shale occurrences, e.g. A=Sydney Basin carbonaceous shale, B=Colorado oil shale, C= St. Hilaire oil shale (France).

The infrared analysis have been used also to supply evidence on the structure of the organic and inorganic constituents of oil shale samples. The infrared spectra were obtained using UNICAM SP. 1200 infrared spectrophotometer in the range between 4000 cm^{-1} and 400 cm^{-1}, and the analysis are shown in Fig.(1). Table (2) lists the wave lengths and description of the identified absorption bands. The nomenclature of these bands are based mainly on those obtained by Forsman (1963), Robinson (1969). Tissot et al. (1971), Keller et al. (1952), Smith (1961), Grim et. al. (1961), Stubican et al. (1961), Wolff (1965) and Serratosa et al. (1962). The identified absorption bands can be summarized as follows :

1. The vibration of organic groups is represented by five absorption groups:

   a) Strong absorption in the region (2900-3000) cm^{-1} assigned to both aromatic and aliphatic C-H bonds.

   b) Strong absorption in the (1680-1740) cm^{-1} region assigned to the C = O bonds.

   c) Medium absorption in the (1580-1620) cm^{-1} region assigned to the C = C bonds, carboxyl salts, aromatic structures and conjugated C = O bonds.

   d) Medium absorption in the (1370) cm^{-1} region assigned to CH_3 and cyclic CH_2 groups.

   e) Weak absorptions in the region (720-850) cm^{-1} showed the presence of condensed aromatic rings and aliphatic chains greater than C_4.

2. The vibration of inorganic groups is represented by the following:

Table (2) Nomenclature of infrared absorption spectra of Syrian oil shale.

Frequency cm^{-1}	Nomenclature	Description
3700	Structural OH	broad
3000-2900	Aromatic C-H, aliphatic C-H	strong
1740-1680	C = O	strong
1620-1580	C = C, carboxyl salts, aromatic structures, conjugated C = O	medium
1370	CH_3 , cyclic CH_2	medium
1100-1030	Si - O	medium
900	O - H - Al	strong
850-720	Condensed aromatic rings and aliphatic chains greater than C_4	weak
800	Si - O	weak
700	Si - O	weak
500	Si - O - Al	weak, broad
450	Si - O	medium

a) An absorption band in the 3700 cm^{-1} region corresponding to the vibration of the structural OH group caused by Kaolinite and montmorillonite.

b) The vibration of Si-O group is represented by several absorption bands in the range of 1100 cm^{-1} 1030 cm^{-1}, 800 cm^{-1}, 700 cm^{-1} and 450 cm^{-1}. These bands are characteristic of motmorillonite, kaolinite and illite.

c) The strong absorption in the region of 900 cm^{-1} assigned to O - H - Al group and is characteristic of montmorillonite, kaolinite and illite.

d) The vibration of Si-O-Al group is represented by a weak, broad absorption bands in the 500 cm^{-1} region and in characteristic of montmorillicnite, kaolinite and illite.

X-ray analysis

In order to identify the inorganic minerals present in oil shale samples, it is necessary to separate the organic materials before X-ray analysis of these samples. A variety of procedures aimed to the physical separation of organic matter have been described in detail by Forsman (1963), Robinson (1969) and Thomas et al. (1970). Such methods depend mainly upon flotation and centrifugation in pure or mixed heavy liquids, or on the different wettability properties of organic and inorganic matter in water and liquid hydrocarbons. In this work, Robinson (1969) method is used which involves centrifuging powdered oil shale samples in $CaCl_2$ solution (SP. Gr. = 1.01-1.15 g/cm^3) or in carbon tetrachloride - benzene mixtures (Sp. Gr. = 1.15-1.40 gm/cm^3). The final float concentrate

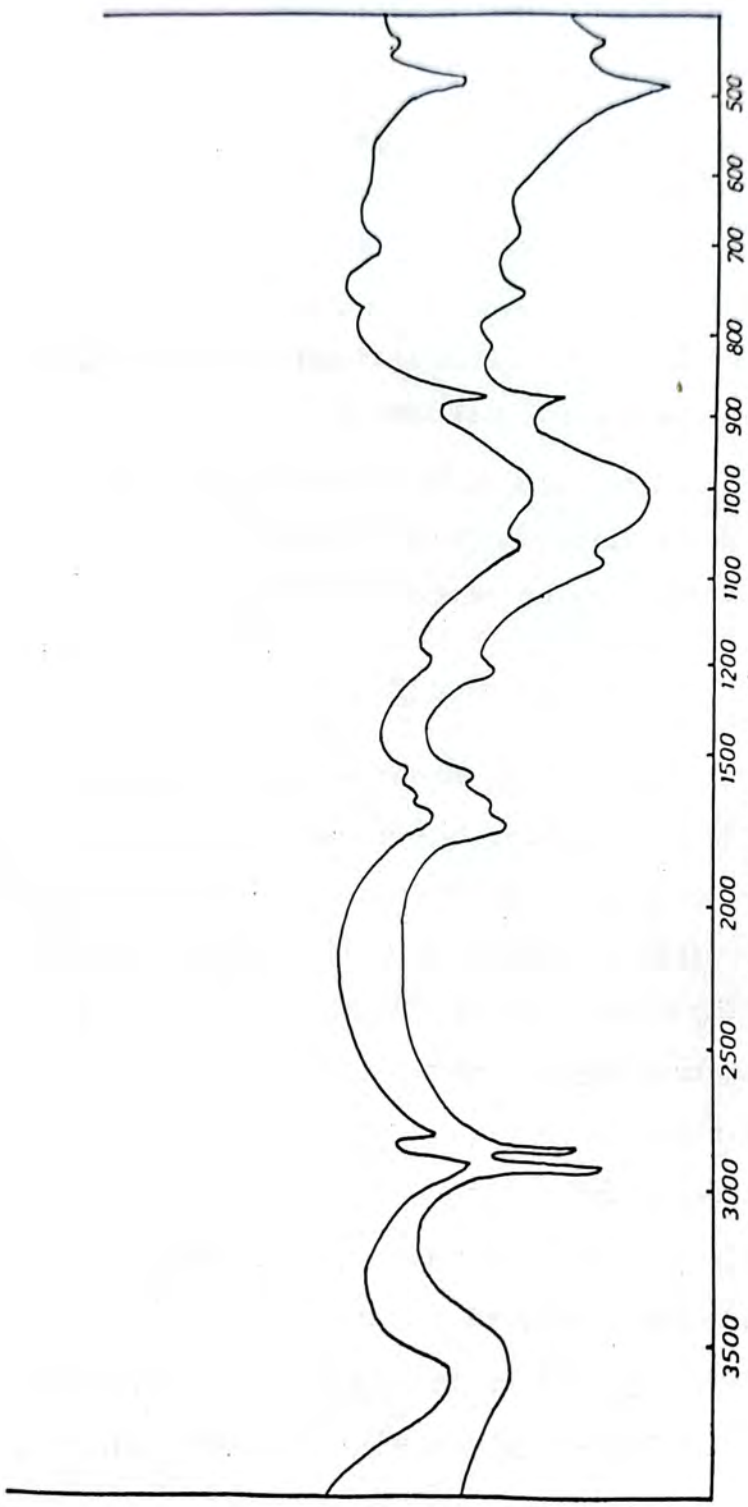

Fig.(3). Infrared absorption spectra of Syrian oil shale.

is separated from the settled inorganic materials.

X-ray diffraction analysis of the bulk sample (Fig. 4, and Table 3) reveals the presence of a number of non clay minerals, e.g. quartz, Calcite and dolomite. However to determine the clay minerals present in oil shales, three oriented mounts for the clay fractions ($< 2\mu$) was prepared and three diffraction patterns were run. i.e. untreated, glycolated and heated at 550°C for two hours (Grim, 1961, 1968). The data is presented in Fig. 5 and Table 4 which revealed the presence of kaolinite, illite and montmorillonite.

Kaolinite is characterized by a series of basal X-ray diffraction peaks at $\sim$ 7.1 Å (001), 3.5 Å (002) and so forth (Grim, 1968). Glycolation yields no noteworthy shift in the spacing or intensity of the peaks observed in the untreated sample. This pattern is completely destructed on heating the specimen to 550°C due to the collapse of the structure to an X-ray amorphous mineral.

Illite is characterized by a series of weak, broad X-ray diffraction at $\sim$ 10 Å (001) and $\sim$ 3.3 Å (003) that are not appreciably affected by either glycolation or heat treatment. Montmorillonite in the other hand, is characterized by its expanding lattice. When having Na or K as the exchange ion frequently has one molecular layer of water and a basal spacing of $\sim$ 12.5 Å . When Ca or Mg is the exchange ion, it frequently has two molecular water layers and a basal spacing of $\sim$ 15.5 Å (Grim, 1968). Upon glycolation a characteristic swelling from a d-spacing of 15 Å to one of $\sim$ 17 Å occurs. When heated at 550 °C for two hours, removal of the absorbed interlayer water causes a decrease in the basal spacings to $\sim$ 10 Å and a characteristic broad peak appears at 3.16 Å . This peak is not detected on both the untreated and the

Table (3) X-ray diffraction data of bulk sample of Syrian oil shale sample.

dÅ	I/I°
12.60	70
7.13	60
4.43	44
3.55	60
3.32	66
3.04	100
2.88	34
2.79	44
2.29	24
2.09	20
2.02	20
1.93	20
1.86	15
1.80	15

Minerals identified

Quartz: Using lines at d = 3.34, 4.26, 1.82 Å (ASTM card 5-0430)

Calcite: Using lines at d = 3.04, 2.29, 2.10 Å (ASTM card 5-0586)

Dolomite: Using lines at d = 2.88, 1.78, 1.80 Å (ASTM card 5-0622)

Fig. (4). X-ray chart of bulk oil shale sample.

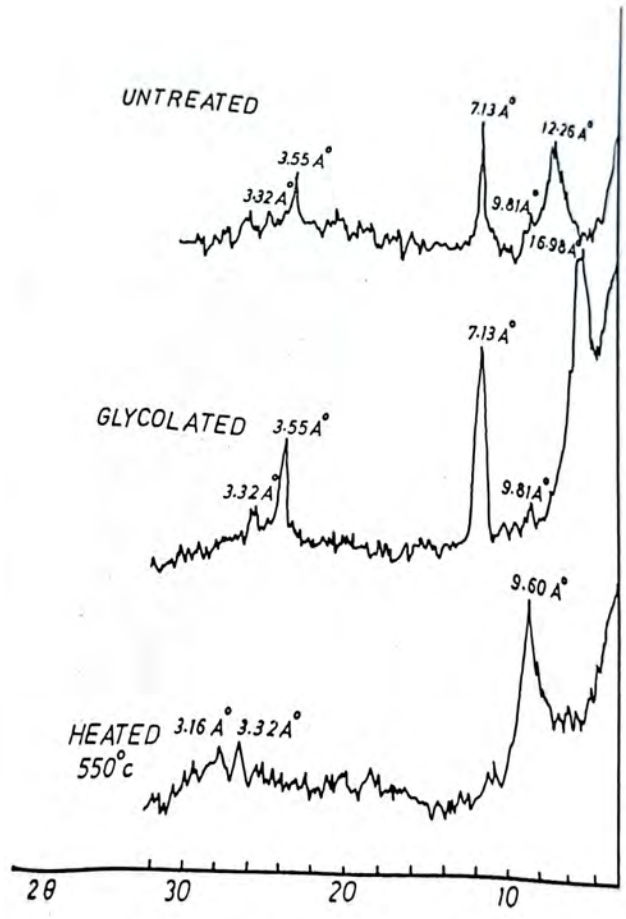

Fig.(5). X-ray diffraction patterns of clay fraction.

Table (4.) X-ray diffraction data of clay fraction of Syrian oil shale sample.

Untreated		Glycolated		Heated	
d Å°	I/I°	d Å°	I/I°	d Å°	I/I°
10.26	95	16.88	100	9.60	100
9.81	35	9.81	24	-	
7.13	100	7.13	67	-	
3.55	55	3.55	40	-	
3.32	25	3.32	17	3.32	25
				3.15	23

glycolated diffraction patterns and is a characteristic peak for the montmorillonite group.

Environment of deposition:

The oil shales result from contemporaneous deposition of fine grained sediments and organic degradation products derived from the breakdown of biota. Bradly (1931) proposed that the carbonaceous materials are derived from biological organisms that grew in aquatic environments. His conclusion was based upon the identification of microfossils in Green River Oil shale Formation. e.g. algae, fungi, protozoa, insects, bacteria and parts of higher plants (spores, pollen grains or minute pieces of tissue). Conditions required for the formation of these shales include abundant organic productivity, anaerobic conditions and a lack of destructive organisms.

The environmental conditions are mainly marine, as evidenced from the assemblage of clay and authigenic minerals present, and also from the hydrogen content of these shales (or atomic H/C ratio). According to Millot (1970) montmorillonite and illite indicated a typical marine environment. Degens et al. (1957) found an increase in the Kaolinite content as passing from the open marine environment to the continental one. Furthermore, Duncan (1967) stated that oil shale sediments deposited in large lacustrine basins are of calcareous type with associated sediments, tuffs, clastics, saline and carbonate minerals. This conclusion is concordant to the Syrian oil shales, which has been classed as calcareous siltstones. The find-grained texture (argillaceous to sandy) of the detrital sediments included in the oil shale is indicative of low energy environments, and supports this interpretation. So the Syrian oil shales appear to have been

deposited in shallow marine environments, e.g. lakes, bays, lagoons, marshes or seas. The microstratifications within the oil shale strata, show that the environmental conditions were not steady but varied annually, seasonally or irregularly.

Evidence for a highly reducing environments (low Eh) is the presence of pyrite and organic materials in the oil shale samples and complete absence of sulphate ions, which reflects the oxidising nature of the oceans and atmosphere, i.e. deposition in areas of limited water circulation. The carbonate (calcite and dolomite) and saline minerals halite, however, indicate an arid climate due to the evaporation of the original solution.

Conclusions:

As an example of Arabian oil-shale occurrence, representative samples from Syria are studied in detail. The oil shales occur as a thin bands and lenses intercalated within the Cretaceous strata. They composed of detrital grains (clays, quartz, orthoclase, plagioclase, sanidine and muscovite), authigenic components (pyrite, calcite, dolomite and halite) and organic materials. The mineral and textural features of these oil shales allow them to be classed as calcareous siltstones or carbonate rich-shales. Chemically, oil shales, occupy the compositional range between those of fatty acids, coal and petroleum. Infrared and X-ray analysis revealed the presence of organic constituents, quartz, calcite, dolomite and clay minerals represented by kaolinite, illite and montomorillonite. These shales are low-energy sediments and deposited under reducing conditions in shallow marine environments.

REFERENCES

ASTM of x-ray diffraction data, 1960. Amer. Soc. of testing materials, Phil., U.S.A.

Bradely, W.H., 1931. Origin and microfossils of the oil shale of the Green River Formation of Colorado and Utah. U.S. Geol. Surv. Profess. Pap., 168 : 58 pp.

Brown, C.A., 1927. The oil shales of the Lothians. (3rd ed.), Geol. Surv. Mem., Scotland : 274 pp.

Cane, R.F., 1976. The origin and formation of oil shale, in : Developments in petroleum science, 5 : 27-61.

Degens, E.T., Williams, E.G. and Keith, M.L., 1957. Environmental studies of carboniferous sediments. Pt. 1 Geochemical criteria for differentiating marine from fresh water shales. Bull. Am. Assoc. Pet., Geol. 41, 11 : 2427-2455.

Duncan, D.C. and Swanson, V.E., 1965. Organic-rich shale of the United States and World Land Areas. U.S. Geol. Surve., Circ. 523 : 30 pp.

Duncan, D.C., 1967. Geologic setting of oil shale deposits and world prospects. In : Proc. 7th World Pet. Congr., 3 : 659-667.

Foreman, J.P., 1963. Geochemistry of kerogen. In : I.A. Breger (Editor), "Organic geochemistry" Pergamon, Oxford, Ch. 5 : 148-182.

Gavin, J.M., 1924. Oil shale. Washington Government Printing Office : 201 pp.

Grim, R.E. and Kulbicki, G., 1961. Montmorillonite: high temperature reactions and classifications. Amer. Miner., 46 : 1329-1369.

Grim, R.E. 1961. Some applications of clay mineralogy. Amer. Miner., 45, 3-4 : pp. 259-270.

---------- 1968. Clay mineralogy. McGraw - Hill Book Co., New York 596 pp.

Himus, G.W., 1951. Observations on the composition of kerogen and the chemical constitution of Kerogen. In : Oil shale and cannel coal, 2. Institute of Petroleum, London : 112-133.

Jaffe, F.C., 1962. Oil shale. I-Nomenclature, Uses, Reserves, and Products. Colo. Sch. Mines, Miner. Ind. Bull., 5(2) : 11 pp.

Keller, W.D., Spotts, J.H. and Biggs, D.L., 1952. Infrared spectra of some rock forming minerals. Amer. Jour. Sci., 50 : 453-471.

Millot, G., 1970. Geology of clays. Springer-Verlag, New York : 429 pp.

Ozerov, G., 1965. Progress and prospects in the utilization of oil shale. U.N. Dep. Econ. Soc. Aff., Resour. Transp. Div., New York, Pap. 1 : 102 pp.

Robinson, W.E. and Dinneen, G.U., 1967. Constitutional aspects of oil shale Kerogen. Proc. 7th World Pet. Congr. (Mexico): 669-680.

Robinson, W.E., 1969. Kerogen of the Green River Formation. In : G. Eglinton and M.T.J. Murphy (Editors). "Organic Geochemistry", Springer, Berlin, Ch. 26 : 619-637.

Saxby, J.D., 1970. Isolation of Kerogen in sediments by chemical methods. Chem. Geol., 6 : 173-184.

Serratosa, J.M., Hidalgo, J.M.A. and Vinas, J.M., 1962. Orientation of OH bonds in Kaolinite. Nature, 195 : 486 - 487.

Smith, J , W., 1961. Ultimate composition of organic material in Green River Oil Shale. U.S. Bur. Mines Rep. Invest., 5725 : 1; pp.

Stubican, V. and Roy, R., 1961. Isomorphous substitution and infrared spectra of the layer lattice silicates. Amm. Miner., 46 : 32-52.

Thomas, R.D. and Lorenz, P.B., 1970. Use of centrifugal separation to investigate how Kerogen is bound to the minerals in oil shale U.S. Bur. Mines, Rep. Invest. : 7378.

[illegible]ot, B., Bebyser, C.Y., Deroo, G. and Oudin, J.L., 1971. Origin [illegible] evol[illegible]n [illegible] [illegible]rnons in Early Toarcian shales,

الخلاصـــــــة

يختص هذا البحث بدراسة الطين الزيتي من القطر السوري من النواحي الصخرية والكيميائية والمعدنية وقد تم التعرف على هذه الصخور ضمن رواسب العصر الطباشيري. وتبعا لتركيبها المعدني والنسيجي فقد صنفت الى الغرين الجيري او صخور طينية غنية بالكربونات. وقد اثبتت التحاليل بالاشعة السينية والاشعة تحت الحمراء عن وجود مكونات عضوية ومعادن الكوارتز والكالسيت والدولوميت وبعض معادن الطين ممثلة بالكاولينايت (طين خاوة) والايليت والمنتومورلينايت. وقد تمت ايضا

THE QUANTUM STATISTICS OF LINEAR SCATTERING

Hikmat Dawood Simaan
Physics Department
College of Science
Al-Mustansiriyah University

ABSTRACT

The process of linear inelastic scattering is treated theoretically from the quantum statistical point of view. An equation of motion for the probability amplitude that the system is in a certain state is derived and then solved analytically by the technique of generating functions. The solution obtained is quite general and enables computation of the probability districution for arbitrary time and any initial conditions. With the help of these results, the moments of the distribution are obtained and finally the statistical properties of the system are discussed.

INTRODUCTION

The process of linear incoherent Rayleigh and Brillouin Scattering has been treated theoretically by many authors (1-3). It takes place simply due to the interaction of the incident and scattered light beams with the group of atoms within the system. In each elementary scattering event of the process, this kind of interaction destroys an incident photon with the frequency w and creates a scattered photon of the same frequency as that of the incident. This implies that the scattering is elastic and the atoms play the role of passive medium only. The inelastic scattering due to the Raman effect has also been treated by us lately (4), where the statistical properties of the light beams concerned are extensively investigated. Before that we have also studied the problem of quantum statistics of the two-photon absorption (5 , 6).

Al-Mustansiriyah Journal of Science, Vol. 2 (1977).

The purpose of this paper is to consider, in some detail, the above mentioned problem of the linear scattering from the quantum statistical point of view. On using a certain linearization and approximation, the author of reference 2 has briefly described and discussed the process. Here we shall use a similar Hamiltonian as that of reference 2, but obtain more exact and general results by using a somewhat different approach in formulating and solving the problem. The Hamiltonian used here is a phenomenological one and depends on the boson creation and destruction operators. It can also be used to study the interaction between two coupled oscillators or in general any two quantum mechanical coupled systems (7-9).

An equation of motion for the probability amplitude that the system is in a certain state is derived by a well known quantum mechanical method, used by different authors (10 , 11), in order to describe similar problems. On using a generating function method similar to that employed by the authors of references 5 and 6, the equation of motion is exactly solved and an expression for the time dependence of the probability amplitude is derived which is then used to write down an expression for the probability distribution given by the square value of the probability amplitude. With the help of these results, the moments of the distribution are obtained and finally the statistical properties of the system are discussed.

FORMULATION OF PROBLEM

The total Hamiltonian, proposed by the authors of references 2,3,7 and 8, which describes the linear incoherent Rayleigh and Brillouin scattering or/and the interaction between two coupled systems, may be expressed as

$$H = \hbar w(a_1^+ a_1 + a_2^+ a_2) + \hbar\lambda a_1 a_2^+ + \hbar\lambda^* a_1^+ a_2 \qquad (1)$$

where $\hbar = h/2\pi$, while h is the Planck's constant, w is the frequency of both the incident and scattered beams of light, and λ is the coupling constant. a_1 and a_1^+ are the boson annihilation and creation operators for the incident photons, while a_2 and a_2^+ are the corresponding operators for the scattered photons. They obey the familiar commutation relations :

$$\left[a_k , a_{k'}^+\right] = \delta_{kk'} \qquad (2a)$$

$$\text{and } \left[a_k , a_k\right] = \left[a_k^+ , a_{k'}^+\right] = 0 \qquad (2b)$$

If we denote the number of quanta $\hbar w_k$ in the field mode k by n_k, the states $|n_k\rangle$ from a complete orthogonal basis for the description of the states of the mode. The way in which the operators a_k and a_k^+ act upon these states is indicated by the relations

$$a_k \left| n_k \right\rangle = (n_k)^{\frac{1}{2}} \left| n_k - 1 \right\rangle \qquad (3a)$$

$$a_k^+ \left| n_k \right\rangle = (n_k + 1)^{\frac{1}{2}} \left| n_k + 1 \right\rangle \qquad (3b)$$

$$a_k^+ a_k \left| n_k \right\rangle = n_k \left| n_k \right\rangle . \qquad (3c)$$

Now we present the quantum mechanical approach to the problem. Consider the coupled system of radiation and atom described in the Schrodinger representation by a wave function $\Phi(t)$ which satisfies the wave equation

$$H \Phi(t) = i\hbar \frac{\partial}{\partial t} \Phi(t), \tag{4}$$

where H is the total time-independent Hamiltonian of the coupled system. The formal solution of equation (4) for the wavefunction at time t, expressed in terms of the wavefunction at an earlier time t = 0, is given by

$$\Phi(t) = \exp(-iHt/\hbar)\, \Phi(0). \tag{5}$$

The exponential quantity is the time-development operator for the system (12). Now if the probability amplitude that the system is in state Ψ_f at time t is represented by A(t), then

$$A(t) = \left\langle \Psi_f \middle| \exp(-iHt/\hbar) \middle| \Phi(0) \right\rangle . \tag{6}$$

This is in fact the overlap integral of Ψ_f and $\Phi(t)$, and the square value of it gives the probability distribution which is usually used to obtain the required information about the system under consideration.

Any practical beam of light contains a statistical distribution of photon numbers. Let us first assume that at time t = 0, the incident and scattered beams contain n_0 and m_0 photons respectively. Therefore, if n and m are the corresponding numbers of photons at any time t, then in Fock representation we can write

$$|\Psi_f\rangle = |n,m\rangle \tag{7a}$$

$$|\Phi(0)\rangle = |n_0,m_0\rangle . \tag{7b}$$

Now with the help of these relations, together with (1) and (3),

quation (6) can be differentiated to give

$$i\frac{d}{dt} A_{n,m} = w(n+m) A_{n,m} + \lambda\left\{(n+1)m\right\}^{\frac{1}{2}} A_{n+1,\,m-1} + \lambda^{*}\left\{n(m+1)\right\}^{\frac{1}{2}} A_{n-1,\,m+1} \qquad (8)$$

here

$$A_{n,m} = \left\langle n,m \right| \exp(-iHt/\hbar) \left| n_o, m_o \right\rangle , \qquad (9)$$

nd at time t = 0, we have

$$A_{n,m}(0) = \delta_{nn_o}\,\delta_{mm_o} \qquad (10)$$

his means that both the incident and scattered beams are initially umber-state beams of light.

In order to write (8) in a more convenient form, we first eliminate the imaginary factor by means of the simple transformation.

$$B_{n,m}(t) = (-i)^{m}(n!\,m!)^{-\frac{1}{2}} \exp\left\{iw\,(n+m)t\right\} A_{n,m}(t). \qquad (11)$$

n this way, equation (8) becomes

$$\frac{d}{dt} B_{n,m} = \lambda^{*}\,(m+1)B_{n-1,m+1} - \lambda\,(n+1)B_{n+1,m-1}\,. \qquad (12)$$

Now, the equation has real coefficients, so the amplitude $B_{n,m}$ is real.

The system of difference differential equations of which (12) is a representative, only couples those elements of the probability amplitude $B_{n,m}$ for which

$$\nu = n + m = \text{constant of the motion} \qquad (13)$$

where ν is a new variable which ranges from 0 to ∞ in integer steps. With the help of this relation, (12) takes the form

$$\frac{d}{dt}\theta_m(\nu,t) = \lambda^*(m+1)\,\theta_{m+1}(\nu,t) - \lambda(\nu-m+1)\,\theta_{m-1}(\nu,t) \quad (14)$$

$$\frac{d}{dt}\theta_n(\nu,t) = \lambda^*(\nu-n+1)\theta_{n-1}(\nu,t) - \lambda(n+1)\theta_{n+1}(\nu,t) \quad (15)$$

where

$$\theta_m(\nu,t) = B_{\nu-m,m}(t) \quad (16)$$

$$\theta_n(\nu,t) = B_{n,\nu-n}(t) \quad (17)$$

It is clear, that for a given ν, this set of rate equations has only a single variable n or m, instead of the pair of variables, n and m, which are apparently coupled in the original form of (12).

A full account of the method of dividing the set of difference equations is given in (6) for the double-beam two-photon absorption process, although this case is more complicated in that ν ranges from $-\infty$ to ∞, instead of the range 0 to ∞ for the present problem of the linear incoherent Rayliegh and Brillouin scattering. Finally, it is worth mentioning here that the approach followed above in order to derive the equation of motion for the probability amplitude has also been followed by the authors of reference 10, in their treatment to the problem of coherent spontaneous emission.

METHOD OF SOLUTION

We are now in a position to attack the dynamical problem based on the Hamiltonian (1) and on the related Schrodinger equations (14)

and (15) which are in Fock representation. These equations in fact prove tractable to solution by the generating function technique, which has been widely used lately in treating similar equations (5 , 6). We define the generating function $F(x, \nu, t)$ as

$$F(x, \nu, t) = \sum_m x^m \theta_m (\nu, t). \tag{18}$$

On multiplication of both sides of (14) by x^m and summation over m, we obtain the following first order partial differential equation

$$\frac{\partial F}{\partial t} = (\lambda^* + \lambda x^2) \frac{\partial F}{\partial x} - \lambda \nu x F. \tag{19}$$

Here we will use Lagrange's method to solve the last equation, rather than employ the usual laplace transform method because of the simplicity and power of the former method. Reference is made to (13) for an excellent account of the method.

Subsidiary equations of Lagrange are

$$\frac{dt}{1} = \frac{dx}{-(\lambda^* + \lambda x^2)} = \frac{dF}{-\lambda \nu x F}. \tag{20}$$

The first and second expressions give

$$\tau + \tan^{-1} \Lambda = \text{constant}, \tag{21}$$

where

$$\tau = (\lambda^* \lambda)^{\frac{1}{2}} t \tag{22}$$

$$\Lambda = (\lambda / \lambda^*)^{\frac{1}{2}} x , \tag{23}$$

while the second and third terms yield

$$\Gamma\left\{ (\lambda^*/\lambda) + x^2 \right\}^{-\frac{\nu}{2}} = \text{constant} . \qquad (24)$$

The general solution of (19) therefore can be written as

$$F(x,\nu,t) = \left\{ (\lambda^*/\lambda) + x^2 \right\}^{\frac{\nu}{2}} \Gamma(\tau + \tan^{-1} x), \qquad (25)$$

where $\Gamma(\quad)$ is an arbitrary function to be determined by using the initial condition, obtained from (18) and (25) by putting $t = 0$:

$$F(x,\nu,0) = \sum_{m_o} x^{m_o} \theta_{m_o}(\nu,0)$$

$$= \left\{ (\lambda^*/\lambda) + x^2 \right\}^{\frac{\nu}{2}} \Gamma(\tan^{-1} x). \qquad (26)$$

By setting

$$U = \tan^{-1} x , \qquad (27)$$

we immediately get

$$x = (\lambda^*/\lambda)^{\frac{1}{2}} \tan U, \qquad (28)$$

where (23) has been used, and therefore from (26) we get :

$$\Gamma(U) = \left\{ (\lambda^*/\lambda) + (\lambda^*/\lambda)\tan^2 U \right\}^{\frac{-\nu}{2}} \sum_{m_o} \theta_{m_o}(\nu,0)$$

$$\left\{ (\lambda^*/\lambda)^{\frac{1}{2}} \tan U \right\}^{m_o} \qquad (29)$$

Using this on the right hand side of (25), we obtain

$$F(x,\nu,t) = \left\{(\lambda^*/\lambda) + x^2\right\}^{\frac{\nu}{2}} \left\{(\lambda^*/\lambda)+(\lambda^*/\lambda)\tan^2 (\tau + \tan^{-1}\lambda)\right\}^{-\frac{\nu}{2}} \times \sum_{m_o} \theta_{m_o}(\nu,0)\left\{(\lambda^*/\lambda)^{\frac{1}{2}} \tan(\tau + \tan^{-1}{}_{\times})\right\}^{m_o} . \quad (30)$$

is can be rearranged to read

$$F(x,\nu,t) = \sum_{m_o} \theta_{m_o}(\nu,0)\left\{\cos\tau\left[x+(\lambda^*/\lambda)^{\frac{1}{2}}\tan\tau\right]\right\}^{m_o} \times \left\{-(\lambda/\lambda^*)^{\frac{1}{2}}\sin\tau\left[x-(\lambda^*/\lambda)^{\frac{1}{2}}\cot\tau\right]\right\}^{m_o} \quad (31)$$

The generating function provides a simple means of obtaining ie probability amplitudes. Making use of (18), we can write

$$\theta_m(\nu,t) = (m!)^{-1}\left\{\partial^m F/\partial x^m\right\}\ x = 0 . \quad (32)$$

erefore on using the Leibnitz's formula (for the m-th derivative the product of two functions), in order to obtain the m-th rivative of the generating function F, we immediately get :

$$\theta_m(\nu,t) = \sum_{k=0}^{m} \sum_{m_o=k}^{\nu} \frac{(-1)^{k-m}(\lambda^*/\lambda)^{(m_o-m)/2}\ m_o!(\nu-m_o)\ (\tan\tau)^{m_o+m-2k}(\cos\tau)^{\nu}}{k!\,(m-k)!\ (m_o-k)!\ (\nu-m_o-m+k)!} \times \theta_{m_o}(\nu,0), \quad (33)$$

here $\theta_{m_o}(\nu,0)$ is the initial photon probability amplitude, and τ is given by (22).

All the above analysis has been concerned with the difference differential equation (14), whence we determine the general time-dependence of the probability amplitude $\theta_m(\nu, t)$, given by (33). The difference equation (15) for $\theta_n(\nu, t)$ can also be solved by the same technique, but this is not necessary as we are able to find an expression for $\theta_n(\nu, t)$ directly from (33) by a simple substitution for m from (13).

DISCUSSION AND SPECIAL CASES

Equations (14) and (15) respectively govern the change of the statistical properties of the photon system in the two light beams, scattered and incident, due to the linear incoherent Rayleigh and Brillouin scattering. The analytical solution given by (33) therefore provides the maximum degree of statistical information that can be known about the system at certain time t. When the system has a well defined state at t=0. Equation (33) gives the time-dependent probability amplitude $\theta_m(\nu; t)$ which is related to $A_{\nu-m,n}(t)$ through the simple relations (16), (13) and (11). It is usually more convenient to deal with the probability distribution rather than the probability amplitude. The former quantity, denoted by $P_{-m,m}(t)$ is given by the square value of the latter,

$$P_{\nu-m,m}(t) = \left| A_{\nu-m,m}(t) \right|^2 . \qquad (34)$$

This is a direct consequence of the quantum mechanical rule that defines the probability distribution as the square value of the over-lap integral given in (6). Once the probability distribution is known, then its r-th moment $\overline{m^r}(t)$, can easily be determined from

the relation (5 , 6)

$$\overline{m^r}(t) = \sum_{\nu} \sum_{m} m^r P_{\nu-m,m}(t) \qquad (35)$$

In a similar way, an expression for the r-th moment $\overline{n^r}(t)$ can also be written in terms of the probability distribution $P_{n,\nu-n}(t)$.

The coupling constant λ and its complex value λ^* are related to each other through the relation $\lambda^* = |\lambda| \exp(-i\alpha)$, where α gives the phase difference. For simplicity let us assume here that $\alpha = 0$, and therefore on using (16), (11) and (10) respectively in (33) we shall obtain an expression for the probability amplitude $A_{\nu-m,m}(t)$, which then can be used in (34) to write

$$P^{NS}_{\nu-m,m}(t) = \frac{(\nu-m)!\,m!}{(\nu-m_0)!\,m_0!} \left| \sum_{k=0}^{m_0} \frac{(-1)^{k-m_0} m_0!\,(\nu-m_0)!\,(\cos\lambda t)\,(\tan t)^{m_0+m-2k}}{k!\,(m-k)!\,(m_0-k)!\,(\nu-m_0-m+k)!} \right|^2 \qquad (36)$$

The superscript NS denotes that at time t=0, the incident and scattered beams of light are taken to be two number-state distributions, which are given by the right hand side of (10), where n_0 and m_0 are respectively the number of photons initially present in each beam.

As a special case, let us assume that initially at t=0, the scattered beam has no photons. Therefore $m_0=0$ and (36) can be simplified to read

$$P^{NS}_{\nu-m,m}(t) = \binom{\nu}{m} (\sin^2\lambda t)^m (\cos^2\lambda t)^{\nu-m} \qquad (37)$$

where $$\binom{\nu}{m} = \nu!/(\nu-m)!\,m! \qquad (38)$$

is the normal binomial coefficient. It is worth noting here that the variable m ranges from 0 to $\mathcal{N}$, and on summation of both sides of (37) over this variable, we immediately get the result of unity for the probability that the radiation field contains $\mathcal{N}$ photons. This is a direct consequence of the fact that $\mathcal{N}$ is given by (13).

Any-how for a given $\mathcal{N}$, equation (37) represents the time-dependence of the probability distribution for the system when initially the incident and scattered beams are both number-state beams with $n_o \neq 0$ and $m_o = 0$ respectively. If $n_o = 1$ for example, then $\mathcal{N} = 1$ and the allowed values of m will be either 0 or 1. This means that

$$P^{NS}_{1,0}(t) = \cos^2 \lambda t \tag{39}$$

and

$$P^{NS}_{0,1}(t) = \sin^2 \lambda t \tag{40}$$

are the only non-vanishing components of the distribution, which can be used in (35) to find that the first moments, $\bar{n}$ of the incident beam and $\bar{m}$ of the scattered beam are respectively given by the right hand sides of (39) and (40). This is an interesting result since it shows that for a certain interval of time immediately after the commencement of the process, the incident beam decays out as the scattered beam grows up. In the second interval, the process repeats itself but in a reverse order so that the incident and scattered beams change places, while in the third interval the process again is similar to that of the first, and so on successively. This behavior in fact has some resemblance to that of the second harmonic generation process, treated semiclassically by many authors (14 , 15).

All the above remarks apply to the case of no scattered photons at $t = 0$, where the incident beam has a number-state distribution with n_o photons. Any other cases different from this are much more complicated, and for most times simple conclusions are not available. In any case, the results obtained in the last section are exact and general and with the aid of computers can easily be evaluated for any initial types of distribution. The most important ones could be used for this purpose are the coherent and thermal distributions given in reference 5. A single-mode laser well above threshold is a good approximation of the coherent type, while lasers below threshold and conventional light sources provide distributions of the thermal type. Finally we conclude by saying that the results obtained in this paper should be of much use for the experimental physicists that are interested in doing experimental work about the Rayleigh and Brillouin scattering, especially much work has been done lately in this field of research by different groups of physicists (16 , 17).

REFERENCES

(1) L.D. Landau and E.N. Lifshitz, 'Electrodynamics of continuous media' , (New York, 1960), P. 377.

(2) Y.R. Shen, Phys. Rev., 155, 921 (1967).

(3) Y.R. Shen, 'Quantum Optics', edited by R.J. Glauber (Academic Press; New York,(1969).

(4) H.D. Simaan, J. Phys. A: Math. Gen., 8, 1620 (1975).

(5) H.D. Simaan and R. Loudon, J. Phys. A: Math. Gen., 8, 539 (1975

(6) H.D. Simaan and R. Loudon, J. Phys. A: Math. Gen., 8, 1140(1975

(7) D.F. Walls, Z. Physik, 234, 231 (1970).

(8) G.J. Iafrate and M.Croft, Phys. Rev. A, 12, 1525 (1975).

(9) H. Prakash and N. Chandra, Indian J. Pure Appl. Phys., 14, 48 (1976).

(10) R. Bonifacio and G. Preparata, Phys. Rev. A, 2, 236 (1970).

(11) D.F. Walls and C.T. Tindle, J. Phys. A: Gen., 5, 534 (1972).

(12) R. Loudon 'The quantum theory of light', (Oxford : Clarendon, 1973).

(13) N.T. Bailey 'The elements of stochastic processes with applications to the natural sciences', (New York : Wiley, 1964), Chap. 1 and 8.

(14) N. Bloembergen, 'Nonlinear Optics', (New York : Benjamin, 1965) and the papers reproduced therein.

(15) P.N. Butcher, 'Nonlinear optical phenomena', (Columbus : Ohio State Univ., 1965).

(16) T. Soki, Y. Okabe, and K.Sakurai, Phys. Rev. A, 10, 259 (1974

(17) J. Meyer and G.G. Albach, Phys. Rev. A, 13, 1091 (1976).

CHARACTERIZATION OF

MULTIVARIATE GENERALIZED POWER SERIES DISTRIBUTIONS

Rafid S. Abdul Razak and Mohammad S.A. Ahmed
Dept. of Stat., College of Adm. and Econ., University of Baghdad, Baghdad, IRAQ
Dept. of Math., College of SCI., University of Baghdad, Baghdad, IRAQ

Key Words and Phrases: Multivariate Generalized Power Series Distributions, Characterization.

1- INTRODUCTION

The multivariate generalized power series distribution has been studied by Kosambi, Noack, Khatri, Patil and other authors. In particular, Khatri proved that the multivariate power series distribution (PSD) is uniquely determined if the vector of means and the variance-covariance matrix are given. This result has been stated and used by several authors.

In this paper, after defining the multivariate generalized power series distribution (GPSD) we obtain many recurrence relations for the moments. The interesting result proved (contrary to the statement of Khatri) is that, under reasonable conditions, the multivariate GPSD is uniquely determined if any element of the vector of means or the variance-covariance matrix is given.

This paper gives generalization of the results obtained in the thesis (see -1-) submitted by one of the authors.

2- Definition of the n-variate GPSD

The definition given below is a slight generalization of that given by Patil (see -7- p.225). The need for this generalization is needed to prove that the marginals are also GPSDs.

Let $\underline{\lambda} = (\lambda_1, \ldots, \lambda_m) \in L \subset R^m$ where R^m is the set of m-ordered non-negative numbers and $\underline{x} = (x_1, \ldots, x_n) \in S \subset I_+^n$ where I_+^n is the set of all n-ordered non-negative integers. Assume that the series

$$\sum_{\underline{x} \in S} a_{\underline{x}}(\underline{\lambda})\, \theta_1^{x_1} \ldots \theta_n^{x_n}$$

with $a_{\underline{x}}(\underline{\lambda}) \geqslant 0$ for all $\forall\, \underline{x} \in S$ and $\forall\, \underline{\lambda} \in L$ is convergent

$$\forall\, \underline{\theta} = (\theta_1, \ldots, \theta_n) \in T,$$

where $T = \langle 0, r_1) \times \ldots \times \langle 0, r_n)$. Denote the sum of the series by

$f(\underline{\theta}, \underline{\lambda})$. Then $f(\underline{\theta}, \underline{\lambda}) > 0$ if $\theta \in \overline{T}$

$= (r_1', r_1) \times \ldots \times (r_n', r_n) \subset T$.

The n-variate discrete r.vc. $\underline{X} = (X_1, \ldots, X_n)$ having j.p.f.

$$P_{\underline{X}}(\underline{x}/\underline{\theta}, \underline{\lambda}) = \begin{cases} a_{\underline{x}}(\underline{\lambda})\theta_1^{x_1} \ldots \theta_n^{x_n} / f(\underline{\theta}, \underline{\lambda}) & \text{if } x \in S \\ 0 & \text{otherwise} \end{cases}$$

for every $(\underline{\theta}, \underline{\lambda}) \in \overline{T} \times L$ is said to have a n-variate GPSD. The n parameters $\theta_1, \ldots, \theta_n$ will be called the active parameters, the m parameters $\lambda_1, \ldots, \lambda_m$ will be called the inactive parameters, and the function $f(\underline{\theta}, \underline{\lambda})$ is called the defining function.

We remark that there is no other way of defining a n-variate GPSD in n active and m inactive parameters.

For purpose of abbreviation, throughout the paper, we shall write "the r.vc. $(X_1, \ldots, X_n)$" to mean a n-variate discrete r.vc. $(X_1, \ldots, X_n)$ having a GPSD as defined above.

3- Marginal Distributions

Consider the r.vc.$(\Lambda_1,\ldots,\Lambda_n)$. Then the p.f. of the marginal r.v. say Λ_1 is given by

$$P_{X_i}(x_i/\underline{\theta},\underline{\lambda}) = \begin{cases} \sum_{\underline{x}\in S} a_{\underline{x}}(\underline{\lambda})\theta_1^{x_1}\ldots\theta_i^{x_i}\ldots\theta_n^{x_n}/f(\underline{\theta},\underline{\lambda}) & \text{if } x_i\in S_i \\ 0 & \text{otherwise} \end{cases}$$

for every $(\underline{\theta},\underline{\lambda})\in\bar{T}\times L$ and that $S_i=\{x_i/\underline{x}\in S\}$ Note that x_i is fixed during summation. Simplifying the above expression, we get

$$P_{\Lambda_i}(x_i/\underline{\theta},\underline{\lambda}) = \begin{cases} a^*_{x_i}(\theta_1,\ldots,\theta_{i-1},\theta_{i+1},\ldots,\theta_n,)\theta_i^{x_i}/f(\underline{\theta},\underline{\lambda}) & \text{if } x_i\in S_i \\ 0 & \text{otherwise} \end{cases}$$

for every $(\underline{\theta},\underline{\lambda})\in\bar{T}xL$.

The conclusion obtained is important and is rewritten as

Theorem 1: Consider the r.vc. $(\Lambda_1,\ldots,\Lambda_n)$. The marginal r.v. Λ_i has a GPSD in 1 active parameter and n-1+m inactive parameters $\theta_1,\ldots,\theta_{i-1},\theta_{i+1},\ldots,\theta_n,\lambda_1,\ldots,\lambda_m$. The defining function of the marginal r.v. Λ_i is also $f(\underline{\theta},\underline{\lambda})$.

It is very important to note that the defining function for the r.vc. $(\Lambda_1,\ldots,\Lambda_n)$ and the defining function for the marginal r.v. Λ_i is the same function $f(\underline{\theta},\underline{\lambda})$ whatever be i=1,2,...,n. To obtain the j.p.f. of the r.vc. $(\Lambda_1,\ldots,\Lambda_n)$ we expand $f(\underline{\theta},\underline{\lambda})$ as a n-variate power series in the n active parameters $\theta_1,\ldots,\theta_n$ but to obtain the p.f. of the marginal r.v. Λ_i we expand $f(\underline{\theta},\underline{\lambda})$ as a power series in 1 active parameter θ_i. This obvious but otherwise a very important conclusion was overlooked by all of the previous authors on the subject of GPSDs.

4- Moments and Recurrence Relations

It is easily verified by using the well-known differentiation properties of the n - variate power series that for the r.vc. $(\lambda_1,\ldots,\lambda_n)$, the multimoment $\mu'_{r_1,\ldots,r_n}$ is given by

$$(4.1)\qquad \mu_{r_1,\ldots,r_n} = E(\lambda_1^{r_1}\cdots\lambda_n^{r_n})$$

$$= \lfloor 1/f(\underline{\theta},\underline{\lambda}) \rfloor (\theta_1 D_1)^{r_1}\ldots(\theta_n D_n)^{r_n} f(\underline{\theta},\underline{\lambda})$$

where $D_i = \dfrac{\partial}{\partial\theta_i}$ $i=1,2,\ldots,n.$

In particular, the mean $m_1(i)$ of the marginal r.v. λ_i is given by

$$(4.2)\qquad m_1(i) = \mu_{0,\ldots,0,1,0,\ldots,0} = E(\lambda_1^0\ldots\lambda_{i-1}^0\lambda_i^1\lambda_{i+1}^0\ldots\lambda_n^0)$$

$$= \lfloor 1/f(\underline{\theta},\underline{\lambda}) \rfloor (\theta_i D_i) f(\underline{\theta},\underline{\lambda})$$

$$= (\theta_i D_i) \text{ in } f(\underline{\theta},\underline{\lambda})$$

Applying the operator D_i on both sides of (4.1) and arranging the terms, we get

$$(4.3)\qquad \theta_i D_i \mu'_{r_1,\ldots,r_i,\ldots,r_n} = \mu'_{r_1,\ldots,r_i+1,\ldots,r_n}$$

$$- \mu_{r_1,\ldots,r_i,\ldots,r_n} \cdot \mu'_{0,\ldots,0,1,0,\ldots,0}$$

A special case of this relation was obtained by Noack (see -6- p.128).

Further rearrangement of the terms in (4.3) gives (4.4) which is $m_1(i) = \mu'_{r_1,\ldots,r_i+1,\ldots,r_n} / \mu'_{r_1,\ldots,r_i,\ldots,r_n}$

$$- \theta_i D_i \text{ ln } \mu'_{r_1,\ldots,r_i,\ldots r_n}$$

This gives

Theorem 2: Given the multimoments $\mu'_{r_1,\ldots,r_i,\ldots,r_n}$ and $\mu'_{r_1,\ldots,r_i+1,\ldots,r_n}$ of the r.vc. $(\Lambda_1,\ldots,\Lambda_n)$, the mean $m_1(i)$ of the marginal r.v. Λ_i $(i=1,\ldots,n)$ is uniquely determined.

In particular, by substituting $r_1=\ldots=r_{i-1}=r_{i+1}=\ldots=r_n=0$ in (4.4) we obtain

$$m_1(i) = m_{r_i+1}(i)/m_{r_i}(i) - \theta_i D_i \ln m_{r_i}(i) \quad i=1,2,\ldots,n$$

which can be restated more clearly as

Theorem 3: Given two successive moments $m_{r_i}(i)$ and $m_{r_i+1}(i)$ of the marginal r.v. Λ_i, the mean $m_1(i)$ is uniquely determined.

Again using relation (4.3) we can easily deduce that the covariance $\sigma(i,j)$ between the marginal r.vs. Λ_i and Λ_j is given by

$$(4.5) \qquad \sigma(i,j) = \theta_i D_i m_1(j) = \theta_j D_j m_1(i)$$

$$= \theta_i \theta_j D_i D_j \ln f(\underline{\theta}, \underline{\lambda})$$

Relation (4.5) show that the covariance of the marginal r.vs. Λ_i and Λ_j is determined uniquely if the mean of any of the marginal r.vs. is given.

5- Characterization of the n - variate GPSD

In this section, we show that given the mean of any marginal r.v. Λ_i, it is possible to find, under very reasonable conditions, the defining function of the n - variate r.vc. $(\Lambda_1,\ldots,\Lambda_n)$.

Theorem 4: The r.vc. $(\lambda_1,\ldots,\lambda_n)$ is uniquely determined from the mean of any one marginal r.v. if the mean contains explicitly all the active parameters.

Proof: Suppose that the mean $m_1(i)$ of the marginal r.v. λ_i is given. Then rearranging (4.2) for $(\underline{\theta}\ ,\ \underline{\lambda}) \in \bar{T}xL$, we have

$$\int_{p_i}^{q_i} [\bar{m}_1(i)/\theta_i]\, d_i = \int_{p_i}^{q_i} D_i [\ln f(\underline{\theta}\ ,\ \underline{\lambda})]\, d_i$$

where $d_i = d\theta_i$ and $[p_i, q_i] \subset [r_i'\ ,\ r_i]$. Therefore

$$(5.1) \qquad M(\theta_1,\ldots,q_i,\ldots,\theta_n,\ \underline{\lambda}) - M(\theta_1,\ldots,p_i,\ldots,\theta_n,\ \underline{\lambda}) =$$

$$\ln [f(\theta_1,\ldots,q_i,\ldots,\theta_n,\ \underline{\lambda})/f(\theta_1,\ldots,r_i,\ldots,\theta_n,\ \underline{\lambda})]$$

where $M(\theta_1,\ldots,\theta_n,\ \underline{\lambda})$ is s.t. $D_i M(\theta_1,\ldots,\theta_n,\underline{\lambda}) = m_1(i)/\theta_i$

$$\forall (\theta_1,\ldots,\theta_n\ ,\ \underline{\lambda}) \in \bar{T}xL.$$

Let $Q(\theta_1,\ldots,p_i,\ldots,\theta_n\ ,\ \underline{\lambda}) = f(\theta_1,\ldots,p_i,\ldots,\theta_n,\ \underline{\lambda})$

$$\exp\left\{ - M\ (\theta_1,\ldots,p_i,\ldots,\theta_n\ ,\ \underline{\lambda}) \right\}$$

and changing q_i into θ_i in (5.1), we get

$$(5.2) \qquad f(\theta_1,\ldots,\theta_i,\ldots,\theta_n\ ,\ \underline{\lambda}) = Q(\theta_1,\ldots,p_i,\ldots,\theta_n\ ,\ \underline{\lambda})$$

$$\exp\left\{ M(\theta_1,\ldots,\theta_i,\ldots,\theta_n,\ \underline{\lambda}) \right\}$$

From the uniqueness of the power series, it follows that (5.2) hold $\forall\ (\theta_1,\ldots,\theta_n\ ,\ \underline{\lambda}) \in \bar{T}xL$. Since $f(\theta_1,\ldots,\theta_n\ ,\ \underline{\lambda})$ has a power series in the active parameter θ_i, it follows that if $K_{x_i}(\theta_1,\ldots,\theta_{i-1},\ \theta_{i+1},\ldots,\theta_n\ ,\ \underline{\lambda})$ is the

coefficient of $\theta_i^{x_i}$ in the expansion of $f(\theta_1,\ldots,\theta_n , \underline{\lambda})$, then $Q(\theta_1,\ldots,p_i,\ldots,\theta_n , \underline{\lambda}) K^*_{x_i}(\theta_1,\ldots,\theta_{i-1},\theta_{i+1},\ldots,\theta_n , \underline{\lambda})$, will be the coefficient of $\theta_i^{x_i}$ in the expansion of $\exp\{M(\theta_1,\ldots,\theta_n,\lambda)\}$ (since $Q(\theta_1,\ldots,p_i,\ldots,\theta_n , \underline{\lambda})$ does not depend on θ_i).

Now, consider the marginal r.v. x_i, we have

$$P_{X_i}(x_i/\underline{\theta}, \underline{\lambda}) = K_{x_i}(\theta_1,\ldots,\theta_{i-1},\theta_{i+1},\ldots,\theta_n, \underline{\lambda}) \theta_i^{x_i}/f(\theta_1,\ldots,\theta_n , \underline{\lambda})$$

$$= Q(\theta_1,\ldots,p_i,\ldots,\theta_n,\underline{\lambda}) K^*_{x_i}(\theta_1,\ldots,\theta_{i-1}, \theta_{i+1},\ldots,\theta_n , \underline{\lambda}) / Q(\theta_1,\ldots,p_i,\ldots,\theta_n,\underline{\lambda}) \exp\left\{ M(\theta_1,\ldots,\theta_i,\ldots,\theta_n , \underline{\lambda}) \right\}$$

$$= K^*_{x_i}(\theta_1,\ldots,\theta_{i-1},\theta_{i+1},\ldots,\theta_n , \underline{\lambda}) \theta_i^{x_i}/\exp\left\{ M(\theta_1,\ldots,\theta_n , \underline{\lambda}) \right\}$$

This shows that $Q(\theta_1,\ldots,p_i,\ldots,\theta_n , \underline{\lambda})$ is arbitrary. Therefore, without loss of any generality, we can assume it to be 1. Hence (5.2) becomes

$$f(\theta_1,\ldots,\theta_i,\ldots,\theta_n , \underline{\lambda}) = \exp\left\{ M(\theta_1,\ldots,\theta_i,\ldots,\theta_n , \underline{\lambda}) \right\}$$

To prove the uniqueness, suppose that $(x_1,\ldots,x_n)$ and $(x_1^*,\ldots,x_n^*)$ are two r.vcs. and that $m_1(i)$ is same for both. Assume that the corresponding defining functions are $f_1(\theta_1,\ldots,\theta_n , \underline{\lambda})$ and $f_2(\theta_1,\ldots,\theta_n , \underline{\lambda})$ respectively. Therefore, from (4.2) for $(\theta_1,\ldots,\theta_n , \underline{\lambda}) \in \bar{T}xL$. we have

$$m_1(i)/\theta_i = D_i [\ln f_1(\theta_1,\ldots,\theta_n , \underline{\lambda})]$$

$$= D_i [\ln f_2(\theta_1,\ldots,\theta_n , \underline{\lambda})]$$

Therefore, in $(\theta_1,\ldots,\theta_n,\underline{\lambda})\in\bar{T}xL$, we have

$$\int_{p_1}^{q_1}\frac{\partial m_1(i)/\theta_1}{\partial q_1}=\int_{p_1}^{q_1}\frac{\partial}{\partial p_1}\frac{\partial \ln f_1(\underline{\theta},\underline{\lambda})}{\partial q_1}=\int_{p_1}^{q_1}\frac{\partial}{\partial p_1}\frac{\partial \ln f_2(\underline{\theta},\underline{\lambda})}{\partial q_1}$$

which implies by changing q_1 into θ_1 that $\forall\ (\underline{\theta},\underline{\lambda})\in\bar{T}xL$

$$f_1(\theta_1,\ldots,\theta_i,\ldots,\theta_n,\underline{\lambda})=G(\theta_1,\ldots,p_1,\ldots,\theta_n,\underline{\lambda})f_2(\underline{\theta},\underline{\lambda})$$

where $G(\theta_1,\ldots,p_1,\ldots,\theta_n,\underline{\lambda})=f_1(\theta_1,\ldots,p_1,\ldots,\theta_n,\underline{\lambda})/f(\theta_1,\ldots,p_1,\ldots,\theta_n,\underline{\lambda})$

Using the same approach as before, we can show that the function G is arbitrary, and therefore, we can take it to be 1. Hence, we have $\forall(\underline{\theta},\underline{\lambda})\in\bar{T}xL\ \ f_1(\theta_1,\ldots,\theta_n,\underline{\lambda})=f_2(\theta_1,\ldots,\theta_n,\underline{\lambda})$

This complete the proof of the theorem.

An important conclusion can be obtained by using Theorems 2 and 4 which is given in

Theorem 5: The r.vc. $(\lambda_1,\ldots,\lambda_n)$ is uniquely determined from its moments $\mu'_{r_1,\ldots,r_i,\ldots,r_n}$ and $\mu'_{r_1,\ldots,\overset{r+1}{i},\ldots,r_n}$.

Also, using Theorems 3 and 4, we obtain

Theorem 6 : The r.vc. $(\lambda_1,\ldots,\lambda_n)$ is uniquely determined from any two successive moments of some marginal r.v.

Now, we ask the question: What functions $m(\underline{\theta},\underline{\lambda})$ can be used as the marginal means of the r.vc. $(\lambda_1,\ldots,\lambda_n)$? The answer is given in

Theorem 7: Let $m(\underline{\theta},\underline{\lambda})$ be a well-defined, non-negative and continuous function of $(\underline{\theta},\underline{\lambda})\in\bar{T}xL$. Then, there exists a r.vc. $(\lambda_1,\ldots,\lambda_n)$

having $m(\underline{\theta}, \underline{\lambda})$ as the mean of one marginal r.v., say λ_i, if and only if

I- There exists a function $M(\underline{\theta}, \underline{\lambda})$ s.t. $D_i M(\underline{\theta}, \underline{\lambda}) = m(\underline{\theta}, \underline{\lambda})/\theta_i$ $\forall (\underline{\theta}, \underline{\lambda}) \in \bar{T} \times L$.

II- Exp $M(\underline{\theta}, \underline{\lambda})$ can be expanded as a power series in the active parameters $\theta_1, \ldots, \theta_n$ with non-negative coefficients $\forall (\underline{\theta}, \underline{\lambda}) \in T \times L$.

Proof follow from Theorem 4.

Theorem 8: The r.vc. $(\lambda_1, \ldots, \lambda_n)$ is uniquely determined from any elements of the variance-covariance matrix of the r.vc. $(\lambda_1, \ldots, \lambda_n)$.

Proof: Suppose that $C(i,j)$ is given. The

case (i): if $i=j$, then $C(i,j)$ is the variance of the r.v. λ_i. Since, it is known that the mean is uniquely determined from the variance in the class of GTSDs (see -3- p.49), the proof follow by using Theorem 4.

case (ii): if $i \neq j$, then $C(i,j)$ is the covariance between the r.vs. λ_i and λ_j Then, using (4.5), we have

$$\int_{p_i}^{q_i} \left[C(i,j)/\theta_i \theta_j \right] d_i = \int_{p_i}^{q_i} D_i D_j \left[\ln f(\underline{\theta}, \underline{\lambda}) \right] d_i$$

i.e.

$$\bar{C}(\theta_1, \ldots, q_i, \ldots, \theta_j, \ldots, \theta_n, \underline{\lambda}) - \bar{C}(\theta_1, \ldots, p_i, \ldots, \theta_j, \ldots, \theta_n, \underline{\lambda}) =$$

$$D_j \left\{ \ln \left[f(\theta_1, \ldots, q_i, \ldots, \theta_j, \ldots, \theta_n, \underline{\lambda}) / f(\theta_1, \ldots, p_i, \ldots, \theta_j, \ldots, \theta_n, \underline{\lambda}) \right] \right\}$$

where $\bar{C}(\underline{\theta}, \underline{\lambda})$ is s.t. $D_i \bar{C}(\underline{\theta}, \underline{\lambda}) = C(i,j)/\theta_i \theta_j$ $\forall (\underline{\theta}, \underline{\lambda}) \in \bar{T} \times L$.

Then, for $(\underline{\theta}, \underline{\lambda})$, let $C(\underline{\theta}, \underline{\lambda})$ be s.t. $D_j C(\underline{\theta}, \underline{\lambda}) = \bar{C}(\underline{\theta}, \underline{\lambda})$. We get

$$(5.3)\quad \int_{p_j}^{q_j} \left[\bar{C}(\theta_1,\ldots,q_i,\ldots,\theta_j,\ldots,\theta_n,\underline{\lambda}) - \bar{C}(\theta_1,\ldots,p_i,\ldots,\theta_j,\ldots,\theta_n,\underline{\lambda}) \right] d_j$$

$$= \int_{p_j}^{q_j} D_j \left\{ \ln \frac{f(\theta_1,\ldots,q_i,\ldots,\theta_j,\ldots,\theta_n,\underline{\lambda})}{f(\theta_1,\ldots,p_i,\ldots,\theta_j,\ldots,\theta_n,\underline{\lambda})} \right\} d_j$$

Changing q_k into θ_k $(k=i,j)$, and writing

$$H(y_1,\ldots,y_{n+1}) = f(y_1,\ldots,y_{n+1}) / \exp\left[C(y_1,\ldots,y_{n+1}) \right]$$

then (5.3) reduces to

$$(5.4)\quad \frac{H(\theta_1,\ldots,\theta_i,\ldots,\theta_j\ldots,\theta_n,\underline{\lambda})}{H(\theta_1,\ldots,p_i,\ldots,\theta_j,\ldots,\theta_n,\underline{\lambda})} = \frac{H(\theta_1,\ldots,\theta_i,\ldots,p_j,\ldots,\theta_n,\underline{\lambda})}{H(\theta_1,\ldots,p_i,\ldots,p_j,\ldots,\theta_n,\underline{\lambda})}$$

Therefore, the ratio does not depend on the j-th argument in H. Also

$$(5.5)\quad \frac{H(\theta_1,\ldots,\theta_i,\ldots,\theta_j,\ldots,\theta_n,\underline{\lambda})}{H(\theta_1,\ldots,\theta_i,\ldots,p_j,\ldots,\theta_n,\underline{\lambda})} = \frac{H(\theta_1,\ldots,p_i,\ldots,\theta_j,\ldots,\theta_n,\underline{\lambda})}{H(\theta_1,\ldots,p_i,\ldots,p_j,\ldots,\theta_n,\underline{\lambda})}$$

As before, the ratio does not depend on the i-th argument in H. Therefore, H does not depend on the i-th and the j-th arguments. Therefore, assume that the ratio in (5.4) and (5.5) equal to $H_k(\theta_1,\ldots,\theta_{i-1},\theta_{i+1},\ldots,\theta_{j-1},\theta_{j+1},\ldots,\theta_n,\underline{\lambda})$ for k=1,2 respectively. Finally, we get $\forall(\underline{\theta}, \underline{\lambda}) \in T \times L$ that

$$f(\underline{\theta}, \underline{\lambda}) = \exp\left[C(\underline{\theta}, \underline{\lambda}) \right]$$

To prove the uniqueness, suppose that $(\lambda_1,\ldots,\lambda_n)$ and $(\lambda_1',\ldots,\lambda_n')$ are two r.vcs. and that the covariance between the i-th and the j-th r.vs. for both is $\sigma(i,j)$. Assume that the corresponding defining functions are $f_1(\underline{\theta}, \underline{\lambda})$ and

$f_2(\underline{\theta}, \underline{\lambda})$ respectively. Therefore, from (4.5) for $(\underline{\theta}, \underline{\lambda}) \in \mathcal{T}_n$, we have

$$\sigma(i,j)/\theta_i\theta_j = D_iD_j\left[\ln f_1(\underline{\theta}, \underline{\lambda})\right] = D_iD_j\left[\ln f_2(\underline{\theta}, \underline{\lambda})\right]$$

Then

$$(5.6) \quad \int_{p_i}^{q_i}\int_{p_j}^{q_j} D_iD_j\left[\ln f_1(\underline{\theta}, \underline{\lambda})\right] d_i d_j = \int_{p_i}^{q_i}\int_{p_j}^{q_j} D_iD_j\left[\ln f_2(\underline{\theta}, \underline{\lambda})\right] d_i d_j$$

Let $H(y_1,\ldots,y_{n+1}) = f_1(y_1,\ldots,y_{n+1})/f_2(y_1,\ldots,y_{n+1})$, then (5.6) reduces after changing q_k into θ_k (for k=i,j) to (5.4), i.e. as before, we get $\forall(\underline{\theta}, \underline{\lambda}) \in T \times L$ that

$$f_1(\underline{\theta}, \underline{\lambda}) = f_2(\underline{\theta}, \underline{\lambda})$$

This complete the proof of the theorem.

6- Examples

In this section, we give several examples to illustrate the theorems proved.

Example 1: Let the mean of the marginal r.v. λ_i be $m(\theta_1,\ldots,\theta_n,k) = k.\theta_i/\theta$

where $\theta = 1-\theta_1-\ldots-\theta_n$, $0 \leqslant \theta_i < 1$, $(i=1,2,\ldots,n)$, $\theta_1+\theta_2+\ldots+\theta_n < 1$ and $0 < k < \infty$.

Let $M(\theta_1,\ldots,\theta_n,k) = -k \ln \theta$. Therefore, the r.vc. $(\lambda_1,\ldots,\lambda_n)$ has a n - variate GPSD in n active parameters and 1 inactive parameter with j.p.f.

$$P_{\underline{A}}(\underline{x}/\underline{\theta},k) = \begin{cases} \dfrac{\Gamma(k + x_1 + \ldots + x_n)}{\Gamma(k)\, x_1! \ldots x_n!}\, \theta_1^{x_1} \ldots \theta_n^{x_n}\, \theta^{k} & (x_1,\ldots,x_n) \in I_+ \times \ldots \times I_+ \\ 0 & \text{otherwise.} \end{cases}$$

This define the n-variate negative multinomial distribution with parameters $k, \theta_1, \ldots, \theta_n$.

Example 2: Let the variance of the r.v. A_1 be $\sigma(1,1)$ $= \theta_1 + \theta.\, \theta_1\, \theta_2$, where $0 \leqslant \theta_1, \theta_2, \theta < \infty$. Therefore, the mean of the r.v. A_1 is

$$m(\theta,\theta_1,\theta_2) = \lim_{p_1 \to 0} \int_{p_1}^{q_1} \left[\sigma(1,1)/\theta_1 \right] dq_1 \Big|_{q_1=\theta_1} = \theta_1 + \theta.\theta_1\theta_2$$

Let $M(\theta,\theta_1,\theta_2) = \theta_1 + \theta.\theta_1\theta_2$. Then it can be shown that the r.vc. (A_1,A_2) has a bivariate GPSD in 2 active and 1 inactive parameter with j.p.f.

$$P_{\underline{A}}(\underline{x}/\underline{\theta}) = \begin{cases} e^{-(\theta_1+\theta\theta_1\theta_2)}\, \theta_1^{x_1} \theta_2^{x_2} \displaystyle\sum_{i=0}^{m} \theta^i / \left[(x_1-i)!(x_2-i)!i! \right] & \\ & (x_1,x_2) \in I_+ \times I_+ \\ 0 & \text{otherwise.} \end{cases}$$

where $m = \min(x_1,x_2)$. This define the bivariate Poisson r.vc. with parameters $\lambda_1, \lambda_2, \lambda_{12}$ where $\lambda_1 = \theta_1$, $\lambda_2 = \theta_2$ and $\lambda_{12} = \theta\theta_1\theta_2$

(see -2- p.810).

Example 3: Let the covariance between the r.vs. A_i and A_j be $\sigma(i,j) = -m\theta_i\theta_j/(1+\theta_1+\ldots+\theta_n)^2$ where $0 \leqslant \theta_i < 1$, i=1,...,n s.t. $0 < \sum_{i=1}^{n} \theta_i < 1$ and m=1,.... Let $\bar{C}(\underline{\theta},m) = m/(1+\theta_1+\ldots+\theta_n)$ and $C(\underline{\theta},m) = m \ln(1+\theta_1+\ldots+\theta_n)$. Therefore, the r.vc. $(A_1,\ldots,A_n)$ has the n - variate GPSD in n active and 1 inactive parameter with j.p.f.

$$P_{\underline{A}}(\underline{x}/\underline{p},m) = \begin{cases} \dfrac{m!}{x!x_1!\ldots x_n!}\, p^x\, p_1^{x_1}\ldots p_n^{x_n} & x_i=1,\ldots,m\ ;\ i=1,\ldots,n \\ & \sum_i x_i = m. \\ 0 & \text{otherwiwe} \end{cases}$$

where $p_i = \theta_i/(1+\theta_1+\ldots+\theta_n)$, $x=m-x_1-\ldots-x_n$ and $p = 1-p_1-\ldots-p_n$. This define the n - variate multinomial distribution with parameters $n, p_1, \ldots, p_n$.

REFERENCES

-1- Abdul-Razak, R.G. (1976), "On bivariate power series distributions". M.Sc. Thesis submitted to the University of Baghdad.

-2- Ahmed, M.S. (1961), "On a locally most powerful boundary randamized similar test for the independence of two Poisson variables" , Ann. Math. Stat., 32, 809 - 827.

-3- Al-Jasim, S.H.A. (1975), "On power series distribution in one parameter", M.Sc. Thesis submitted to the University of Baghdad.

-4- Khatri, C.G. (1959), "On certain properties of power series distributions", Biometrika, 46, 486 - 490.

-5- Kosambi, D.D. (1949), "Characteristic properties of series distributions", Proc. Nat. Inst., Sci. India, 15, 109 - 113.

-6- Noack, A. (1950), "A class of random variables with discrete distributions", Ann. Math. Stat., 21, 127 - 132.

-7- Patil, G. P.(1966), "On multivariate generalized power series distribution and its application to the multinomial and negative multinomial", Sankhya, 28A, 225 - 238.

PHOTOCHEMICAL STUDIES OF SOME PURINES
AND SOLUTIONS OF SOME NUCLEIC ACID BASES

(PART - I)

S.K. Tawfil* and S.Zaa

ABSTRACT

The photoreactions at PH 12 of the aqueous solutions of some nucleic acid bases are compared with those at PH 7. Red shifts in the absorption maxima, due to the formation of the ionized form were observed. The reactions are faster, the calculated rates were greater compared with those obtained from neutral media. For uracil and adenine, this is attributed to the direct attack of OH radicals on the molecules themselfs. For other bases like xanthine and uric acid the reactions were found to be very fast and this is explained on the basis that the bases are converted to their ionic forms which get degraded through ring rupturing reaction on absorbing radiation. The photoreactions in general are found to be faster in oxygen containing solutions, attributed to the action of oxygen as a carrier for the photonic energy.

INTRODUCTION

The photochemistry of pyrimidines is so well documented compared with that of the purines. Several quantitative observations, most of them being based on the destruction of the characteristic band between 200 - 300 nm, are available. Rapport and Canzanelli [1] observed that a twelve hour ultraviolet irradiation of 5×10^{-5} M solutions of adenine, adenosine, xanthine, hypoxanthine, uric acid,

* Chemistry Department, College of Science, Al-Mustansyriah University, Baghdad, IRAQ.

Al-Mustansiriyah Journal of Science, Vol. 2 (1977).

guanine and caffeine, germicidal lamp sufficed in all cases to disrupt completely the absorption spectrum. Stimson[2] observed a similar behavior for isoguanine. Christenson and Giese[3] report that ultraviolet irradiation of adenine, adenosine, and adenylic acid leads to an increase in absorbance over the range 230 - 290 nm.

Loofbourow and Stimson[4] concluded on the basis of absorption spectra, that the lability of the purines and pyrimidines appeared to parallel the number of carbonyl groups in the ring. This statement does seem to apply roughly to the purines where the decreasing order of stability is adenine, hypoxanthine and guanine, xanthine, uric acid.

Ivanchenko et al [5] observed however that both adenosine and guanosine were destroyed faster under oxygen atmosphere. They observed that the quantum yield of photochemical conversion of adenine and its corresponding nucleosides and nucleosides 5-phosphates in liquid (PH 5.6 and 2) and frozen aqueous states do not exceed 10^{-4} and those of guanine and its similar derivatives after removal of oxygen do not exceed 0.3×10^{-4} . In oxygen saturated solutions the yield increases to 0.3×10^{-3} , that is to values commensurate with quantum yield of pyrimidine photolysis.

The production of hydrated electrones by flash photolysis of liquid water has been extensively studied[6] . Boyle et al [7] determined the amount of e^-_{aq} produced by the photoionization of OH^- in neutral water by measuring the amount of e^-_{aq} as a function of PH. The amount of OH^- produced was independent at all PH ranges. However, e^-_{aq} increased 20% at PH = 7.8 as compared to that at PH = 6.7 . At PH values, 8.6, 9.8 and 10.8 it increased by a factor of 2, 6,

and 22 respectively. From PH 10.8 to PH 11.7 no further increase was observed. The following mechanism was proposed at 192 nm,

$$2H_2O \xrightarrow{h\nu} e^-_{aq} + H_3O^+ + OH_{aq} .$$

The aim of this work is to investigate the effect of high PH of the solution on the photolysis of some nucleic acid bases.

EXPERIMENTAL

Materials :-

All chemicals (uracil, adenine, xanthine, uric acid, guanine, uridine, t-butylbromide, and sodium hydroxide) used are of the highest purity and were used without any further purification. t-butanol was prepared by the alkali hydrolysis of t-butylbromide[8], dried and purified before use.

Preparation of Samples :-

Solutions were prepared using triply distilled de-ionized water as solvent. In the case of soluble bases (uracil and adenine) stock solutions (10^{-3} M) were initially prepared by direct weighing. These solutions were diluted in clean, dry volumetric flasks such that optical density is in the range 0.4 to 0.6. In the case of the slightly soluble bases (uric acid and xanthine) saturated solutions were filtered to obtain the stock solution.

De-aeration of solutions : -

Nitrogen gas (99.6 % purity) was bubbled through the solution for the purpose of de-aeration. The gas was passed through sodium hydroxide to remove any carbon dioxide and moisture. The gas was then

bubbled through the solution for half an hour, at a steady rate using a narrow glass tube.

Photoreactor :-

The quantum yield photoreactor was obtained from " Applied Photophysics Ltd. London ". It consists of four separate units (high pressure mercury lamp, quartz lens, filter cell and cuvette holder), which can be mounted on an optical bench. The lamp is 250 watt with an arc size 2 x 4 mm. It emits a number of strong ultra-violet and visible lines, emitting more than 5×10^{18} photon per second, per steradian, of which more than 40% is below 400 nm. The out put of the lamp can be focussed by means of a quartz lens.

Filter cell :-

It is a three compartment quartz cell (30 mm diameter x 20 mm separation per compartment). Cut of wavelengths shorter than 242 nm was done by using 10% aqueous solution of acetic acid.

Photolysis and spectrophotometric measurements :-

The cuvette containing the solution was subjected to irradiation in the photoreactor which after a period of time transferred to the spectrometer to record the change in the spectrum of the solution. A Pye Unicam SP 800 spectrophotometer was used for spectroscopic measurements. The cell compartment of the instrument is fitted with a thermostatically controlled unit enabling temperature stabilization to within $\pm$ 0.1° C, all spectra were recorded at 25 $\pm$ 0.1° C. Potassium dichromate solution and holmium glass filter were used for the instrument calibration.

QUANTUM YIELD EVALUTION

The energy absorbed per unit time, I_{abs} , by a solution of optical density D at some wavelength, when irradiated with parallel light of that wave length will be ;

$$I_{abs} = I_o - I_t$$
$$= I_o - I_o \ (10^{-D})$$
$$= I_o \ (1 - 10^{-D})$$

where I_o is the incident light intensity and I_t is the transmitted light intensity. Assuming constant intensity of illumination and no absorption by the product of irradiation at a wavelength chosen, the quantum yield of degradation of the absorbing substance is ,

$$\Phi = \frac{(A)_o - (A)}{I_{abs} \cdot t}$$

$$\Phi = \frac{(A)_o - (A)}{I_o (1 - 10^{-D})t} \quad \text{moles einstein.}^{-1}$$

I_o, the incident light intensity per unit time on the solution was evaluated by studying the photolysis of uridine under optically identical conditions[9, 10]. The calculated value of I_o remained constant within the limits of experimental error throughout the work. The following results were obtained for the photolysis of aqueous solution of uridine ;

$$I_o = 3.298 \times 10^{-8} \text{ einstein cm}^{-1} \text{ min}^{-1} .$$

rate of the reaction, $R = 6.11 \times 10^{-10}$ moles cm^{-1} min^{-1}.

rate constant of the reaction, $k = 5.71 \times 10^{-3}$ min^{-1} .

RESULTS AND DISCUSSION

The 5,6 double bond ultraviolet absorbing chromophore of uracil absorbs strongly at 259 nm (ϵ = 0.8128 x 10^4). However at PH 12 the spectrum of the ionized form of uracil, shifts to the red, the absorption maximum being 285 nm (ϵ = 0.5012 x 10^4). Similar shifts were observed for other bases, table 1 gives the details.

TABLE 1

Bases	Neutral medium		Basic medium (PH 12)	
	λ max.	ϵ x 10^{-4}	λ max.	ϵ x 10^{-4}
Uracil	259	0.8128	285	0.5012
Adenine	261	1.3489	270	1.1750
Xanthine	269	1.0652	282	0.9587
Uric acid	288	1.0965	295	1.1125
Guanine	-	-	275	0.6978

Irradiation of these bases with unfiltered radiation, since shorter wavelengths are required for the formation of hydroxyl radicals from hydroxyl ions by the following mechanism (11),

$$OH^- \longrightarrow \cdot OH + e^-_{aq}$$

The photoreactions were faster for the bases in basic medium as compared to those in the neutral medium (table 1). In the uracil hydroxyl ion system, all the spectral changes are shown in Fig.1a. The rate of the reaction, as calculated from Fig's 2 is not increased greatly on changing the medium from neutral to basic. However, addition of t-butanol (Fig.4), shows that the photoreaction of the quenched

reaction being slower than that in the neutral medium. Since preliminary studies showed that t-butanol did not quench the photo-reaction of aqueous uracil in the neutral medium, it is evident that in the basic medium the main reacion taking place is the attack of hydroxyl radicals on the uracil molecule (Fig.1b). t-butanol is known to quench hydroxyl radicals that are generated, photochemically or by pulse radiolysis via the following mechanism,

$$(CH_3)_3\,COH + {}^{\bullet}OH \longrightarrow (CH_3)_2\,CH_2COH + H_2O$$

The above reaction is known to be very fast. In the present system the ratio of the base to t-butanol is nearly 1 : 100. Hence the hydroxyl radical generated in the system will be taken up by t-butanol.

The increased rate of reaction in the basic medium for adenine Fig (4) is partially quenched indicating the attack of hydroxyl radicals on the adenine molecules, spectral changes are shown in Fig (3)

Uric acid, xanthine and guanine reacted differently in basic medium as compared to uracil and adenine, as clarified in Fig's (5, 7, 9). The photoreactions of these bases were extremely fast in the basic medium as compared to the photoreactions in the neutral medium Fig's (6,9,10). Uric acid reacted almost completely with a few minutes of photolysis. The reactions were not quenched by t-butanol and the rates of the photoreactions are the same for ordinary and deaerated solutions. The increased photolability is attributed to the conversion of the bases to their ionic forms which get degraded through ring rupturing reactions on absorbing ultraviolet radiation. All rates of reactions and rate constants are given in table 2.

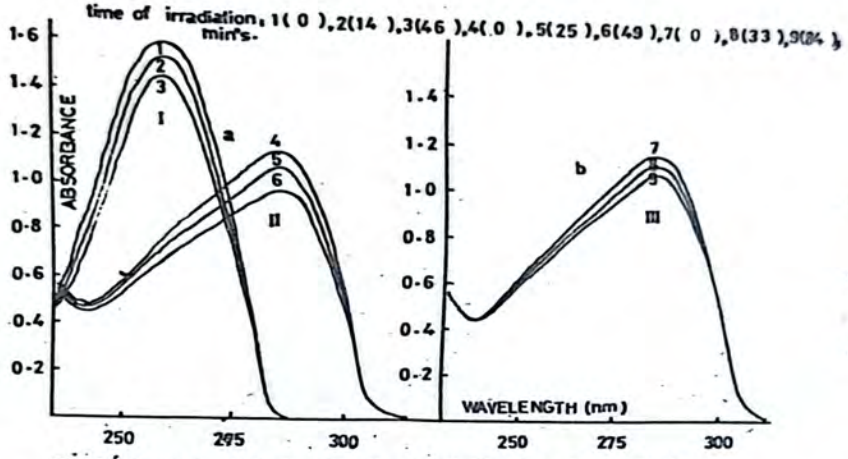

Fig.(1) Spectral changes due to photolysis of aqueous solution, (a) I-uracil, II-uracil+OH^-; (b) uracil + OH^- + t-butanol

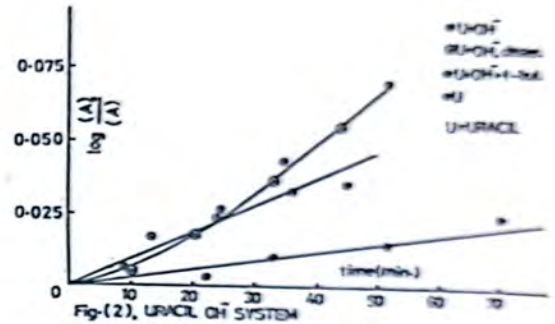

Fig-(2), URACIL OH^- SYSTEM

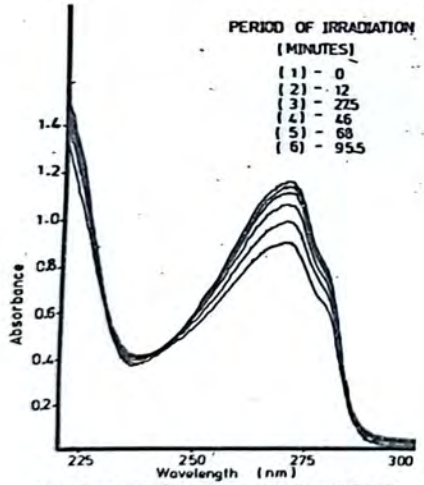

FIG.(3) a Spectral changes due to photolysis of aqueous solution of adenine OH^-

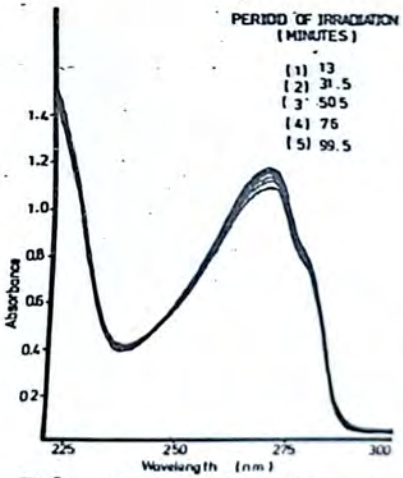

FIG.(3) b Spectral changes due to photolysis of aqueous adenine, OH^-, t-BuOH solution.

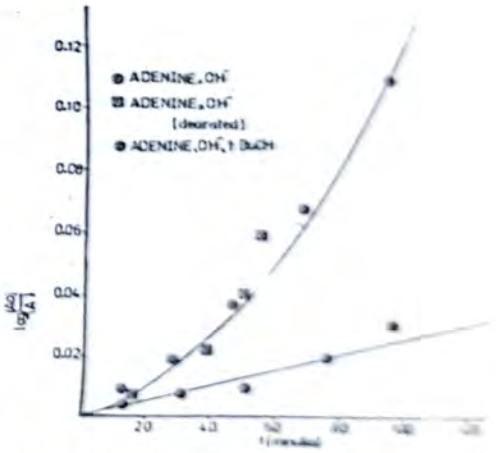

Fig.(4) Plot of $\log \frac{(A_0)}{(A)}$ vs t for adenine OH^- system

Fig 5a) spectral changes on the photolysis of aqueous xanthine, OH^- solution.

Fig 5b) spectral changes on the photolysis of aqueous xanthine, OH^- t. BuOH solution.

FIG(6) Plot of $\log \frac{(A_0 - A_\infty)}{(A - A_\infty)}$ Vs t for uric acid, OH^- system

Fig-(6), XANTHINE, OH^- SYSTEM

TABLE 2 showing rate of reactions (R) and rate constant (k) values for the photolysis of aqueous solutions of some nucleic acid bases at high PH values (irradiation without filter).

Base	$R \times 10^{10}$ moles cm^{-1} min^{-1}			$k \times 10^{3}$ min^{-1}		
	ordinary solution	deaerated solution	solution +t-BUtOH	ordinary solution	deaerated solution	solution +t-BUtOH
Uracil alone	4.17	-	-	2.19	-	-
Uracil + NaOH	4.42!	4.42!	1.38	*	*	0.74
Adenine alone	0.075	-	-	0.11	-	-
Adenine + NaOH	1.40!	1.40!	0.62	*	*	0.59
Xanthine alone	0.42	-	-	1.44	-	-
Xanthine + NaOH	13.33	13.33	13.33	22.36	22.36	22.36
Uric acid alone	18.18	-	-	18.42	-	-
Uric acid + NaOH	39.00!	39.00!	39.00!	*	*	*
Guanine + NaOH	53.85	53.85	53.85	32.91	32.91	32.91

* Only rate constants of first order reactions are reported.

! Rates calculated after 40 minutes of irradiation as determined from plots.

The concentration of NaOH in all cases is 10^{-2} M and that of t-butanol is 10^{-2} M. The concentrations of the different bases are ; Uracil (1.98×10^{-4} M), Adenine (0.994×10^{-4} M), Xanthine (0.75×10^{-4} M), Uric acid (1.18×10^{-4} M), Guanine (1.82×10^{-4} M).

Greenstock et al [12] have shown that in the radiation chemistry of aqueous solutions of purines and pyrimidines, the following reaction does occur ;

$$BH + OH^- \longrightarrow B^- + H_2O$$

(where BH is the base and B^- is the ionized form of the base), similar reactions are expected in the present systems. The ionic forms absorb radiation to give ring open compounds as has been proposed for the base, hydroxyl ion systems. The spectra of the ions are not observed, probably due to their being formed on low concentrations and being unstable to ultra-violet radiation.

The ring rupturing reactions, being oxidation reactions, would be expected to be faster in oxygen containing solutions. This could probably explain the observations that the photoreactions, for most of the reactions were faster in ordinary solutions than in deaerated solutions. Oxygen which normally present up to a concentration of 10^{-4} M in aqueous solution could also act as a carrier of photonic energy to the base, which would assist in the rupturing of the rings.

REFERENCES

1.) D. Rappert and A. Canzanell ; Science, 112 , 469 (1950).

2.) M.M. Stimson ; J. Amer. Chem. Soc. , 64 , 1604 (1942).

3.) E. Christenson and A.C. Giese ; Arch. Biochem. Biophys., 51, 208 (1954).

4.) J.R. Loffbourow and M.M. Stimson ; J. Chem. Soc., 844 (1940).

5.) V.A. Ivanchenko, A.I. Titschenko, E.I. Budowsky, N.A. Sumukowa, and N.S. Wulfson ; Nucl. Acid Res. , 2, (8), 1365 (1975

6.) C.J. Hochnadel ; "Comparitive Effects of Radiation ". (Eds. M. Burton ; J.S. Kirby - Smith, and J.L. Magee) p.151, Wiley, New York (1960).

7.) J.W. Boyle, J.A. Ghormely, C.J. Hochnadel, and J.P. Riley ; J. Phys. Chem., 73, (9), 2886 (1969).

8.) J.S. Swinehart, Organic Chemistry. An Experimental Approach, p.164 (1969), Meredith Corporation, U.S.A.

9.) R.L. Sinsheimer, Radiat. Res., 1,505 (1954).

10.) K.L. Wierzchowski, and D. Shugar ; Acta Biochem. Pol. 6,313 (1959).

11.) K. Schmidt and E.J. Hart ; Advan. Chem. Ser., 81, 267 (1965).

12.) C.L. Greenstock, P.C. Sharage, J.W. Hunt ; J. Phys. Chem., 77, (13), 1624 (1973).

U.V. PHOTOLYSIS OF SOME NUCLEIC ACID BASES IN AQUEOUS SOLUTIONS IN THE PRESENCE OF AMMONIUM NITRATE (PART II)

S.K. Ismail* and S. Das

ABSTRACT

The U.V. photolysis of aqueous solutions of some nucleic acid bases was investigated in the presence of ammonium nitrate. Quantum yields, rate of reactions and rate constants of reactions were calculated. It was noticed that the presence of nitrate ions increases the rate of degradation of uracil. Purines (adenine, xanthine, and uric acid) gave similar increase. t-butanol found to quench the photoreactions of uracil, adenine, and xanthine to a considerable extent and to a lesser extent for uric acid. A mechanism for the different reactions was suggested.

INTRODUCTION

The photochemical alteration of DNA constituent was first reported by Sinsheimer and Hastings[1] who showed that uracil and uridine undergo a reversible photoreaction. Moore[2] was able to show that this reaction was the reversible formation of 5,6, dihydro-6-hydroxy uracil (uridine). Since then the photochemistry of nucleic acids and their constituents have become a very active area of research which has been extensively reviewed [3-11].

The first attempt to study the kinetics was that of Kland and Johnson [12]. Using a 15W GE lamps unfiltered, they irradiated purine solutions under nitrogen and oxygen atmospheres. With the exception of adenine there was an initial induction period followed which the rate increased and then levelled off. They also observed that purines

* Chemistry Department, College of Science, Al-Mustansyriah University, Baghdad, IRAQ.

Al-Mustansiriyah Journal of Science, Vol. 2 (1977).

substituted in 6-position (adenine, hypoxanthine) decomposed faster under oxygen atmosphere, while disubstituted purines (guanine, xanthine) decomposed more quickly under nitrogen atmosphere.

Hydroxyl radicals are generated during the photolysis of aqueous solutions containing nitrate ions. Daniels et al [13] studied the photolysis of nitrate solutions in the first weak absorption band (300 mm). Nitrite was observed to be formed. Use of radical scavengers and consideration of reaction stoichiometries and mechanisms showed that OH radicals were being formed. The following processes were suggested :

$$(A)\quad NO_3^- \xrightarrow{h\nu} NO_3^- + O$$

$$O + NO_3^- \longrightarrow O_2 + NO_2^-$$

$$O + NO_2^- \longrightarrow NO_3^-$$

$$(B)\quad NO_3^- \xrightarrow{h\nu} NO_2 + O^-$$

Shuali et al [14] studied nitrate solutions in the high energy region (195 mm) using flash techniques. They demonstrated the formation of OH radicals by observing the transients formed with CO_3^- , CNS^- , and O_2 , and suggested that four independent processes are taking place ;

$$(1)\quad NO_3^- \xrightarrow{h\nu} NO_3^{-*}$$

$$NO_3^{-*} \longrightarrow (NO_2 + O^-)_{cage} \longrightarrow ONO_2^-$$

$$(2)\quad NO_3^{-*} \longrightarrow NO_2 + O^-$$

$$(3)a-\quad NO_3^- \longrightarrow NO_2^- + O^-$$

$$O + NO_3^- \longrightarrow O_2 + NO_2^-$$

$$O + NO_2^- \longrightarrow NO_3^-$$

$$b- \quad NO_3^{-*} \longrightarrow NO_2 + O$$

$$(4) \quad NO_3^{-*} \longrightarrow NO_2^- + O$$

$$O + NO_3^- \longrightarrow NO_2^- + O_2$$

Barat et al [15] studied the flash photolysis of aqueous solutions of NO_3^- at 200 mm. The results obtained by them support the following primary process,

$$NO_3^- \xrightarrow{h\nu} (NO_3^-)^* \xrightarrow{H_2O} NO + OH + OH^-$$

The flash photolysis did not show any transient absorption in the 500 to 700 nm region thus excluding the following mechanism ;

$$NO_3^{-*} \longrightarrow NO_3 + e^-_{aq}$$

EXPERIMENTAL

The same experimental procedures were followed[16]. For photolysis and spectrophotometric measurements, the photoreactor and the spectrophotometer used in part (I)[16], are used. Ammonium nitrate of AnalaR grade (BDH) was used as an additive. Other chemicals are either puriss or AnalaR as listed in part (I)[16].

RESULTS AND DISCUSSION

Purines are generally more resistant to damage by ultraviolet radiation than pyrimidines. The general results available from literature data indicate the following order of stability towards

ultraviolet radiation; adenine > guanine > xanthine > uracil.

Uric acid, however, is known to be rather labile, its irradiation gives a variety of products. Both purines and pyrimidines belong to a class of resonating molecules, possessing a considerable number of mobile or π electrons associated with the conjugated double bonds and lone - pairs of the heteroatoms. These π electrons form a unique electrical cloud distributed over the molecular periphery, and the existence of this delocalization gives the molecules a complementary stabilization, which is the resonance energy. It may be expected that the existance of this resonance energy will represent a factor of stabilization of the molecules against radiation damage and that the degree of stabilization will be related to the value of the corresponding resonance energy. The resonance energies per π electron are evaluated by Pullman and Pullman [17] for these molecules are in the following order ; adenine > guanine > xanthine > uric acid > uracil.

Purines have a greater resonance energy than the pyrimidines and moreover, adenine, which is the most stable among biologically important bases has the greatest value of resonance energy per π electron.

Irradiation of aqueous uracil solutions caused a decrease in the characteristic absorption centred at 260 mm. The calculated quantum yield is found to be 0.4×10^{-2} moles einstein^{-1} . Deaeration of solution did not effect the reaction. The presence of nitrate ions greatly increased the quantum yield of degradation of uracil ($\Phi = 1.6 \times 10^{-2}$ moles per einstein). Similar increase in the quantum yield of degradation were observed for the purines (adenine, xanthine and uric acid). The calculated quantum yields, rate of

reactions and rate constant of reactions are shown in the table below. The photoreactions of these systems were slower for deaerated solutions. Addition of t-butanol quenched the photoreactions of the system, for uracil, adenine and xanthine, to a considerable extent Fig's. (1,3,5). For the uric acid system, however, the quenching of the photoreaction by t-butanol is much less Fig. (7).

The increase in the quantum yield of degradation of the bases as calculated. Fig's (2a,4a,6a,8a) can therefore be attributed in part, to the reaction of the hydroxyl radicals formed by the photoreaction of nitrate ions, with the base.

The order of photoreactivity obtained for the aqueous solutions of the bases is ; uric acid > uracil > xanthine > adenine.

The order of reactivity of these bases to hydroxyl radicals, as judged by the differences in quantum yields of unquenched and quenched reactions was obtained as ;

uracil > xanthine > adenine > uric acid.

Uric acid though photochemically the most reactive is least reactive to hydroxyl radicals. These results indicate that, of the two possible centres of radical reactivity in the case of the purines, are the C_5-C_6 and the N_7-C_8 bonds, the hydroxyl radicals preferably attack the N_7-C_8 double bond. The C_8 of uric acid is substituted by oxygen, thus rendering it the least reactive to hydroxyl radicals. Based on the above explanations, the following reaction mechanisms have been suggested ;

$$NO_3^- \xrightarrow{h\nu} NO_2 + O^-$$

$$O^- + H_2O \longrightarrow \cdot OH + OH^- \qquad (1)$$

$$URACIL \xrightarrow{h\nu} URACIL^* \qquad (2)$$

Table showing the quantum yields ($\bar{\Phi}$), the rates (R), and the rate constants (k); for the UV photolysis of aqueous solutions of some nucleic acid bases in the presence of nitrate ions under different experimental conditions.

BASES	$\bar{\Phi} \times 10^2$ mole einstein^{-1}			$k \times 10^4$ min^{-1}			$R \times 10^{10}$ mole cm^{-3} min^{-1}		
	Ordinary sol.	deaerated sol.	+t-BUtOH	ordin.sol.	deaer. sol.	+t-BUtOH	ordin. sol.	deaer. sol.	+t-BUtOH
Uracil solution	0.40	0.40	0.53	6.68	6.68	8.75	1.25	1.25	1.70
Uracil + NO_3^- solution	1.60	1.44	0.53	21.30	19.11	8.75	3.90	3.55	1.70
Adenine solution	0.013	0.01	0.016	-	-	0.51	-	-	0.04
Adenine + NO_3^- solution	0.48	0.37	0.08	9.10	7.27	1.43	1.40	1.14	0.24
Xanthine solution	0.05	0.02	0.05	1.64	0.86	1.64	0.14	0.07	0.14
Xanthine + NO_3^- solution	0.69		0.29	**	**	9.21	**	**	0.74
Uric acid solution	0.72	0.72	0.72	23.03	23.03	23.03	2.02	2.02	2.02
Uric acid + NO_3^- solution	2.60	2.36	2.21	80.61	80.61	75.99	6.96	6.52	6.12

* $\bar{\Phi}$ values of solutions after having received 1.3×10^{-6} einsteins cm^{-1} of energy.

** Rate constants and rates of only first order reactions have been reported.

Note: The concentrations of ammonium nitrate and t-BUtOH are 2.18×10^{-3}M and 10^{-2}M respectively.
Uracil concentration = 1.95×10^{-4}M; Adenine concentration = 0.97×10^{-4}M; Xanthine concentration = 0.90×10^{-4}M;
Uric acid concentration = 0.91×10^{-4}M.

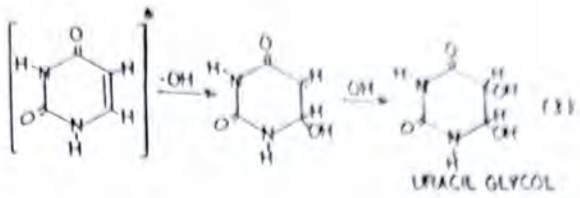

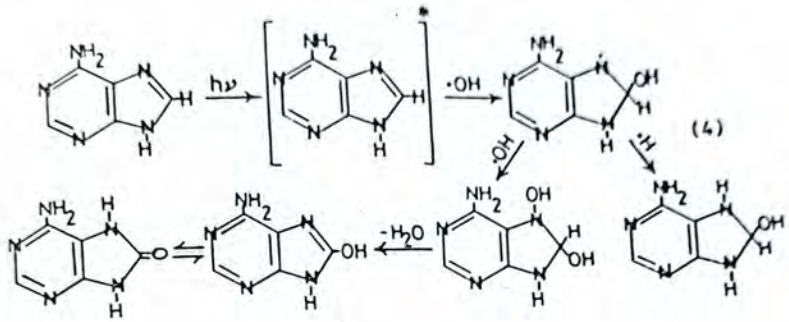

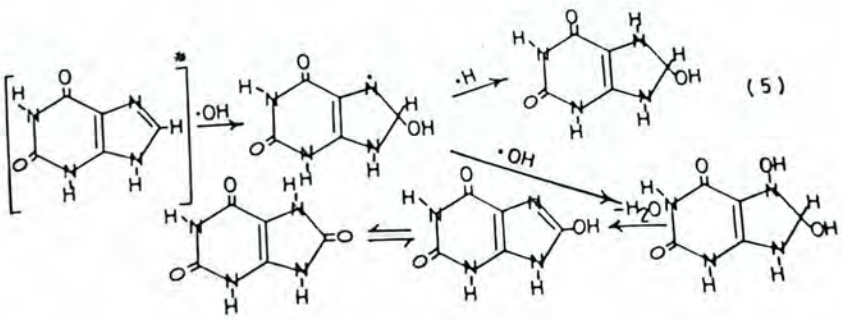

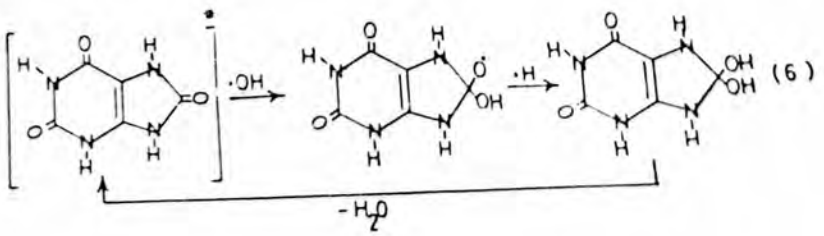

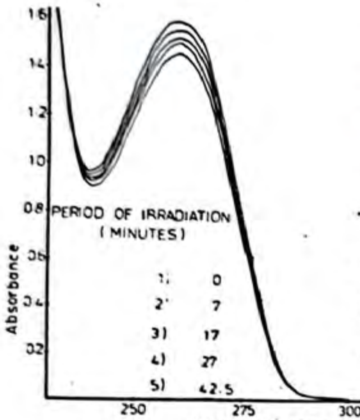

Fig ($\frac{1}{a}$) spectral changes due to the photolysis of aqueous uracil, NO_3^- solution

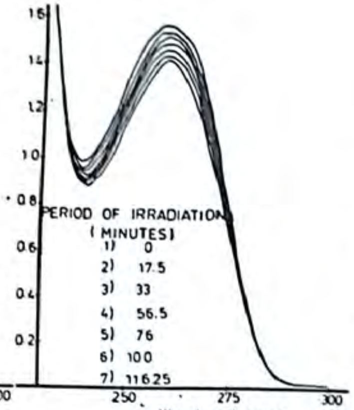

Fig ($\frac{1}{b}$) spectral changes due to the photolysis of aqueous uracil, NO_3^-, t-BUOH solution

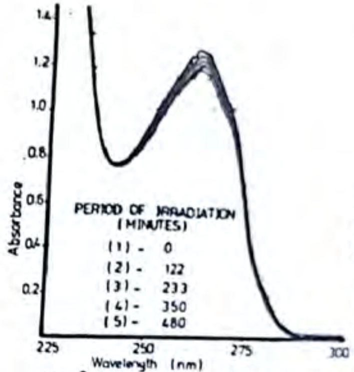

FIG ($\frac{3}{b}$) Spectral changes due to photolysis of aqueous adenine, NO_3^-, t-BuOH solution.

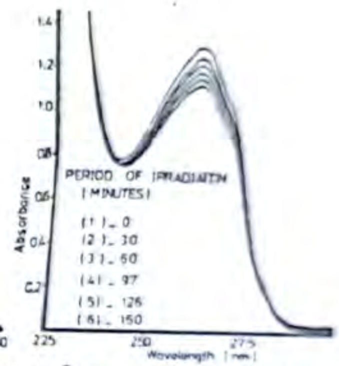

FIG ($\frac{3}{a}$) Spectral changes due to photolysis of aqueous adenine, NO_3^- solution.

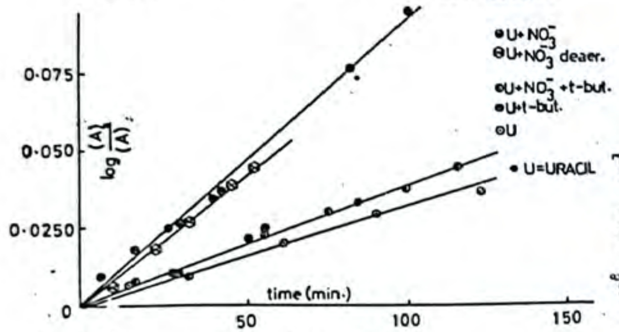

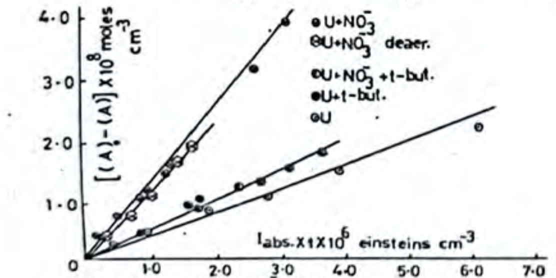

Fig (2) : URACIL + NO_3^- SYSTEM

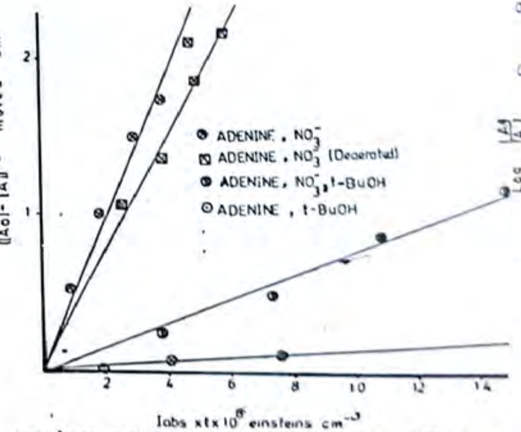

Fig (4a) Plot of ([Ao] - [A]) Vs Iabs x t plot for Adenine, NO_3^- system

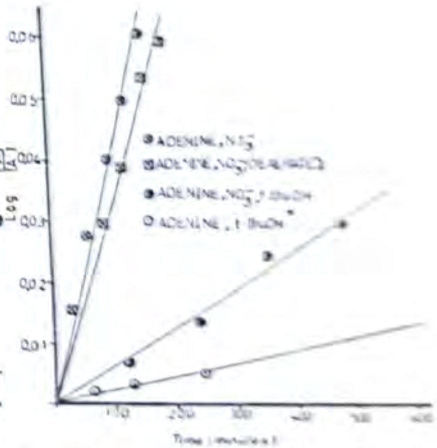

Fig (4b) Plot of log $\frac{[Ao]}{[A]}$ Vs t for adenine - NO_3^- system

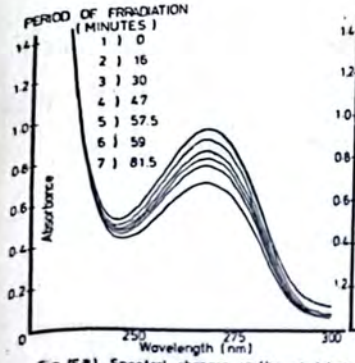

Fig (5a) Spectral changes on the photolysis of aqueous xanthine, NO_3^- solution

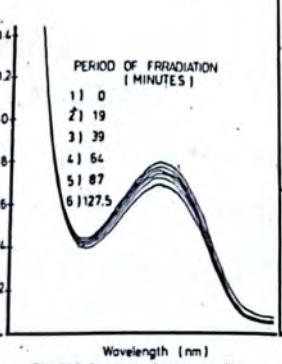

Fig 5b) Spectral changes on the photolysis of aqueous, xanthine, NO_3^-, t. BUOH solution

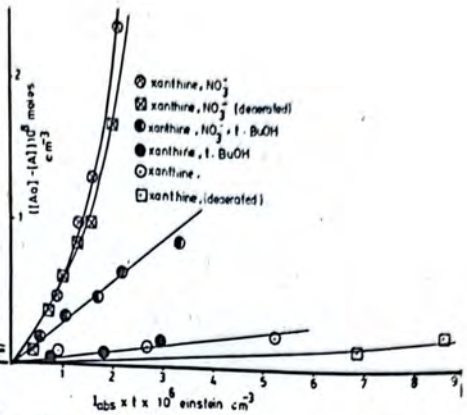

Fig (5a) Plot of $(|A_0| - |A|)$ Vs $I_{abs}t$ for xanthine, NO_3^- system

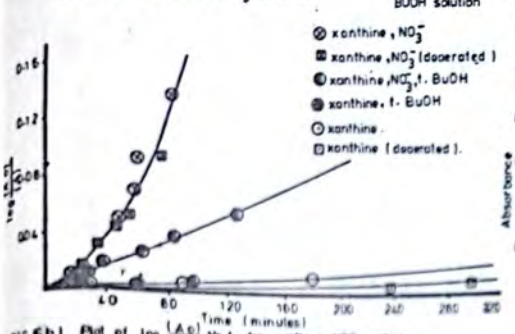

FIG (6b) Plot of $\log \frac{|A_0|}{|A|}$ Vs t for xanthine, NO_3^- system.

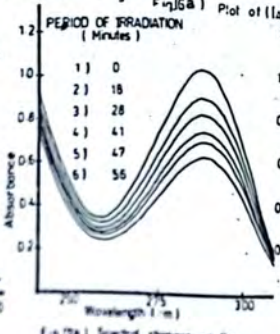

Fig (7a) Spectral changes on the photolysis of uric acid, NO_3^- solution

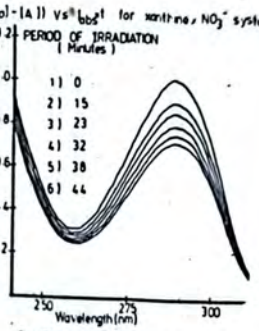

Fig (7b) Spectral changes on the photolysis of aqueous uric acid, NO_3^-, t. Buoh solution.

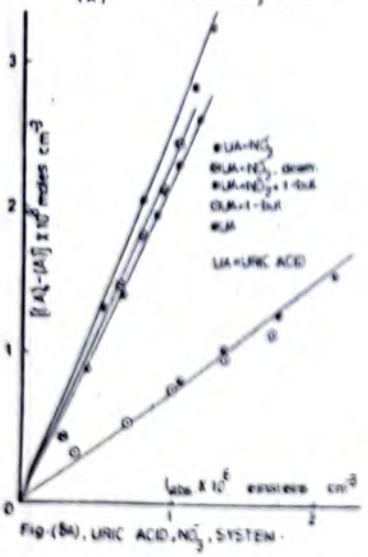

Fig (8a), URIC ACID, NO_3^-, SYSTEM.

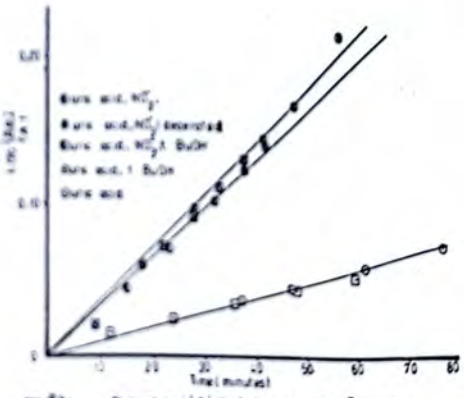

FIG (8b) Plot of $\log \frac{|A_0|}{|A|}$ Vs t for uric acid, NO_3^- system.

In the uric acid - nitrate ion system, t-butanol does quench the photoreaction although to a very limited extent. This indicates that some attack of the hydroxyl radicals does take place at the C_5-C_6 bond of the purines. The reaction mechanism for the purines is proposed below with adenine as an example ;

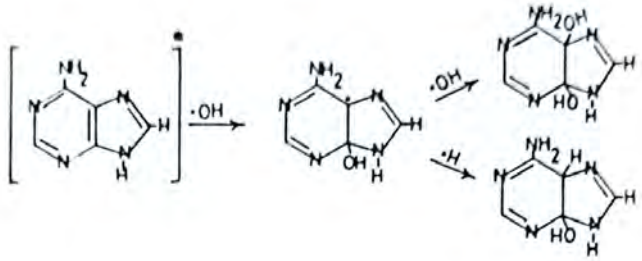

(7)

The presence of nitrate ions greatly increases the quantum yield of degradation of the bases, and the photoreaction is only partially quenched by t-butanol. This suggests the occurence of a reaction other than radical attack. It is proposed that the hydroxyl ions which are formed along with the hydroxyl radicals by the photoreaction of nitrate ions are responsible for this reaction. The possible nature of the reaction is discussed along with base - hydroxyl ion systems. (16)

Plots of log $\frac{(A)_o}{(A)}$ versus time for the above system Fig's (2b, 4b, 6b,8b) indicates first order mechanism in all cases except that of the xanthine-nitrate ion system. This may be due to the formation of uric acid in the xanthine - nitrate system as proposed by reaction (6), which may also react photochemically.

REFERENCES

,) R.L. Sinsheimer and R. Hastings ; Science, 110, 525 (1949).

,) A.M. Moore ; Can. J. Chem., 36, 281 (1958).

,) R. Beukers and W. Berends ; Biochim, Biophys. Acta., 41, 550, (1960).

,) K.C. Smith, "Photophysiology " (A.C. Giese ed.), 2, 329-388, Academic Press, New York (1964).

,) J.G. Burr : Advan. Photochem., 6,-193 - 299 (1968).

,) E. Fahr ; Angew Chem., Int. Ed. Engl. , 8, 578 (1969).

,) A.D. McLaren and D. Shugar ; " Photochemistry of proteins and nucleic acids " , Macmillan, New York (1964).

,) R.B. Setlow ; Progr. Nucl. Acid Res. Mol. Bio. , 8, 257 (1968).

,) P.C. Hanawatt; " Photophysiology " (A.C. Giese ed.) , 4 , 204 - 251, Academic Press, New York (1968).

0.) K.C. Smith and P.C. Hanawatt ; " Molecular Photobiology. Inactivation and Recovery ". Academic Press, New York (1969).

1.) A.J. Varghese ; " Photophysiology " (A.C. Giese ed.), 7, 207, Academic Press, New York (1972).

2.) M.J. Kland and L.A. Johnson, J.Amer. Ghem. Soc., 79, 6187 (1957).

3.) M. Daniels, R.V. Meyers and E.V. Belrado ; J. Phy. Chem., 72, (2), 389 , (1968).

4.) U. Shuali, M. Ottolenghi, J. Rabani and Z. Yelin, J. Phys. Chem., 73, 3445, (1969).

5.) F. Barat, L. Gilles, B. Hickel and S. Sutton ; J. Chem. Soc. (A), 1982 (1970).

6.) S.K. Ismail, and S. Das ; Al-Mustansiriah J. of Science, (1978) Part (I).

7.) B. Pullman and Pullman ; Quantum Biochemistry, P.185 (1963), Inter Science Publishers, New York.

THE EFFECT OF THE PRESENCE OF Fe^{2+} ION ON THE PHOTOLYSIS OF AQUEOUS SOLUTIONS OF SOME PURINES AND PYRIMIDINES (PART - III)

S.K. Ismail* and S.Das

ABSTRACT

The photodegradation of uracil as a pyrimidine is compared with those of some purines in aqueous solutions in the presence of Fe^{2+}. The presence of Fe^{2+} is greatly increased the quantum yield of degradation of both purines and pyrimidines. The system is characterized by an induction period after which the rate is increased rapidly. The rates and the rate constants along with the quantum yields for the reactions were calculated. A mechanism for the different reactions is proposed. t-butanol found to quench the reaction to a large extent for all the bases but not completely due to some reactions taking place other than those with hydroxyl radicals. The photoreactions of this system is found to be slower in deaerated solutions. A formation of complex between ferric ions and uric acid has been suggested for the blue shift obtained after photolysis.

INTRODUCTION

Irradiation of a solution containing DNA[1] to the point where 30% of the pyrimidine bases were destroyed lead to a photoproduct from which entire guanine and almost 90% of the adenine could be recovered. This relative resistance to ultraviolet irradiation of purine as compared to the pyrimidines has been repeatedly observed [2-4]. Due to this relative stability of purines to ultraviolet irradiation as compared to the pyrimidines, so far, it was the photochemical breakdown of the pyrimidines which have received the most attention.

---

* Chemistry Department, College of Science, Al-Mustansyriah University, Baghdad, IRAQ.

Wang [5] reported the photeaddition products of pyrimidines and alcohols. Uracil undergo photochemical reduction in the presence of suitable hydrogen doner. Thus isopropanol the major photoproduct of uracil is 5,6-dihydrouracil[6]. The photeaddition products of pyrimidines with ketones [7-9] amineacids[10-12] have also been reported.

Shugar and Wierzchowski[13] made some rough measurements of quantum yields at 253.7 nm for adenine and guanine.

Several of the photochemical reactions of the purines and pyrimidines involve free radical mechanisms. The action of hydrogen and hydroxyl radicals generated by the action of ionizing radiation on aqueous solutions of the nucleic acid bases have been extensively studied[14]. Butler and Conway[15] investigated the effect of λ 310 nm on nucleic acid bases in the presence of hydrogen peroxide and found the purines (adenine) to be more resistant than pyrimidines (Thymine).

The photochemistry of aqueous ferrous solutions involves an electron transfer. Several factors including the observed photochemical behaviour of these solutions suggested that water hydrating the ion in aqueous solutions is involved in the electronic transition.

$$Fe^{2+}\ (H_2O) + h\nu \longrightarrow Fe^{3+}\ H_2O^-$$

Potteril [16] and Farkas and Farkas [17] have shown that subsequent reactions following the primary electron transfer to the water molecule lead to the liberation of hydrogen from UV irradiation ferrous salt solutions.

$$Fe^{3+}\ H_2O^- \xrightarrow{H^+} \begin{cases} Fe^{3+} + H_2O + H \\ Fe^{3+} + OH^- + H \end{cases}$$

Shiron and Stein[18] have shown that irradiation of low temperature aqueous alkaline glasses containing 10^{-4} M $Fe(CN)_6^{4-}$ produced trapped electrons,

$$Fe(CN)_6^{4-} + h\nu \longrightarrow Fe(CN)_6^{3-} + e^-_{aq}\ .$$

EXPERIMENTAL

Chemicals of either purisa or AnalaR grade were used without any further purification, supplied from either Fluka or BDH as listed in part (I) [19] . ferrous sulfate of AnalaR grade was used. All solutions were prepared in triply distilled water. The same source for photolysis and the same spectrophotometer are used as in part (I) [19] . Deaeration of samples were done by bubbling dry, pure nitrogen gas through solution.

RESULTS AND DISCUSSION

Photolysis of aqueous solutions of ferrous sulfate causes an increase in the absorbance, in the form of a plateau over the region 200 - 375 nm, due to the conversion of ferrous ions to ferric ions. In irradiated aqueous uracil - ferrous sulfate solutions, a decrease in absorbance, in the region of the band maximum and a simultaneous increase in absorbance in the regions 375 - 280 nm and 235 - 200 nm is observed. The absorbance value at the peak accounts for unreacted uracil molecules and newly formed ferric ions. To obtain the absorbance value at the peak, due to unreacted uracil molecules alone, the absorbance value at the wavelength 300 nm (sufficiently far from the peak at 260 nm and assumed to be due to ferric ions alone) is subtracted from the absorbance value at the peak.

The sensitivity of bases to radiation in the present system will be related to their reactivity towards free radicals. One of the structural features responsible for the relative ease of reaction, which consists of addition of a pair of free radicals to one of the double bonds of the purine or pyrimidine molecules, will be the existence of a bond with a high mobile bond order (great double bond character). Pullman and Pullman [20] calculations show that the bond with the greatest mobile bond order is the 5-6 carbon - carbon bond in pyrimidines and the

7-8 nitrogen - carbon bond in purines. The mobile bond order of the C_5-C_6 bond of the pyrimidines is much greater than the mobile bond order of the N_7-C_8 bond in purines. According to the above results, pyrimidines should be more reactive towards radicals than the purines and the radicals should preferably attack the C_5-C_6 bond in pyrimidines and the N_7-C_8 bond in purines.

Addition of t-butanol to the aqueous solution of pure bases caused observable increase in quantum yield only for the uracil solutions. The photoreactions of the other bases were not affected by t-butanol addition. The increase in quantum yield for uracil could be due to the abstraction of hydrogen atom from t-butanol by the 5-6 double bond of uracil.

The presence of ferrous ions in the photolysis process greatly increases the quantum yield of degradation of both the purines and the pyrimidines. The reactions in these systems are characterized by an initial induction period following which the rate of reaction increased rapidly as calculated, see Fig's (2b, 4b, 6a, 8a). For the purpose of comparing the reactivity of the bases in these systems, the quantum yields as calculated from $(A)_o - (A)$ versus $I_{abs} \times t$ plots Fig's. (2a, 4a, 6b, 8b) when the solution received 1.3×10^{-6} einsteins cm^{-3} along with the rates and rate constants for the reactions are shown in the table bellow.

Addition of t-butanol to the solutions of the bases containing ferrous ions quenched the photoreaction to a large extent for all the bases in the above systems as shown in Fig's. (1, 3, 5, 7). The photoreactions of these systems are considerably slower for deaerated solutions.

t-butanol is known to quench hydrogen radicals generated photo- or radiolytically.

$$(CH_3)_3\,COH + \cdot H \longrightarrow (CH_3)_2\,CH_2COH + H_2 \qquad (1)$$

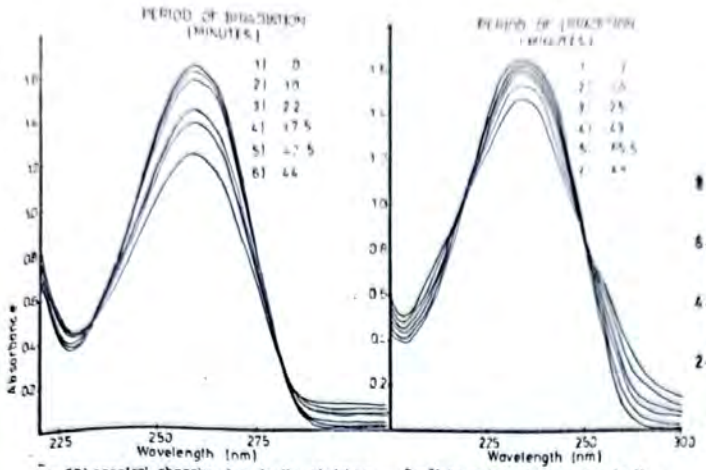

Fig (2a) spectral changes due to the photolysis of aqueous uracil, Fe^{2+} solution deaerated

Fig (2b) spectral changes due to the photolysis of aqueous uracil, Fe^{2+}, t. BUOH solution

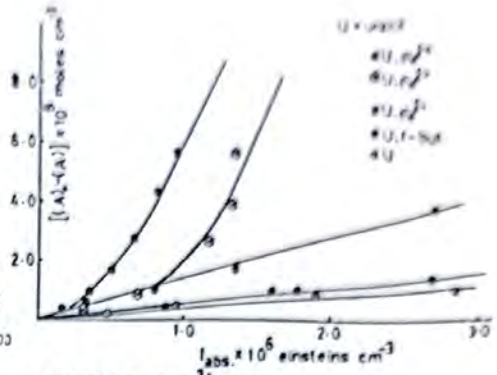

Fig (2), URACIL Fe^{2+} SYSTEM

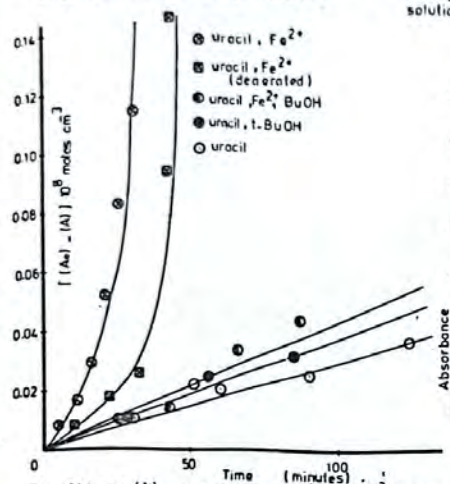

Fig (2b) Log $\frac{[Ao]}{[A]}$ Vs t Plot For the uracil, Fe^{2+} system

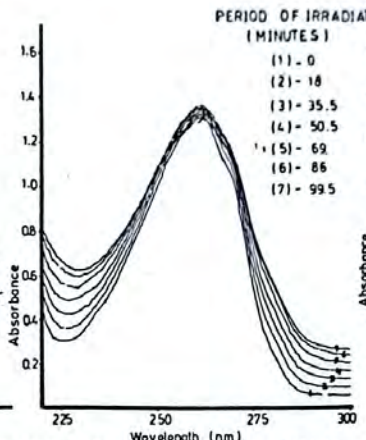

FIG (3a) Spectral changes due to photolysis of aqueous adenine, Fe^{2+} solution.

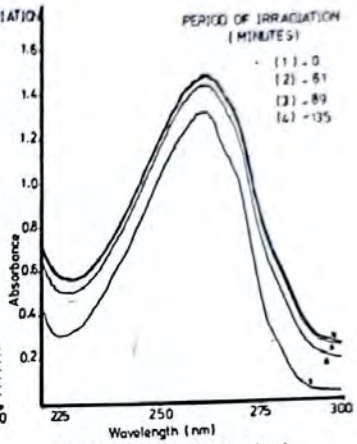

FIG (3b) Spectral changes due to photolysis of aqueous adenine, Fe^{3+}, t. BuOH solution.

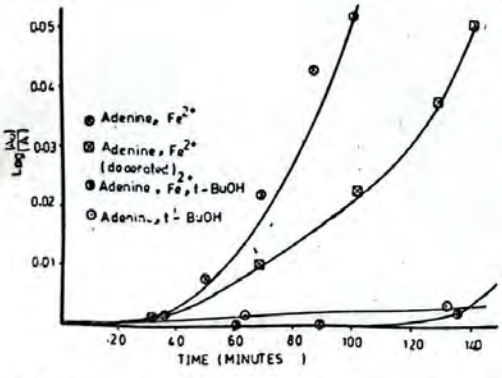

Fig ($\frac{4}{b}$) Plot of Log $\frac{[Ao]}{[A]}$ Vs t for Adenine, $FeSo_4$ system

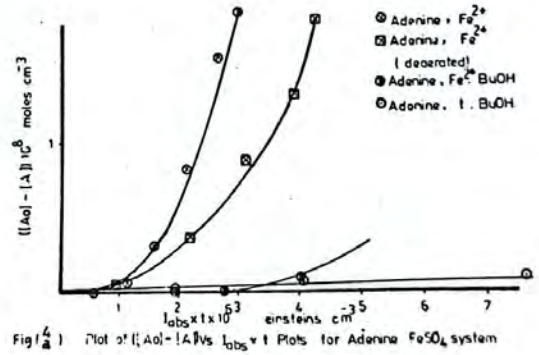

Fig ($\frac{4}{a}$) Plot of $[A_o]-[A]$ Vs $I_{abs} \times t$ Plots for Adenine $FeSO_4$ system

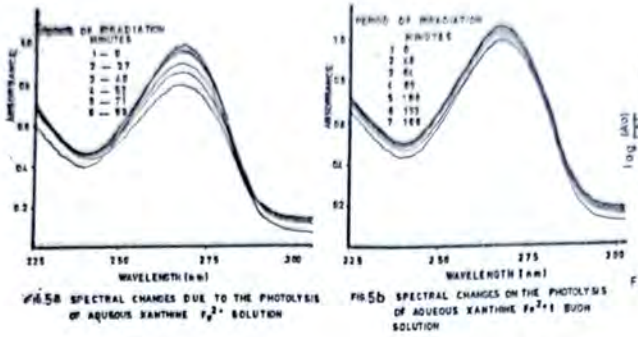

FIG.5a SPECTRAL CHANGES DUE TO THE PHOTOLYSIS OF AQUEOUS XANTHINE Fe^{2+} SOLUTION

FIG.5b SPECTRAL CHANGES ON THE PHOTOLYSIS OF AQUEOUS XANTHINE Fe^{2+} t. BUOH SOLUTION

FIG.($\frac{5}{a}$) Plot of $\log \frac{[Ao]}{[A]}$ vs t for xanthine Fe^{2+} system

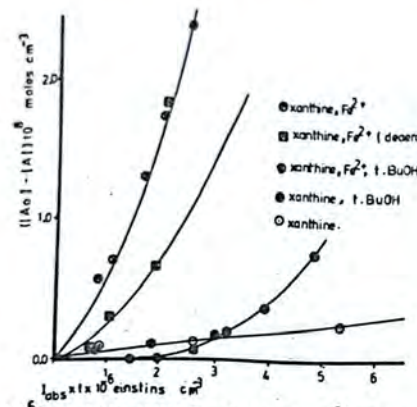

FIG.($\frac{6}{b}$) Plot of $([An]-[A])$ Vs $I_{abs} \times t$ for xanthine, Fe^{2+} system.

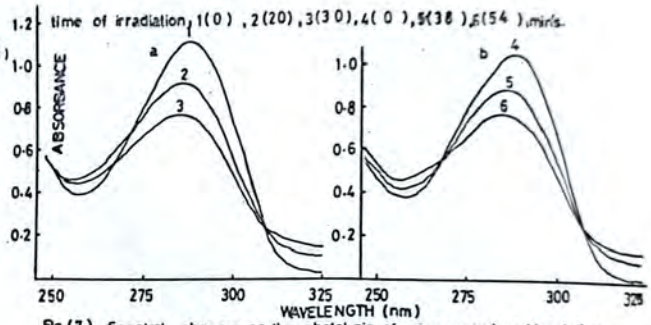

Fig.(7) Spectral changes on the photolysis of aqueous uric acid, solution, (a) + Fe^{2+}, (b) + Fe^{2+} + t-butanol

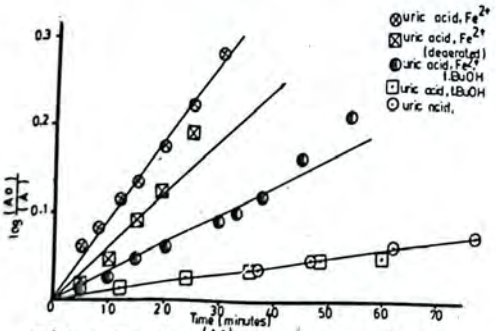

FIG.($\frac{8}{a}$) Plot of $\log \frac{[Ao]}{[A]}$ vs t for uric acid Fe^{2+} system

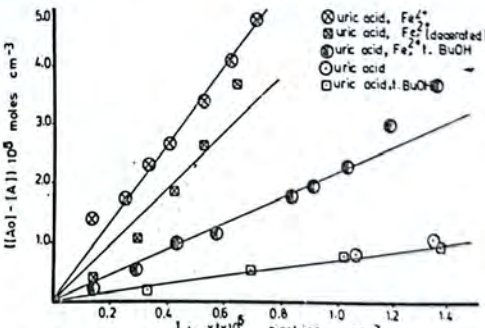

FIG.($\frac{8}{b}$) Plot of $[[Ao]-[A]]$ vs $I_{abs} \times t$ for uric acid, Fe^{2+} system

TABLE showing the quantum yields (Φ), the rates (R), and the rate constants (k); for the effect of Fe^{2+} ions on the photolysis of aqueous solutions of some purines and pyrimidines.

SYSTEMS STUDIES	Φ x10^2 mole einstein^{-1}			k x 10^4 min,$^{-1}$			R x 10^{10} mole cm^{-3} min,$^{-1}$		
	ordinary sol.	deaerated sol.	+t-BUtOH	ordin. sol.	deaer. sol.	+t-BUtOH	ordin. sol.	deaer. sol.	+t-BUtOH
Uracil sclutions	0.40	0.40	0.53	6.68	6.68	8.75	1.25	1.25	1.70
Uracil + Fe^{2+} solution	7.15*	3.23*	1.38*	**	**	**	**	**	**
Adenine solution	0.013	0.010	0.016	-	-	0.51	-	-	0.040
Adenine + Fe^{2+} solution	0.11*	0.08*	0.00*	**	**	**	**	**	**
Xanthine solution	0.050	0.020	0.050	1.64	0.86	1.64	0.14	0.07	0.14
Xanthine + Fe^{2+} solution	0.65*	0.29*	0.00*	**	**	**	**	**	**
Uric acid solution	0.72	0.72	0.72	23.03	23.03	23.03	2.02	2.02	2.02
Uric acid + Fe^{2+} solution	6.67	4.50	214.18	131.18	75.99	22.80	18.60	18.60	8.75

* Φ values of solutions after having received 1.3 x 10^{-6} einsteins cm^{-3} of energy.

** rate constants and rates of only first order reactions have been reported.

Note ; The concentrations of ferrous sulfate and t-butanol are (0.80 - 1.04) x 10^{-4} M and 10^{-2} M respectively.

Uracil concentration = 1.96 x 10^{-4} M ; Adenine concentration = 0.98 x 10^{-4} M ; Xanthine concentration = 0.94 x 10^{-4} M ;

Uric acid concentration = 0.96 x 10^{-4} M.

The above results therefore clearly indicate that all the bases are reactive to hydrogen radicals being generated from the photoreactions of ferrous ions.

$$Fe^{2+}\ (H_2O) \longrightarrow Fe^{3+}\ (H_2O^-) \longrightarrow Fe^{3+} + \cdot H + OH^- \qquad (2)$$

The order of reactivity of the bases towards hydrogen radicals as observed from the differences in quantum yields of unquenched and quenched reactions is ; Uracil > Uric acid > Xanthine > Adenine.

The following reaction mechanisms are proposed for uracil in the presence of ferrous ions ;

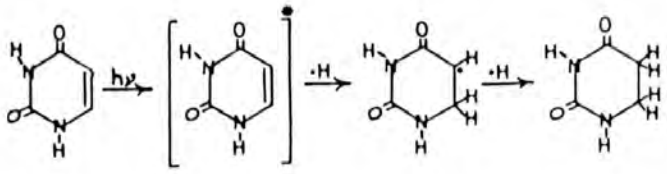

(3)

$$\cdot H + O_2 \longrightarrow HO_2^{\cdot}$$

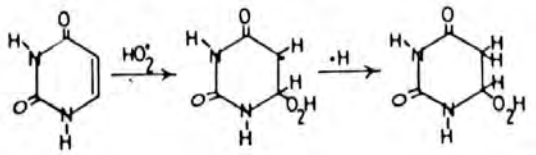

(4)

The observation that uric acid is reactive to hydrogen atoms in spite of the absence of an N_7-C_8 double bond is indicative of the attack of the hydrogen atoms on the 5-6 double bonds in purines. The increased quenching of the photoreaction for this system of uric acid as compared to that in the previous work [21] shows that hydrogen atoms react at the 5-6 double bond to a much greater degree than hydroxyl radicals. This would be expected to be so, since stereochemically it would be more difficult to add hydroxyl radicals at the

5-6 double bond of purines than it would be for hydrogen atoms. The reaction mechanism for the purines in the presence of ferrous ions are suggested below with adenine as an example ;

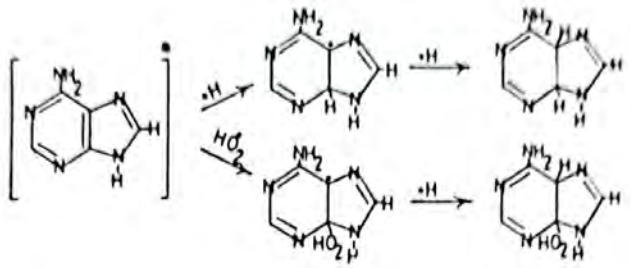

(5a)

(5b)

The reaction of hydrogen atoms at the N_7-C_8 bond would also be expected;

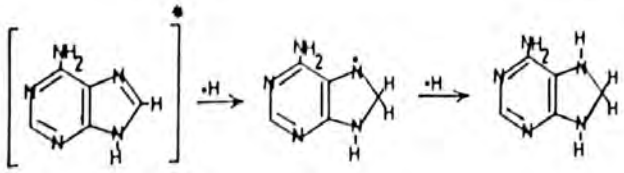

(6)

The increased quenching in the case of uric acid for the present system as compared to the other system [21] could also be due to the attack of hydrogen atoms on the carbonyl group of uric acid. Such a reaction, however, should not cause much changes in the absorption spectra of uric acid. The reaction may possibly proceed via the following mechanism ;

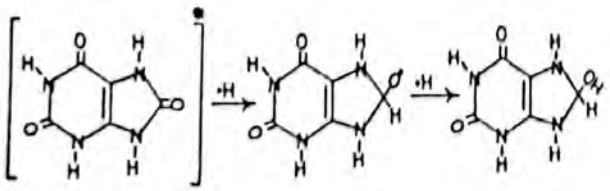

(7)

In the uric acid - ferrous ion system another interesting observation was that on the photolysis the decrease in the absorbance of the band maximum was accompained by a gradual blue shift of the maximum from 288 nm to 285 nm. Similar shifts were observed in the addition of ferric ions to aqueous solutions of uric acid. The shift has therefore been attributed to the formation of a complex between ferric ions and uric acid molecules.

In this system, as, in the base-nitrate ion system [21] the quenching by t-butanol is not complete, that is to say, a reaction other than radical attack is taking place. This other reaction is attributed to the formation of hydroxyl ions along with the hydrogen atoms generated by the photoreactions of ferrous ions.

REFERENCES

1.) M. Errera; Biochim. Biophys. Acta, 8, 115, (1952).

2.) R. L. Sinsheimer and R. Hastings; Science, 110, 525 (1949).

3.) C. E. Carter; J. Amer. Chem. Soc., 72, 1835 (1941).

4.) E. Christensen and A. C. Giese; Arch. Biochem. Biophys., 51, 200 (1954).

5.) S. Y. Wang; Nature (London), 184, 184 (1959).

6.) D. Elad and I. Rosenthal; Chem. Commun., 879 (1968).

7.) I. von Wiluck, H. Mathans and C. H. Kranch; Photochem. Photobiol., 6, 497 (1967).

8.) M. Charlier and C. Helene; C. R. Acad. Sci. Ser D., 272, 743, (1971).

9.) D. R. Arnold; Advan. Photochem., 6, 301 (1968).

10.) K. C. Smith; Photochem. Photobiol., 7, 651, (1968).

11.) K. C. Smith and M. E. O'Leary; Science, 155, 1024 (1967).

12.) K. C. Smith and D. H.C. Meun; Biochemistry, 7, 1033 (1968).

13.) D. Shugar and K. L. Wierzchowski; J. Polymer Sci., 31, 657 (1958).

14.) J. J. Weiss; "Progress in nucleic acids Research and Molecular Biology". (Eds. J. N. Davidson, W. E. Cohnf.), 3 103 (Academic Press, N.Y.), (1964).

15.) J. A.V. Butler and B. E. Conway, Proc. Roy. Soc. (London), B 141, 562 (1953).

16.) R. H. Potteril, O. J. Walker and J. Weiss; Proc. Roy. Soc. (London), A 156, 561 (1936).

17.) A. Farkas and L. Farkas; Trans. Far. Soc., 34, 1113 (1938).

18.) M. Shirom and G. Stein; Nature, 204, 778 (1964).

19.) S. K. Ismail and S. Das; Al-Mustansyriah J. of Science, (1978); PART (I).

20.) B. Pullman and A. Pullman; Quantum Biochemistry p. 185 (1963) Inter Science Publishers, N.Y.

21.) S. K. Ismail and S. Das; Al-Mustansyriah J. of Science, (1978), PART (II).

مجلة علوم المستنصرية

كانون الأول ١٩٧٧

رقم الايداع في المكتبة الوطنية ببغداد (٢٧٨) لسنة ١٩٧٧

مجلة
علوم المستنصرية
المجلد ٢ كانون الأول ١٩٧٧
كلية العلوم — الجامعة المستنصرية — بغداد — العراق —

تعليمات للمؤلفين

١. تقدم ثلاث نسخ من البحث مطبوعة على الآلة الكاتبة وعلى ورق ابيض صقيل وتترك مسافة ٢,٥ سم على يسار كل صفحة .
٢. تقدم خلاصة باللغة العربية وأخرى باللغة الانكليزية وتطبع كل منهما على ورقة منفصلة .
٣. يطبع عنوان البحث وكذلك اسم المؤلف (او المؤلفين) وعنوانه على ورقة منفصلة ويكتب اسم المؤلف كاملا كان يكتب (احمد م. علي) .
٤. تقدم الرسوم التوضيحية منفصلة عن مسودة البحث وترسم بالحبر الصيني الاسود على ورق شفاف وترفق ثلاث صور لكل رسم وتكتب عناوين الرسوم على نفس الورقة .
٥. تنظم الجداول باسلوب تجعلها مفهومة دون اللجوء الى النص وذلك باعطاء كل جدول وكل عمود وصفا واضحا .
٦. لايجوز اعطاء المعلومات ذاتها بالرسم وبالجدول في وقت واحد الا اذا اقتضت ضرورة النقاش ذلك .
٧. يشار الى المصدر برقم ضمن قوسين [ ] بعد الجملة مباشرة وتطبع كافة المصادر على ورقة منفصلة ويتوجب عند ذكر مختصرات اسماء المجلات اتباع اسلوب
٨. من المحبذ حيثما كان ممكنا ان يتسلسل البحث ليتضمن المقدمة ، طرق التجربة ، النتائج ، المناقشة.

مجلة علوم المستنصرية

طالب

المجلد ٢ كانون الاول ١٩٧٧

مطبعة كلية العلوم
جامعة بغداد